Chemometrics in multispectral imaging for quality inspection of postharvest products

Chemometrics in multispectral imaging for quality inspection of postharvest products

een wetenschappelijke proeve op het gebied van de
Natuurwetenschappen, Wiskunde en Informatica

Proefschrift

ter verkrijging van de graad van doctor
aan de Radboud Universiteit Nijmegen
op gezag van de Rector Magnificus prof. dr. C.W.P.M. Blom,
volgens besluit van het College van Decanen
in het openbaar te verdedigen op vrijdag 25 februari 2005
des namiddags om 1.30 uur precies
door

Jan Corstiaan Noordam
geboren op 23 april 1970
te Bleiswijk

Febodruk BV Enschede

Promotor: Prof. dr. L.M.C. Buydens

Copromotor: Dr. W.H.A.M. van den Broek
Agrotechnology and Food Innovations BV

Manuscriptcommissie: Prof. dr. ir. P. van Espen
Universitaire Instellingen Antwerpen, België

Dr. P. Geladi
Near Infrared Center of Excellence, Umeȧ, Sweden

Prof. dr. R.N. Rutledge
Institut National Agronomique, France

The research reported in this thesis was partially supported by:

- the Ministry of Economic Affairs under the IOP (Innovation Oriented Research) programme,
- the Ministry of Agriculture, Nature Management and Fisheries
- Agrotechnology and Food Innovations

ISBN 90-9018754-5
Copyright © 2005 by J.C. Noordam

Dankwoord

Tijdens mijn sollicitatiegesprek in december 1996 bij Agrotechnology and Food Innovations (het toenmalige ATO) werd mij gevraagd of ik interesse had om eventueel te gaan promoveren. Ik heb dat destijds positief beantwoord. Als ik toen geweten had wat er bij komt kijken om een promotieonderzoek succesvol uit te voeren naast een fulltime baan zou ik daar misschien iets langer over nagedacht hebben. Er zijn dan ook wel een aantal mensen die hebben bijgedragen aan de realisatie van dit proefschrift en die wil ik dan ook graag van harte bedanken.

Allereerst wil ik mijn promotor Lutgarde Buydens bedanken voor de mogelijkheid en het vertrouwen dat zij mij heeft gegeven om dit promotieonderzoek uit te voeren. Zij was van begin af aan enthousiast over het onderwerp en heeft ervoor gezorgd dat de rode draad duidelijk bleef.

Maar uiteindelijk ben ik toch de meeste dank verschuldigd aan mijn copromotor Willie van den Broek, hij is toch degene geweest die mij destijds uiteindelijk over de streep heeft getrokken om de al ruim een jaar lang sluimerende ideeën en ambities daadwerkelijk te gaan vormgeven tot een heus promotietraject. Willie, je was altijd beschikbaar om over het lopende onderzoek of de geschreven artikelen te discussiëren waarbij je vaak de pijnpunten kon aanwijzen. Je functioneerde tevens als eerste reviewer van de artikelen, wat denk ik ook voor Lutgarde niet onplezierig was, en waar toch heel wat uurtjes in zijn gaan zitten. Willie, bedankt voor alle hulp en morele steun.

Toine Timmermans wil ik bedanken voor zijn hulp en inspanningen tijdens het opstarten van het traject. De toekenning van het gezamenlijk geschreven voorstel voor een 2-jarig IOP project zorgde ervoor dat er ook bij daglicht aan het onderzoek gewerkt kon worden. Toine, bedankt voor je inzet en vertrouwen, het is dan toch maar mooi gelukt!

Mijn collega’s binnen het thema Product Quality Measurement bedank ik voor hun hulp bij diverse facetten gedurende het onderzoek, variërend van het meedenken over de uitvoering van lastige programmeerklusjes tot het geven van nuttige adviezen bij de brainstorms of discussies tijdens de koffiepauzes. Een speciaal woord van dank wil ik richten aan verschillende mensen binnen Agrotechnology and Food Innovations die er voor gezorgd hebben dat het promotietraject ook organisatorisch en financieel klopte: Arjen Simons, Hans Maas en Jan Top.

De multispectrale opnamen hadden niet gemaakt kunnen worden zonder de apparatuur van Plant Research International waar collega-promovendus Gerrit Polder werkte aan multispectrale beeldverwerking binnen zijn IOP clusterproject. Samen met Gerie en Paul vormden jullie gedrieën niet alleen een goed discussiepanel maar zijn jullie ook zeer behulpzaam en flexibel geweest in het beschikbaar stellen van de multispectrale meetopstelling, dank hiervoor.

Hoewel het onderzoek zich grotendeels in Wageningen afspeelde, waren er naast de voortgangsbesprekingen met Lutgarde ook nog de research besprekingen van de aio’s op de vakgroep analytische chemie in Nijmegen waar ik regelmatig heen ging om weer wat op steken, bij te blijven en te babbelen. Ik heb deze contacten met aio’s, staf en studenten altijd erg leuk gevonden en op prijs gesteld. Dank Arjan, Uwe, Jos, Philip, Lammert, Egon, Thanh, Rufen, Fabien, Geert, Willem, Brigitte. Jullie hebben mij altijd het gevoel gegeven een interne promovendus te zijn in plaats van een ’externe’. In het bijzonder wil ik Ron Wehrens bedanken voor zijn bijdrage tijdens discussies in gezamenlijk overleg en via email over ’onze’ clustering problemen.

Een zeer speciaal woord van dank gaat uit naar mijn lieve lief, Lydia, niet alleen voor haar steun en gezelschap gedurende de lange reizen naar de conferenties, maar ook voor haar geduld en begrip voor wanneer er weer een artikel af moest. En verder bedank ik Albert en Annemarie, mijn ouders, familie en vrienden. Velen hebben mij vaak voor gek verklaard (”waar je zin in hebt!”, was een vaak gehoorde spontane reactie. . .) maar zijn mij toch ook altijd blijven steunen en motiveren.

Arnhem, *Jacco Noordam*
December 2004

Contents

Chapter 1

Introduction to multivariate imaging in agriculture

1.1 What is quality?

This is a striking title of a manuscript [1] which discusses several aspects of the term quality in relation to consumers. Here quality is defined from either a product orientation or a consumer orientation. A more detailed and broader description of the relation between quality and consumer is described in literature [2], where a consumer is considered as a part of a product chain and each next item in that product chain can be considered as a consumer by the previous one: grower, packer, distributor, retailer, produce manager, shelf stocker, shopper, and finally the ultimate consumer who actually consumes the product. As a result of that, the quality criteria vary as [2] ”Each consumer in the chain has its own set of quality or acceptability criteria, often biased by personal expectations and preferences”.

1.1.1 Measuring quality

Consumers use a combination of sensory inputs like appearance, aroma and hand-feel of the entire product to obtain a final judgment of the acceptability of that fruit or vegetable. A lot of instruments have been developed in the past [2] to imitate human testing methods. Where aroma and hand-feel are more recent research topics, appearance in relation with fruit and vegetable quality has been a research topic for many decades. Appearance is not only related to the expected or required color of the fruit or vegetable but also to the presence of abnormalities, deformations or even visible defects on the fruit or vegetable. There have been many reviews of technologies in literature [2, 3, 4] concerning the appearance quality attribute. A specific number of technologies focus on replacing or imitating the visually human testing methods and are therefore based on imaging technologies as the spatial distribution of abnormalities on the products under consideration require the use of imaging systems. Figure 1.1 shows some typical appearance based quality defects on food products.

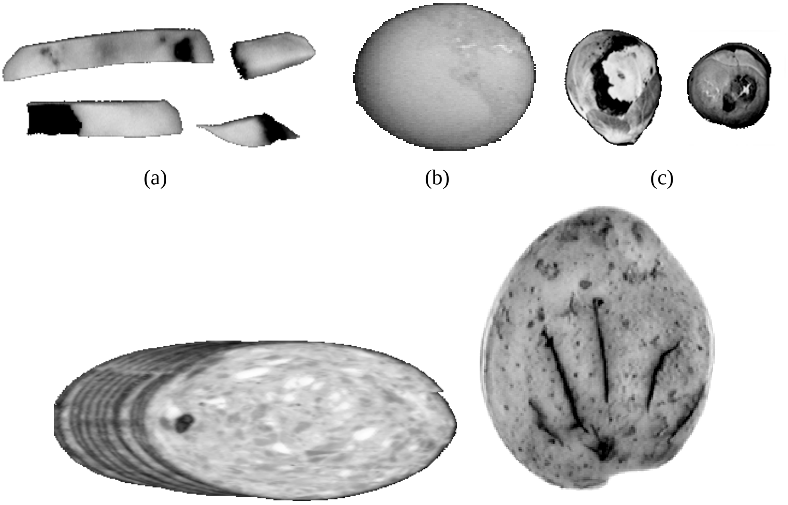
(a) (b) (c)

(d) (e)

Figure 1.1: *Typical appearance based quality defects on postharvest products. (a) defects on raw French fries; (b) faeces on eggs; (c) rot and alternaria on Brussels sprouts; (d) blood spots in cold meats; (e) cracks in consumer potatoes.*

Although appearance goes hand in hand with imaging due to the requirement of spatial information, this does not imply it is limited to the visible wavelength range. The for humans visible wavelength range is only a small part of the electromagnetic spectrum, the whole spectrum ranges from microwave, infrared, visible light, ultraviolet, X-ray to gamma-ray radiation. Although techniques like X-ray and nuclear Magnetic Resonant Imaging (MRI) have potential for detecting diseases and defects in agricultural products [5, 6, 7, 8, 9], their applications are still limited due to the high cost of equipment and low operational speed. MRI has been applied for the detection of mealiness in apples [10], bruises in apples [11], differentiation between fresh-killed and frozen trout [12], the effect of freezing on pork quality [13], detection of hollowness in rice [14] and internal quality evaluation of tomatoes, olives, apples, peaches, pears, unions, oranges, cucumbers and pineapples [15]. Reviews about MRI and X-ray technologies and their applications in food is given in literature [2, 6, 16].

1.1.2 Interaction of matter with light

When a fruit or vegetable is exposed to light, about 4% of the incident light is reflected at the outer surface, causing specular reflectance or gloss, and the remaining 96% of incident energy is transmitted into the product [17]. Most light energy penetrates only a very short distance and exits near the point of entry, which is the basis for color. As color is directly related to consumer perception of appearance, it explains why color imaging is preferred over gray value imaging. Therefore, color imaging has been the basis for sorting and grading al kind of products in different grades. Inspection of food products with color imaging have been reported for various applications like the detection of external defects on whole potato tubers [18, 19, 20, 21, 22, 23], the detection of defects on apples [24, 25] and inspection of beef tenderness [26]. Extended reviews about color inspection are reported in literature [27, 28, 29, 2, 30].

The wavelength dependent interaction of light with material of the product has been studied for many years and has resulted in various measurement techniques in both the near infrared and infrared region of the electromagnetic spectrum. The underlying principles of techniques like Raman spectroscopy, Mid and Near infrared (MIR and NIR) spectroscopy are thoroughly described in literature [31]. The relative long measurement times and the low intensities of Raman has limited its application in agriculture. This is in contrast with NIR spectroscopy, there is a huge amount of literature concerning NIR spectroscopy and its relationship with respect to food quality [32]. Although recent NIR systems are able to perform realtime inline measurements, no indication of disease or defect area can be obtained as only single spectral point measurements are acquired. The lack of spatial resolution makes NIR less suitable for appearance based quality inspection, as opposed to the more recently described spectral cameras. These cameras permit acquisition of images at multiple wavelengths, which is called spectral imaging, thereby providing both spectral and spatial information which makes them more suitable for appearance based quality control.

1.1.3 Spectral image acquisition

Spectral imaging, where imaging techniques are combined with spectral information, can be executed by placing different optical bandpass filters in front of a monochrome camera. This allows the acquisition of multiple images at multiple wavelengths after changing a filter. Sometimes the filters are placed in a filter wheel which can rotate in front of the camera [31, 33]. Applications on food products with this approach are described for the detection of wholesome birds in a poultry slaughter plant [34, 35, 36, 37], the detection of bruises on peaches and apricots [38], the status monitoring in vegetables such as cabbage [39], detection of parasites in cod fillets [40, 41] and for the the spatial distribution of soluble solids in melons [42]. A more elegant and convenient approach for acquiring a multispectral image is to place a Liquid Crystal Tunable Filter (LCTF) in front of the camera. A tunable filter is a filter whose spectral transmission can be electronically controlled by applying voltage. There are no moving parts and no discontinuity in the spectral transmission range, thus providing finer spectral sampling, and rapid and random switching between wavelength bands. Tunable filters are available in both the visible and NIR region of the electromagnetic spectrum. A detailed description about the principles and various applications can be found in literature [43, 44, 45, 46, 47]. Applications in agriculture are the classification of blemishes on apples [48], the mapping of light penetration in apples and tomatoes [49], the discrimination between different food products [50] and the detection of herbicide stress in crops [51].

A drawback of filters in front of the camera is that it takes multiple recordings to acquire a complete multivariate image. In the time required to take a full multispectral image, the object under inspection is not allowed to move. True multispectral imaging systems do not have this problem and can acquire all wavelengths simultaneously. A example of such systems are the so-called common aperture multichannel camera's which can take a full view full spectrum multivariate image in a single shot. A traditional 3-CCD Red Green Blue (RGB) color camera is a well known multichannel common aperture camera. The three color channels are usually fixed and selected beforehand by selecting the appropriate coatings and filters. With this principle 3-6 channel common aperture constructions are possible, more channels becomes difficult due to the lack of space for the optics. A custom made 3 channel camera system is applied for the quality inspection of citrus fruits [52] and defect detection in bell pepers [53].

Another variant of the common aperture technique is called wavelength dispersive multispectral imaging. This technique acquires all wavelength data simultaneously and generates the image sequentially. A line of spatial information with a full spectral range per spatial pixel is captured sequently to obtain a continuous multispectral image. With this approach it is guaranteed that multiple wavelength integrity is maintained even when an object is moving or the chemical dynamics are changing. Imaging spectrographs (e.g. Imspector, Spectral imaging Ltd. Oulo, Finland) coupled with a C-mount lens and attached to a camera use this principle to acquire multispectral images. The spectrograph consists of a Prism-Grating Prism (PGP) principle which redirects the light onto the CCD. To obtain a multispectral image, either the object or the Imspector must translate. The Imspector principle is well described in literature [54]. Applications of such multispectral imaging systems has been reported for the quality inspection of poultry [55, 56, 57, 58, 59] and chickens [60, 61, 62], meat [63, 64], the measurement of ripeness of tomatoes [65], the inspection of cherries [66] and apples [67, 68, 69, 70], the spatial distribution of soluble solids in kiwi fruit [71], for the quality evaluation in nuts and grains [72], detection of scab in wheat [73] and detection of aflatoxin in corn [74].

1.1.4 Unsupervised and supervised classification of multispectral images

In the majority of aforementioned multispectral imaging applications for appearance based quality control, the goal was to detect small defects or abnormalities in the object under inspection. To quantify the amount of defects or abnormalities in the inspected object classification of the spectra is required. In cases where only a single multivariate image or a few multivariate images with no a priori spectral information is available, no training set can be extracted from these images to train a supervised classifier. In those cases, unsupervised classification techniques can be applied as a segmentation technique for those images.

Unsupervised classification

A widely used unsupervised technique is Fuzzy C-Means [75] (FCM). The main reason for its popularity as an image segmentation technique is its transparency and unsupervised nature [76, 77, 78]. Furthermore, its ability to detect clusters of different shape such as spherical, elliptical, shells and lines makes it a versatile technique [79, 80] for the segmentation of multivariate images. Another reason for the popularity of FCM is its good performance in high dimensional spaces when the number of objects are limited [81]. This is an important feature as in pattern recognition literature, it is widely known that a finite number of training samples can lead to practical difficulties in designing a classifier for high dimensional spaces [30, 82, 81, 83]. Known drawbacks of FCM such as the required parameter for the number of clusters, its sensitivity for initialization and its sensitivity of clusters with different number of objects have not led to any obstruction given the number of widespread applications in multivariate imaging [84, 85, 86, 87, 88, 89, 90, 91, 92, 93, 94, 95, 96].

Multispectral images of postharvest products

However, when FCM is applied as a clustering technique to segment multivariate images for appearance based quality evaluation of food products, care should be taken when there is great difference in object area between objects of different classes. This is not uncommon for multivariate images acquired in postharvest quality inspection where small sized defects can occur on products that contain defects or diseases. The difference in object size between different classes effects the partitioning of the data space and thus the final image segmentation will be influenced by this cluster size sensitivity. A direct result of these incorrect segmentation is an over or under estimation of the classes on the inspected product. In literature, two FCM based techniques have been reported that overcome this cluster size sensitivity [97, 98] although both techniques are somewhat impracticable for segmenting single or few images in high dimensional spaces. The Fuzzy Maximum Likelihood Estimation [97] (FMLE) requires the estimation of a covariance matrix for each class, something which requires a lot of parameter estimation and thus a lot of measurements. The semi supervised FCM (ssFCM) algorithm [98] requires a priori information about clusters and labels, something which is not always available. Therefore, a new cluster size insensitive FCM (csi-FCM) is presented in Chapter 4, which requires no extra parameters compared to traditional FCM. The csi-FCM algorithm is tested on different real multivariate images of potatoes and cold meats.

Combining spectral and spatial information

Although multivariate imaging offers possibilities to differentiate between both objects of similar spectra and different spatial correlations, existing unsupervised clustering techniques can not utilize this property. It is clear in case of overlapping clusters in the spectral domain, only the extra spatial information can discriminate between the different objects. The disadvantage of applying those unsupervised techniques as a multivariate image segmentation technique is that the information from the spatial domain is ignored. Only the spectral information determines the partitioning of the measurement space. Even if no a priori information about the spectra is available, information about the shape of the objects in the image is sometimes known. However, the majority of supervised and unsupervised classification techniques including traditional FCM cannot use this a priori spatial information during the clustering process without modification. Manuscripts about the combined use of spatial and spectral information for image segmentation have been reported in literature before [99, 100, 101, 102, 103, 104, 105, 106, 107, 108], except for FCM. In Chapter 2 and Chapter 3 different modifications of FCM are presented that utilize spatial information during the clustering.

Supervised classification

Unsupervised clustering techniques when used as a segmentation technique are able to partition the image in regions based on a user selected number of classes as long as the number of spectral bands are limited. The huge amount of data in multispectral images requires computational demands which are not feasible in most applications. This is especially true for the multispectral images as discussed in the applications above where the Imspector is used for the image acquisition. E.g. in certain applications, the number of bands ranges from 100-300 and a single 16 bit multispectral image contains about 84 Mbyte of data [65]. A widely used approach is to apply an unsupervised classifier to a small sample of the image data for the estimation of the classes and then classify the entire multivariate image using a supervised classifier trained with the estimated model [109]. It has been shown that this strategy leads to under or overestimated classes in the segmented image [110]. Furthermore, different samplings may result in different segmentation results due to the random nature of the sampling procedure. Therefore, in case of high dimensional data, supervised classification techniques are often used to classify the multispectral image. Supervised techniques require a labelled training set from which the class boundaries are determined. Usually, a representative training set must be obtained from the multispectral image set which can be a challenging task as there are multiple image bands to explore.

Multivariate image analysis

A procedure for selecting a representative training set and test set from multivariate images is based on Multivariate Image Analysis (MIA), as described thoroughly in literature [33]. MIA uses Principal Component Analysis (PCA) for dimension reduction and with three selected score images a pseudo color image is constructed which is used for visualization and region selection. By selecting regions in the pseudo color image, corresponding scores in the score plots can be visualized. The opposite is also possible, by selecting regions or clusters in score space, the corresponding pixel position in the pseudo image can be visualized. Although it was originally introduced as an interactive tool for the explorative analysis of multivariate images, the selected regions can be used as training or test set. The selected objects or scores can be extracted, backtransformed to original space, labelled and used as a labelled data set. The procedure must be repeated for each class in the multivariate image and the classes are combined to a training or test set. This procedure has been followed in several applications [40, 31, 111] for the selection of training and test sets.

Training and test set selection

However, with respect to the explorative analysis and classification of huge multispectral images of agricultural and food products several difficulties might occur. To select a training set from the multivariate image with the MIA procedure, an exact selection of regions is required which can be a challenging task. Due to spectral and spatial mixing, overlapping classes occur which makes the selection of a single class difficult. Likewise, it is not possible to verify that all relevant classes have been selected, due to dense classes and class overlap small defect classes may be overlooked and therefore will not be included in a training set. To prevent this, a thorough exploration of the multivariate image is required which can be time consuming as the amount of data shown in the score plots makes it difficult to recognize structure or grouped data. To overcome the aforementioned problems, a new Feedback Multivariate Model Selection (FEMOS) procedure for the estimation of classes in multivariate images has been developed. The procedure is described in Chapter 5 and is based on the principles of both unsupervised classification and the MIA approach and can be applied for the unsupervised segmentation of multivariate images or for training and test set estimation from multivariate images. The procedure is tested on different multispectral images of pot plants, wood and French fries.

1.2 Objective

The work in this thesis focusses on the development of techniques and methods for the detection of defects and diseases from multispectral images acquired from postharvest products. These images do not only have a huge number of spectral bands which makes exploration or training set selection for classification a challenging task, they also contain classes with small defects or abnormalities where objects of these classes are easily missed. The huge amount of data produced by these measurement systems require techniques and algorithms that can extract maximum information. Also, as the amount of data increases, techniques which can separate the relevant data out of the non-interesting data, become more necessary. A second important area of interest is the combined use of multivariate data analysis tools with image-processing algorithms. As multivariate data analysis tools usually process data in spectral domain and image processing routines mainly in the spatial domain, new territories can be explored where the combination of both fields can result in a set of new algorithms which are able to extract relevant data from an entire set better and more precisely.

1.3 Outline of the thesis

In Chapter 2 a modified version of the unsupervised Fuzzy C-Means (FCM) technique is presented which uses the combined spectral and spatial information during the clustering process. A generalized version of this technique, called spatial guided FCM (sg-FCM) is presented in Chapter 3.

The generalized version uses a geometrical shape model to describe a priori shape information which is used to guide the clustering process. Although FCM is a very popular technique for unsupervised multivariate image segmentation, the sensitivity for different cluster sizes is known as an important disadvantage. Especially when FCM is applied as a segmentation technique in postharvest quality inspection, where differences in cluster sizes are common due to small defects on the products. A new cluster size insensitive FCM (csi-FCM) has been developed to overcome this cluster size sensitivity and is presented in Chapter 4.

In Chapter 5 the csi-FCM is utilized in a new procedure for the estimation of classes in multivariate images. The Feedback Multivariate Model Selection (FEMOS)is discussed where positive characteristics of unsupervised, supervised and the MIA approach are combined in a single procedure.

Chapter 6 describes the detection and classification of defects and diseases on French fries where the best performing combination of data preprocessing and classifier are determined for the classification of both RGB color and multispectral images. The FEMOS procedure of Chapter 5 is used for the the extraction of training and test sets.

Finally, in Chapter 7 the conclusions are given and some future aspects of multivariate imaging for agricultural product inspection are discussed.

1.4 Publications

The work as described in the following chapters has been published as:

Chapter 2: J. C. Noordam and W. H. A. M. van den Broek, Multivariate image segmentation based on geometrically guided Fuzzy C-Means clustering, *Journal of Chemometrics*, vol. 16, pp. 1-11, 2002.

Chapter 3:	J. C. Noordam, W. H. A. M. van den Broek, and L. M. C. Buydens, Unsupervised segmentation of predefined shapes in multivariate images, *Journal of Chemometrics*, vol. 17, pp. 216-224, 2003. J. C. Noordam, W. H. A. M. van den Broek, and L. M. C. Buydens, Geometrically guided Fuzzy C-Means clustering for multivariate image segmentation, presented at *ICPR 2000, the 15th International Conference on Pattern Recognition*, Barcelona, Spain, 2000. J. C. Noordam, W. H. A. M. van den Broek, and L. M. C. Buydens, Geometrically guided Fuzzy C-Means clustering of multispectral images, presented at *SPIE, Multispectral and Hyperspectral Image Acquisition and Processing*, Wuhan, China, 2001.
Chapter 4:	J. C. Noordam, W. H. A. M. van den Broek, and L. M. C. Buydens, Multivariate image segmentation with cluster size insensitive Fuzzy C-means, *Chemometrics and Intelligent Laboratory Systems*, vol. 64, pp. 65-78, 2002.
Chapter 5:	J. C. Noordam, W. H. A. M. van den Broek, P. Geladi and L. M. C. Buydens, A new strategy for the modelling and representation of classes in multivariate images, accepted by *Chemometrics and Intelligent Laboratory Systems*.
Chapter 6:	J. C. Noordam, W. H. A. M. van den Broek, and L. M. C. Buydens, Detection and classification of latent defects and diseases on French fries with multispectral imaging, submitted to *Journal of the Science of Food and Agriculture*. J. C. Noordam, W. H. A. M. van den Broek, and L. M. C. Buydens, Perspective of inline control of latent defects and diseases on French fries with multispectral imaging, presented at *SPIE, Food Safety and Agricultural Monitoring*, Providence, Rhode Island, USA, 2003. J. C. Noordam, W. H. A. M. van den Broek, and L. M. C. Buydens, Influence of spectral preprocessing on the classification for latent defects and diseases on French fries with multispectral imaging, presented at *Agricultural Engineering 2004*, Leuven, Belgium, 2004.

Bibliography

[1] R. Shewfelt, “What is quality?,” *Postharvest Biology And Technology*, vol. 15, pp. 197–200, 1999.

[2] J. A. Abbott, “Quality measurement of fruits and vegetables,” *Postharvest Biology And Technology*, vol. 15, no. 3, pp. 207–225, 1999.

[3] T. Brosnan and D. W. Sun, “Inspection and grading of agricultural and food products by computer vision systems - a review,” *Computers and Electronics in Agriculture*, vol. 36, pp. 193–213, 2002.

[4] M. Graves and B. Batchelor, *Machine Vision for the Inspection of Natural Products*. London: Springer, 2003.

[5] B. Hills, “Food processing: An MRI perspective,” *Trends in Food Science & Technology*, vol. 6, no. 4, pp. 111–117, 1995.

[6] L. Hall, S. Evans, and K. Nott, “Measurement of textural changes of food by MRI relaxometry,” *Magnetic Resonance Imaging*, vol. 16, no. 5/6, pp. 485–492, 1998.

[7] M. McCarthy and K. L. McCarthy, “Applications of magnetic resonance imaging to food research,” *Magnetic Resonance Imaging*, vol. 14, no. 7/8, pp. 799–802, 1996.

[8] W. Laurent, J. Bonny, and J. Renou, “Muscle characterization by NMR imaging and spectroscopic techniques,” *Food Chemistry*, vol. 69, pp. 419–426, 2000.

[9] Z. Yan, M. J. McCarthy, L. Klemann, M. S. Otterburn, and J. Finley, “NMR applications in complex food systems,” *Magnetic Resonance Imaging*, vol. 14, no. 1/8, pp. 979–981, 1996.

[10] P. Barreiro, J. Ruiz-Cabello, M. Fernandez-Valle, M. Ortiz, and M. Ruiz-Altisent, “Mealiness assessment in apples using MRI techniques,” *Magnetic Resonance Imaging*, vol. 17, no. 2, pp. 275–281, 1999.

[11] B. Zion, P. Chen, and M. J. McCarthy, “Detection of bruises in magnetic resonance images of apples,” *Computers and Electronics in Agriculture*, vol. 13, pp. 289–299, 1985.

[12] K. P. Nott, S. D. Evans, and L. D. Hall, “Quantitative magnetic resonance imaging of fresh and frozen-thawed trout,” *Magnetic Resonance Imaging*, vol. 17, no. 3, pp. 445–455, 1999.

[13] T. M. Guiheneuf, A. D. Parker, J. J. Tessier, and L. D. Hall, “Authentication of the effect of freezing/thawing of pork by quantitative magnetic resonance imaging,” *Magnetic Resonance in Chemistry*, vol. 35, pp. 112–118, 1997.

[14] A. Horigane, H. Toyoshima, H. Hemmi, W. Engelaar, A. Okubo, and T. Nagata, “Internal hollows in cooked rice grains (oryza sativa cv. koshihikari) observed by NMR micro imaging,” *Journal of Food Science*, vol. 64, no. 1, pp. 1–5, 1999.

[15] P. Chen, M. J. McCarthy, and R. Kauten, “NMR for internal quality evaluation of fruits,” *Transactions of the ASAE*, vol. 32, no. 5, pp. 1747–1753, 1989.

[16] E. Finney and K. Norris, “X-ray images of hollow heart potatoes in water,” *American Potato Journal*, vol. 50, pp. 1–8, 1963.

[17] G. Birth, “How light interacts with food,” in *Quality Detection in Foods* (J. Gaffney Jr, ed.), (St. Joseph, MI), pp. 6–11, American Society for Agricultural Engineering, 1976.

[18] J. Noordam, A. Timmermans, G. Otten, and B. v. Zwol, “A colour vision system for high speed sorting of potatoes,” in *Agricultural Engineering 2000*, (Univeristy of Warwick, Warwick, England), 2000.

[19] S. Deck, C. Morrow, P. Heinemann, and H. Sommer, “Comparison of a neural network and traditional classifier for machine vision inspection of potatoes,” *Applied Engineering in Agriculture*, vol. 11, no. 2, pp. 319–326, 1995.

[20] P. Heinemann, N. Pathare, and C. Morrow, “An automated inspection station for machine-vision grading of potatoes,” *Machine Vision and Application*, vol. 9, pp. 14–19, 1996.

[21] N. Pathare, P. Heinemann, C. Morrow, and S.Deck, “Automated inspection station for grading of potatoes,” in *1993 International Summer Meeting of the ASAE*, (Spokane, Washington), 1993.

[22] Y. Tao, C. Morrow, P. Heinemann, and H. Sommer, “Automated machine vision inspection of potatoes,” in *1990 International Winter Meeting of the ASAE*, (Hyatt Regency Chicago, Illinois), 1990.

[23] L. Zhou, V. Chalana, and Y. Kim, “PC-based machine vision system for real-time computer-aided potato inspection,” *International Journal of Imaging Systems and Technology*, vol. 9, no. 6, pp. 423–433, 1998.

[24] Y. Tao, P. Heinemann, Z. Varghese, C. Morrow, and H. Sommer, “Machine vision for color inspection of potatoes and apples,” *Transactions of the ASAE*, vol. 38, no. 5, pp. 1551–1561, 1995.

[25] P. Heinemann, Z. Varghese, C. Morrow, and C. Crasweller, “Machine vision inspection of golden delicious apples,” *Applied Engineering in Agriculture*, vol. 11, no. 6, pp. 901–906, 1995.

[26] J. Li, J. Tan, F. Martz, and H. Heyman, “Image texture features as indicators of beef tenderness,” *Meat Science*, vol. 53, pp. 17–22, 1999.

[27] S. Deshpande, M. Cheryan, S. Gunasekaran, M. R. Paulsen, and D. Salunkhe, “Nondestructive optical methods of food quality evaluation,” *CRC Critical Reviews in Food Science and Nutrition*, vol. 2, no. 4, pp. 323–379.

[28] C. R. Bull, “A review of sensing techniques which could be used to generate images of agricultural and food materials,” *Computers and Electronics in Agriculture*, vol. 8, pp. 1–29, 1993.

[29] A. Jimenez, A. Jain, R. Ceres, and J. Pons, “Automatic fruit recognition : a survey and new results using range/attenuation images,” *Pattern Recognition*, vol. 32, no. 10, pp. 1719–1736, 1999.

[30] Y. Chen, K. Chao, and M. S. kim, “Machine vision technology for agricultural applications,” *Computers and Electronics Agriculture*, vol. 36, pp. 173–191, 2002.

[31] W. v. d. Broek, *Chemometrics in Spectroscopic Near Infrared Imaging for Plastic Material Recognition*. PhD thesis, Catholic University of Nijmegen, 1997.

[32] P. Williams and K. Norris, *Near-Infrared Technology in the Agricultural and Food Industries*. St. Paul, MN: American Association of Cereal Chemists, 1987.

[33] P. Geladi and H. Grahn, *Multivariate Image Analysis*. John Wiley & Sons Ltd., 1996.

[34] B. Park, Y. Chen, and R. Huffman, “Integration of visible/NIR spectroscopy and multispectral imaging for poultry carcass inspection,” *Journal of Food Engineering*, vol. 30, pp. 197–207, 1996. NIR.

[35] B. Park and Y. Chen, “Intensified multispectral imaging system for poultry carcass inspection,” *Transactions of the ASAE*, vol. 37, no. 6, pp. 1983–1988, 1994.

[36] B. Park and Y. Chen, “Multispectral image co-occurance matrix analysis for poultry carcasses inspection,” *Transactions of the ASAE*, vol. 39, no. 4, pp. 1485–1491, 1996.

[37] B. Park, K. C. Lawrence, W. R. Windham, Y. Chen, and K. Chao, “Discriminant analysis of dual-wavelength spectral images for classifying poultry carcasses,” *Computers and Electronics in Agriculture*, 2002.

[38] R. Zwingelaar, S. Yang, E. Garcia-Pardon, and C. R. Bull, “Use of spectral information and machine vision for bruise detection on peaches and apricots,” *Journal of Agricultural Engineering Research*, vol. 63, pp. 323–332, 1996.

[39] S. Chen and M.-T. Li, “Multispectral imaging of chlorophyll content for vegetable status monitoring,” in *Fruit, Nut and Vegetable Production Engineering* (M. Zude, B. Herold, and M. Geyer, eds.), (Potsdam), pp. 603–608, Institut fur Agrartechnik Bornim e.V., 2001.

[40] J. Wold, F. Westad, and K. Heia, “Detection of parasites in cod fillets by using SIMCA classification in multispectral images in the visible and NIR region,” *Applied Spectroscopy*, vol. 55, no. 8, pp. 1025–1034, 2001.

[41] J. P. Wold, *Rapid Quality Assessment of Meat and Fish by Using Near-Infrared Spectroscopy Autofluorescence Spectroscopy and Image Analysis*. PhD thesis, Agricultural University of Norway, 2000.

[42] J. Sugiyama, “Visualisation of sugar content in the flesh of a melon by near-infrared imaging,” *Journal of Agricultural and Food Chemistry*, vol. 47, pp. 2715–2718, 1999.

[43] N. Gat, “Imaging spectroscopy using tunable filter based cameras,” 2000.

[44] N. Gat, “Imaging spectroscopy using tunable filters: a review,” in *Wavelet Applications VII*, vol. 4056, pp. 50–64, SPIE, 2000.

[45] M. Evans, C. Thai, and J. Grant, “Development of a spectral imaging system based on a liquid crystal tunable filter,” *Transactions of the ASAE*, vol. 41, no. 6, pp. 1845–1852, 1998.

[46] M. Evans, C. Thai, and J. Grant, “Performance of dual-wavelength liquid crystal tunable filter,” in *1998 ASAE Annual International Meeting*, (Orlando, Florida), ASAE, 1998.

[47] Y. Inoue and J. Penuelas, “An AOTF-based hyperspectral imaging system for field use in ecophysiological and agricultural applications,” *International Journal of Remote Sensing*, vol. 22, no. 18, pp. 3883–3888, 2001.

[48] W. Miller, J. Throop, and B. Upchurch, “Pattern recognition models for spectral reflectance evaluation of apple blemishes,” *Postharvest Biology and Technology*, vol. 14, pp. 11–20, 1998.

[49] C. Thai, S. Kays, and J. C. Grant, “Mapping light penetration into fruits using a liquid crystal tunable filter,” in *1997 ASAE Annual International Meeting*, (Minneapolis, Minnesota), 1997.

[50] B. Novales, D. Bertrand, M.-F. Devaux, P. Robert, and A. Sire, “Multispectral fluorescence imaging for the identification of food products,” *Journal of the Science of Food and Agriculture*, vol. 71, pp. 376–382, 1996. NIR.

[51] C. Thai, M. Evans, and J. Grant, “Herbicide stress detection using liquid crystal tunable filter,” in *1997 ASAE Annual International Meeting*, (Minneapolis,Minnesota), 1997. paper no. 973142.

[52] N. Aleixos, J. Blasco, F. Navarron, and E. Molt, “Multispectral inspection of citrus in real-time using machine vision and digital signal processors,” *Computers and Electronics in Agriculture*, vol. 33, pp. 121–137, 2002.

[53] Redlake, “Multispectral imaging in food and agriculture.” Website, 2003. `http://www.redlake.com/spectral/tech_articles/food_inspection.html`.

[54] G. Polder, G. W. A. M. van der Heijden, L. C. P. Keizer, and I. T. Young, “Calibration and characterization of imaging spectrographs,” *Journal of near Infrared Spectroscopy*, vol. 11, pp. 193–210, 2003.

[55] K. Lawrence, W. Windham, P. Park, and D. Smith, “Comparison between visible/NIR spectroscopy and hyperspectral imaging for detecting surface contaminants,” in *SPIE, Food Safety and Agricultural Monitoring* (Y. R. Chen and G. E. Meyer, eds.), vol. 5271, (Providence, Rhode Island USA), SPIE, 2003.

[56] P. Park, W. Windham, K. Lawrence, and D. Smith, “Classification of hyperspectral imagery for identifying fecal and ingesta contaminants,” in *SPIE, Food*

Safety and Agricultural Monitoring (Y. Chen and G. E. Meyer, eds.), vol. 5271, (Providence, Rhode Island USA), SPIE, 2003.

[57] K. C. Lawrence, W. R. Windham, B. Park, and J. Buhr, “Hyperspectral imaging for poultry contaminant detection,” *NIR News*, vol. 12, no. 5, pp. 3–6, 2001.

[58] K. C. Lawrence, B. Park, W. R. Windham, and C. Mao, “Calibration of imaging spectrometry system for inspection of contaminated poultry carcasses,” in *Annual International Meeting* (ASAE, ed.), vol. 01-3129, (Sacramento, California), ASAE, 2001.

[59] K. C. Lawrence, B. Park, D. P. Smith, W. R. Windham, and P. Feldner, “Hyperspectral system calibration for improved contaminant detection on poultry carcasses,” in *Annual International Meeting* (ASAE, ed.), vol. 023063, (Hyatt Regency Chicago), ASAE, 2002.

[60] J. Wold and K. Kvaal, “Mapping lipid oxidation in chicken meat by multispectral imaging of autofluorescence,” *Applied Spectroscopy*, vol. 54, no. 6, pp. 900–909, 2000.

[61] K. Chao, P. M. Mehl, and Y. Chang, “Use of hyper- and multi-spectral imaging for detection of chicken skin tumors,” *Applied Engineering in Agriculture*, vol. 18, no. 1, pp. 113–119, 2002.

[62] D. Casasent and S. Nakaryakul, “Hyperspectral feature selection for detection of chicken skin tumors,” in *SPIE, Food Safety and Agricultural Monitoring* (Y. R. Chen and G. E. Meyer, eds.), vol. 5271, (Providence, Rhode Island USA), SPIE, 2003.

[63] K. Shiranita, T. Miyajima, and R. Takiyama, “Determination of meat quality by texture analysis,” *Pattern Recognition Letters*, vol. 19, no. 12, pp. 1319–1324, 1998.

[64] J. P. Wold, K. Kvaal, and B. Egelandsdal, “Quantification of intramuscular fat content in beef by combining autofluorescence spectra and autofluorescence,” *Applied Spectroscopy*, vol. 53, no. 4, pp. 448–456, 1999. NIR.

[65] G. Polder, G. van der Heijden, and I. Young, “Spectral image analysis for measuring ripeness of tomatoes,” *Transactions of the Asae*, vol. 45, pp. 1155–1161, 2002.

[66] D. Guyer and X. Yang, “Use of genetic artificial neural networks and spectral imaging for defect detection on cheries,” *Computers and Electronics in Agriculture*, vol. 29, pp. 179–194, 2000.

[67] P. M. Mehl, K. Chao, M. Kim, and Y. Chen, "Detection of defects on selected apple cultivars using hyperspectral and multispectral image analysis," *Applied Engineering in Agriculture*, vol. 18, no. 2, pp. 219–226, 2002.

[68] D. E. Guyer and Z. Yang, "Identifying apple defects by utilizing spectral imaging fluorescence and genetic neural networks," in *2000 ASAE Annual International Meeting*, (Milwaukee, Wisconsin), 2000.

[69] R. Lu, "Near infrared multispectral scattering for assessing internal quality of apple fruit," in *SPIE, Food Safety and Agricultural Monitoring* (Y. R. Chen and G. E. Meyer, eds.), vol. 5271, (Providence, Rhode Island USA), SPIE, 2003.

[70] D. Ariana, D. Guyer, and B. Shresta, "Near infrared multispectral scattering for assessing internal quality of apple fruit," in *SPIE, Food Safety and Agricultural Monitoring* (Y. R. Chen and G. E. Meyer, eds.), vol. 5271, (Providence, Rhode Island USA), SPIE, 2003.

[71] P. Martinsen and P. Schaare, "Measuring soluble solids distribution in kiwifruit using near-infrared imaging spectroscopy," *Postharvest Biology and Technology*, vol. 14, no. 3, pp. 271–281, 1998.

[72] B. Upchurch and C. Thai, "Spectral characterization of Pecan weevil larvae and Pecan nutmeat using multispectral imaging," in *2000 ASAE Annual International Meeting*, (Milwaukee, Wisconsin), 2000.

[73] S. Delwiche and M. S. kim, "Hyperspectral imaging for detection of scab in wheat," in *Biological Quality and Precision Agriculture II* (J. A. DeShazer and G. E. Meyer, eds.), vol. 4203, pp. 13–20, Proceedings of SPIE, 2000.

[74] D. Casasent and X. Che, "Aflatoxin detection in whole corn kernels using hyperspectral methods," in *SPIE, Food Safety and Agricultural Monitoring* (Y. R. Chen and G. E. Meyer, eds.), vol. 5271, (Providence, Rhode Island USA), SPIE, 2003.

[75] J. Bezdek, *Pattern Recognition with Fuzzy Objective Functions*. New York: Plenum Press, 1981.

[76] J. Bezdek, L. Hall, and L. Clarke, "Review of MR image segmentation techniques using pattern recognition," *Medical Physics*, vol. 20, no. 4, pp. 1033–1048, 1993.

[77] A. M. Bensaid, *Improved Fuzzy Clustering for Pattern Recognition with Applications to Image Segmentation*. PhD thesis, South Florida, 1994.

[78] M. R. Rezaee, *Application of Fuzzy Techniques in Image Segmentation*. PhD thesis, University of Leiden, 1998.

[79] A. Baraldi and P. Blonda, “A survey of fuzzy clustering algorithms for pattern recognition - part 2,” *IEEE Transactions on Systems, Man and Cybernetics*, vol. 29, no. 6, pp. 786–801, 1999.

[80] M. Yang, “A survey of fuzzy clustering,” *Mathematical and Computer Modelling*, vol. 18, no. 11, pp. 1–16, 1993.

[81] J. E. Malek, A. M. Alim, and R. Tourki, “Problems in pattern classification in high dimensional spaces: Behavior of a class of combined neuro-fuzzy classifiers,” *Fuzzy Sets and Systems*, vol. 128, pp. 15–33, 2002.

[82] C. Lee and D. A. Landgrebe, “Analyzing high dimensional multispectral data,” *IEEE Transactions on Geoscience and Remote Sensing,*, vol. 31, pp. 792–800, 1993.

[83] D. Landgrebe, “Some fundamentals and methods for hyperspectral image data analysis,” in *Systems and Technologies for Clinical Diagnostics and Drug Discovery II*, (G. Cohn and J. Owicki, eds.), vol. 3603, Proceedings of SPIE, 1999.

[84] T. Næs and B. Mevik, “The flexibility of fuzzy clustering illustrated by examples,” *Journal of Chemometrics*, vol. 13, pp. 435–444, 1999.

[85] L. Hall, A. Bensaid, L. Clarke, R. Velthuizen, M. Silbiger, and J. Bezdek, “A comparison of neural network and fuzzy clustering techniques in segmenting magnetic resonance images of the brain,” *IEEE Transactions on Neural Networks*, vol. 3, no. 5, pp. 672–682, 1992.

[86] M. Goldberg and S. Shlien, “A clustering scheme for multispectral images,” *IEEE Transactions on Systems, Man and Cybernetics*, vol. 8, no. 2, pp. 86–92, 1978.

[87] R. L. Cannon, J. V. Dave, and J. Bezdek, “Efficient implementation of the Fuzzy C-Means clustering,” *IEEE Transactions on Pattern Analysis and Machine Intelligence*, vol. 8, no. 2, 1986.

[88] R. Cannon, J. Dave, and J. Bezdek, “Segmentation of a thematic mapper image using the Fuzzy C-Means clustering algorithm,” *IEEE Transactions on Geoscience and Remote Sensing*, vol. 24, no. 3, pp. 400–408, 1986.

[89] A. Ouahab Boudraa, “Automated detection of the left ventricular region in magnetic resonance images by Fuzzy C-Means model,” *International Journal of Cardiac Imaging*, vol. 13, pp. 347–355, 1997.

[90] J. R. Mansfield, M. G. Sowa, G. B. Scarth, R. L. Somorjai, and H. H. Mantsch, “Analysis of spectroscopic imaging data by Fuzzy C-Means clustering,” *Analytical Chemistry*, vol. 69, pp. 3370–3374, 1997.

[91] J. R. Mansfield, M. G. Sowa, C. Majzels, C. Collins, E. Cloutis, and H. A. Mantsch, “Near infrared spectroscopic reflectance imaging : Supervised versus unsupervised analysis using an art conservation application,” *Vibrational Spectroscopy*, vol. 19, pp. 33–45, 1999.

[92] J. R. Mansfield, M. G. Sowa, J. R. Payette, N. Abdulrauf, M. F. Stranc, and H. H. Mantsch, “Tissue viability by multispectral near infrared imaging: A Fuzzy C-Means clustering analysis,” *IEEE Transactions on Medical Imaging*, vol. 17, no. 6, 1998.

[93] J. R. Mansfield, M. G. Sowa, G. B. Scarth, R. L. Somorjai, and H. H. Mantsch, “Fuzzy C-Means clustering and principal component analysis of time series from near-infrared imaging of forearm ischemia,” *Computerized Medical Imaging and Graphics*, vol. 21, no. 5, 1997.

[94] N. Kehtarnavaz, M. Chung, L. Hayman, and R. , Wendt III, “Magnetic resonance image segmentation by contextual fuzzy clustering,” *Journal of Intelligent and Fuzzy Systems*, vol. 1, pp. 295–305, 1994.

[95] M. Vaidyanathan, L. Clarke, C. Heidtman, R. P. Velthuizen, and L. Hall, “Normal brain volume measurements using multispectral MRI segmentation,” *Magnetic Resonance Imaging*, vol. 15, no. 1, pp. 87–97, 1997.

[96] M. Trivedi and J. C. Bezdek, “Low-level segmentation of aerial images with fuzzy clustering,” *IEEE Transactions on Systems, Man and Cybernetics*, vol. 16, no. 4, pp. 589–598, 1986.

[97] I. Gath and A. Geva, “Unsupervised optimal fuzzy clustering,” *IEEE Transactions on Pattern Analysis and Machine Intelligence*, vol. 11, no. 7, pp. 773–781, 1989.

[98] A. M. Bensaid, L. O. Hall, J. Bezdek, and L. Clarke, “Partially supervised clustering for image segmentation,” *Pattern Recognition*, vol. 29, no. 5, pp. 859–871, 1996.

[99] P. Paclik, R. P. W. Duin, and G. van Kempen, “Multi-spectral image segmentation algorithm combining spatial and spectral information,” in *SCIA 2001*, (Bergen, Norway), 2001.

[100] S. Roberts, G. Gisler, and J. Theiler, “Spatial-spectral image analysis using classical and neural algorithms,” Proceedings of the Artificial Neural Networks in Engineering, pp. 425–430, ASME Press, New York, 1996.

[101] J. Besag, “On the statistical analysis of dirty pictures,” *Journal of the Royal Statistical Society*, vol. 48, no. 3, pp. 259–302, 1986.

[102] S. Geman and D. Geman, “Stochastic relaxation, gibbs distributions and the bayesian restoration of images,” *IEEE Transactions on Pattern Analysis and Machine Intelligence*, vol. 6, no. 6, pp. 721–741, 1984.

[103] J. Kittler and J. Föglein, “Contextual classification of multispectral pixel data,” *Image and Vision Computing*, vol. 2, no. 1, pp. 13–29, 1984.

[104] A. Sarkar, M. K. Biswas, B. Kartikeyan, V. Kumar, K. Majumder, and D. Pal, “A MRF model-based segmentation approach to classification for multispectral imagery,” *IEEE Transactions on Geoscience and Remote Sensing*, vol. 40, no. 5, pp. 1102–1113, 2002.

[105] N. R. Harvey, J. Theiler, S. P. Brumby, S. Perkens, J. J. Szymanski, J. J. Bloch, R. B. Porter, M. Galassi, and A. C. Young, “Comparison of GENIE and conventional supervised classifiers for multispectral image feature extraction,” *IEEE Transactions on Geoscience and Remote Sensing*, vol. 40, no. 2, pp. 393–404, 2002.

[106] D. Landgrebe, “The development of a spectral-spatial classifier for earth observational data,” *Pattern Recognition*, vol. 12, pp. 165–175, 1980.

[107] S. Sanjay-Gopal and T. J. Hebert, “Bayesian pixel classification using spatially variant finite mixtures and the generalized EM algorithm,” *IEEE Transactions on Image Processing*, vol. 7, no. 7, pp. 1014–1028, 1998.

[108] T. Tran, R. Wherens, and L. Buydens, “SpaRef: A clustering algorithm for satellite imagery,” *Analytica Chimica Acta*, vol. 490, pp. 303–312, 2003.

[109] J. Banfield and A. Raftery, “Model-based gaussian and non-gaussian clustering,” *Biometrics*, vol. 49, pp. 803–821, 1993.

[110] R. Wherens, L. Buydens, C. Fraley, and A. Raftery, “Model-based clustering for image segmentation and large datasets via sampling,” Technical report 424, Department of Statistics, University of Washington, February 13 2003.

[111] J. Witjes, *Explorative Analysis of Chemometrics in Magnetic Resonance (Spectroscopic) Imaging of Human Brain Tumors*. PhD thesis, Catholic University of Nijmegen, 2001.

Chapter 2

Multivariate image segmentation based on geometrically guided Fuzzy C-Means clustering

Abstract

This paper describes a new approach to geometrically guided fuzzy clustering. A modified fuzzy C-Means clustering (FCM), Conditional FCM, is extended to incorporate a priori geometrical information from the spatial domain in order to improve image segmentation. This leads to a new algorithm (ggc-FCM) where the cluster guidance is determined by the membership values of neighboring pixels. The ggc-FCM is tested on synthetic and real images to demonstrate the improved image segmentation compared to traditional FCM.

2.1 Introduction

The use of pattern recognition techniques to segment a multivariate image in meaningful regions has been reported in literature [1, 2, 3]. One of those techniques, widely used in multivariate imaging, is Fuzzy C-Means clustering (FCM) [4]. It is known as an unsupervised fuzzy clustering technique that uses the raw measurement data in order to reveal the underlying structure of the data and segment the image in regions with similar spectral properties. When FCM is applied as a clustering technique in multivariate imaging, the relationship between pixels in the spatial domain is completely ignored. The partitioning of the measurement space depends on the spectral information only. When geometrical information is used during the clustering process possible segmentation errors can be corrected during clustering by utilizing the information from the spatial domain. Furthermore, when two overlapping clusters in the spectral domain correspond to two different objects in the spatial domain, usage of a priori spatial information can improve the separation of these two overlapping clusters. An example of multispectral images with overlapping spectral information are images produced by a computer based potato inspection system [5]. The inspection system uses standard 3-CCD color camera's for the image capturing. The obtained images are noisy and contain overlapping spectra for certain similar colored defects. Without the use of additional spatial information, the segmentation procedure cannot discriminate between the similar colored potato defects. As a consequence, the classification procedure rejects the potato based on the wrong segmentation results. In order to add spatial information, a modification of the FCM algorithm is necessary because the traditional FCM is not suitable to add a priori information into the clustering process. Many modifications and variants of FCM have been presented [6], where the FCM is modified to search for a specific structure in the data, e.g. lines, ellipsoids or c-shells. However, these algorithms impose a certain structure to the partition that they generate. In cases where spatial information is combined with spectral information, both techniques are used sequentially [7, 8, 9]. In these applications, the initial segmentation, which is performed by the spectral based FCM algorithm is followed by a spatially based algorithm which tries to correct the segmentation errors. However, the subsequent spatial based algorithm cannot correct the already present segmentation results directly. In literature, several ideas have been presented to add a priori information in the objective function of FCM [10, 11]. One approach is to split the objective function in a supervised term and an unsupervised term, where membership values of known labels are set beforehand [11]. Additional weight terms may be used to enhance or weaken objects with a specific label. The user must select the objects that receive a weight factor and also determine the value for this weight factor. This user intervention requires a priori information about the final classes of the objects, which may not always be available. In this paper, a modification of the unsupervised fuzzy clustering technique, called Conditional FCM (C-FCM) [12], is utilized to guide the clustering process by an auxiliary variable. The c-FCM algorithm uses this auxiliary variable to influence the contribution of each object to the final position of the cluster prototypes. Because this variable is used to condition the cluster prototypes, it is called condition [12]. The value of the condition variable for each pixel is determined by the neighboring pixels in the spatial domain. This makes it possible to guide the clustering process based on spatial relationships. After each iteration step of the clustering process in the spectral domain, the condition for each pixel is updated. Influencing the segmentation results takes place during the segmentation process itself and not afterwards. This is the difference with the techniques discussed above. The determination of the condition is based on the membership values of the neighboring pixels in the spatial domain. Thus, the Geometrically Guided Conditional FCM (ggc-FCM) swaps between the spectral domain and the spatial domain during the clustering process. A priori spatial information such as a certain shape or size of objects in an multivariate image can now be used during clustering in order to improve the segmentation results. The paper is organized as follows: In section 2.2, the FCM algorithm and the modified Conditional-FCM algorithms are explained. Next, the theory of the ggc-FCM is presented. Section 2.4 shows the results of experiments of ggc-FCM compared to traditional FCM. A priori information such as spurious pixels and blob size is used during ggc-FCM clustering to improve the segmentation results. Multivariate RGB images obtained from a camera based potato inspection system are segmented with ggc-FCM algorithm to distinguish between similar colored objects on the potato. In the last section, the conclusions and further research are discussed.

2.2 Conditional Fuzzy C-Means clustering (C-FCM)

2.2.1 Fuzzy C-Means clustering

Given a set of n data patterns,$X = \mathbf{x}_1, ..., \mathbf{x}_n$, the FCM algorithm minimizes the weighted within group sum of squared error objective function $J(U,\mathbf{V})$ [4] :

$$J(U,\mathbf{V}) = \sum_{k=1}^{n}\sum_{i=1}^{c} u_{ik}^{m} d^2(\mathbf{x}_k,\mathbf{v}_i) \tag{2.1}$$

where $\mathbf{x}_k$ is the $k\text{-}th$ p-dimensional data vector, $\mathbf{v}_i$ is the prototype of the center of cluster i, u_{ik} is the degree of membership of $\mathbf{x}_k$ in the $i\text{-}th$ cluster, m is a weighting exponent on each fuzzy membership, mostly m=2 is used [4], $d^2(\mathbf{x}_k,\mathbf{v}_i)$ is a distance measure between object $\mathbf{x}_k$ and cluster center $\mathbf{v}_i$, n is the number of objects and c is the number of clusters. A solution of the objective function $J(U,\mathbf{V})$ can be obtained via an iterative process where the degrees of membership u_{ik} and the cluster centers $\mathbf{v}_i$ are updated via:

$$u_{ik} = \frac{1}{\sum_{j=1}^{c} \left(\frac{d_{ik}}{d_{ij}} \right)^{\frac{2}{m-1}}} \tag{2.2}$$

$$\mathbf{v}_i = \frac{\sum_{k=1}^{n} u_{ik}^{m} \mathbf{x}_k}{\sum_{k=1}^{n} u_{ik}^{m}} \tag{2.3}$$

with the constraints :

$$u_{ik}\, \varepsilon\, [0,1], \qquad \sum_{i=1}^{c} u_{ik} = 1 \quad \forall k, \qquad 0 < \sum_{k=1}^{n} u_{ik} < N \quad \forall i \tag{2.4}$$

2.2.2 Conditional Fuzzy C-Means clustering

Clustering is usually seen as an unsupervised routine where no information about the underlying structure of the patterns is known. In cases where clustering is used and some labelled patterns (e.g. edges) are available, it might be advantageous to use these labelled patterns to influence the clustering process. In literature [12], this fundamental is used in Conditional FCM, a FCM based clustering technique where the clustering is guided by an auxiliary variable to guide the outcome of the clustering process. For each labelled pattern $\mathbf{x}_k$, an auxiliary condition f_k exists, where f_k ranges from [0,1]. The update procedure for the partition matrix **U** is now changed into:

$$u_{ik} = \frac{f_k}{\sum_{j=1}^{c} \left(\frac{d_{ik}}{d_{ij}} \right)^{\frac{2}{m-1}}} \tag{2.5}$$

with the modified constraint

$$\sum_{i=1}^{c} u_{ik} = f_k \tag{2.6}$$

For condition values equal to 1, the partition update procedure is similar to the partition update procedure of the traditional FCM. A small value of the condition results in a low membership value. A low membership value minimizes the contribution of that particular object to the cluster center. If the condition is set to zero, the influence of that object to the update procedure is neglected.

2.3 Geometrically guided conditional Fuzzy C-Means clustering

2.3.1 Principle of ggc-FCM

In case of clustering multivariate images with a traditional FCM algorithm, the spatial relationships between the pixels is not used during clustering. The construction of cluster prototypes is solely based on the distances in measurement space. The rationale of ggc-FCM is to use spatial relationship during the construction of the cluster prototypes. This means that both the spectral and spatial neighborhood of a pixel determine the contribution of a pixel to a cluster prototype. A spatial neighborhood window W around the pixel under consideration compares the majority class of the neighboring pixels with the class of the pixel under consideration to indicate whether a pixel matches its neighborhood. This comparison is based on membership values and results in a condition value for the pixel under consideration. The value of the condition indicates the similarity of the pixel compared to surrounding neighbors. The condition is high when the surrounding pixels have similar membership values and the condition is low when surrounding pixels have deviate membership values. The condition procedure is not performed for each cluster. Only the cluster of the neighborhood majority has to be considered as this is most likely the cluster where the pixel will be assigned to in the defuzzification process. The cluster of neighborhood majority is called the *iMax* cluster and the membership values for this cluster determine the condition. Thus, the ggc-FCM algorithm swaps between the spectral domain and the spatial domain during clustering. To prevent false removal of edge pixels, an edge preserving threshold must be exceeded before the condition procedure is performed. The procedure to select this value is discussed in section 2.3.4. To remove spatial outliers and noise pixels, the defuzzification procedure uses an *OutlierThreshold* to remove pixels with a condition value below this *OutlierThreshold* value. The selection for a correct value for the *OutlierThreshold* is discussed in section 2.3.6.

2.3.2 FCM clustering on multivariate images

A multivariate image is a stack of congruent two-dimensional images of a single scene where each image in the stack is measured for a different variable, e.g. wavelength. The number of rows (*nr*) and columns (*nc*) of the image define the horizontal and vertical dimensions of the three-dimensional image stack and the number of variables (*p*), determines the height of the stack. It is usually necessary for practical reasons to rearrange this three dimensional stack of images into a two-dimensional matrix [13]. All two-dimensional images are rearranged into a one-dimensional vector of *nr*x*nc* objects, called pixels. These rearranged images measured at p variables are combined to a two-dimensional data matrix $\mathbf{X}_{nrnc,p}$. This rearranging of matrices is called unfolding and the reverse operation is called back-folding. The number of rows of the partition matrix **U** is equal to the number of rows of the data matrix **X**. The columns of **U** are defined by c, the number of clusters. Backfolding a column of the **U** matrix with length *nr*x*nc* results in a two-dimensional image with *nr* rows and *nc* columns. The c columns of the partition matrix correspond to c backfolded images. The obtained images are called partition images and are used for the determination of the spatial neighborhood and the condition value of a pixel. Summarizing, partition image i is the backfolded column i of partition matrix **U** and corresponds with cluster i.

2.3.3 Fuzzy neighborhood

As discussed in section 2.3.1, only the cluster with maximum sum of neighboring membership values is considered to determine the condition of a pixel (*iMax*). To determine the majority class of neighboring pixels, the membership values covered by the neighborhood window W are added for each partition image i. The partition image i with the highest sum of membership values within the window W is considered as the class the pixel under investigation belongs to. To obtain *iMax*, a vector $\mathbf{sum\_u_{rc}}$, consisting of membership summations within the window W for a given position (r,c) in the image is created :

$$\mathbf{sum\_u_{rc}} = (sum\_u_1, \ldots, sum\_u_c) \quad \text{where} \quad sum\_u_i = \sum_{r'c' \varepsilon W} u_{r'c',i}\, ; \forall i = 1, \ldots, c \tag{2.7}$$

and the index of $\mathbf{sum\_u_{rc}}$ with the maximum sum_u_i is called *iMax* :

$$iMax = i \mid \max_i(\mathbf{sum\_u_{rc}}) \tag{2.8}$$

where W is a neighborhood window with (odd) size s, $u_{r'c',i}$ is the degree of membership of the neighbor pixel at position (r',c') in the window W of partition image i. Now that the majority cluster *iMax* of the spatial neighborhood is known, the mean membership deviation Δm between the pixel under investigation and its neighbors in window W of the *iMax* cluster is determined:

$$\Delta m_{rc,imax} = \frac{1}{s^2-1} \sum_{r'c' \varepsilon W} \left| u_{rc,imax} - u_{r'c',imax} \right| \tag{2.9}$$

where $\Delta m_{rc,imax}$ is the mean membership deviation for the pixel at position (r,c) of partition image *iMax*, $u_{rc,iMax}$ is the degree of membership of the center pixel in the window W of partition image $iMax$. The final condition for a pixel located at position (r,c) in the center of window W is obtained via a multiplication of $\Delta m_{rc,imax}$ with the membership value $u_{rc,imax}$ of the pixel at position (r,c):

$$f_{rc} = \Delta m_{rc,imax}\, u_{rc,imax} \tag{2.10}$$

where f_{rc} is the condition for the pixel at position (r,c). Multiplication of Δm with u_{rc} weakens the condition values in case of low values of u_{rc}. The result of this is that pixels with low membership values, such as outliers, are conditioned more strongly than higher membership values. In the remainder of this paper, $\Delta m_{rc,imax}$ is referred to as Δm and $u_{rc,iMax}$ is referred to as u_{rc}.

2.3.4 Edge preserving threshold

Edges may cause a false increment of the mean membership deviation (Δm) if the window W is positioned at a transition between two image planes. The membership values of the pixels in the window W will deviate as the pixels in the window belong to different classes. As a result, edge pixels receive a low condition value. To prevent this, the procedure as described above is extended with an extra threshold which must be exceeded before pixels are conditioned. With this extension, it is assumed that the mean membership deviation (Δm) is not caused by edge transitions. This edge preserving threshold, further referred to as *EdgeThreshold*, depends on the size of the window W. The *EdgeThreshold* value is determined as follows :

$$EdgeThreshold = \frac{floor(\frac{s}{2})\,s}{s^2 - 1} \tag{2.11}$$

where s is the odd size of a square window W. For a 3x3 window, this value is 0.375. Only when Δm exceeds this *EdgeThreshold* value, the condition value is calculated. Pixels with a condition value below this *EdgeThreshold* value keep their original condition value.

2.3.5 Defuzzification

Once the ggc-FCM procedure is stopped, the fuzzy partition matrix **U** must be defuzzified to a hard partition matrix to obtain a final classification of the pixels. Usually, the procedure of maximum membership is used for the conversion. The procedure of maximum membership will assign a class label to all pixels, even to pixels with extreme low condition values. This is undesirable, as even spatial outlier pixels with low condition values (f_{rc}) would be assigned to a class. Therefore, pixels with a condition lower than a predefined threshold value, further referred to as *OutlierThreshold*, are assigned to the reject class. Pixels assigned to the reject class have no contribution to the final position of any cluster prototype. The reject class is a collection of pixels with condition values below the *OutlierThreshold*. The reject class is not an extra class which is used during clustering with the ggc-FCM procedure, it is just an extra class during the defuzzification procedure. This *OutlierThreshold* procedure makes it possible to remove spatial outliers with low condition values. The procedure to determine a optimal value for the *OutlierThreshold* will be discussed in the next section.

2.3.6 Determination of OutlierThreshold value

To determine the *OutlierThreshold* value, the coherence between Δm, u_{rc} and f_{rc} must be understood. According to equation 2.9, Δm depends on the membership values of neighbouring pixels and the membership value u_{rc} of the pixel under investigation. The range for Δm is [*EdgeThreshold*,1] and the range for u_{rc} is [0,1]. As a result, the value for the condition f_{rc} ranges from [0,*EdgeThreshold*], according to equation 2.10. In case of defuzzification, this is also the range for the *OutlierThreshold* value. Combinations of variables can be excluded beforehand in case of spatial outliers, which makes it easier to select an optimal value for the the *OutlierThreshold*. First, as discussed in section 2.3.3, only the *iMax* cluster is considered, which means that for this particular cluster the neighboring pixels have high membership values. As a consequence of this, a spatial outlier pixel must have a low value for u_{rc}, otherwise a high value for Δm is not possible (equation 2.9). After all, a high value for Δm is required to exceed *EdgeThreshold* value (section 2.3.4). The abovementioned constraints show that an optimal value for the *OutlierThreshold* is a combination of Δm and u_{rc} and is in the range [0,*EdgeThreshold*]. To verify this, the situations as summarized in table 2.1 will be discussed. Situation 1 is typical for spatial outliers, a high value for Δm, which indicates the deviation between the center pixel and its neighbors, is accompanied with a low value for u_{rc}, which indicates a low cluster membership for the current cluster *iMax*. Since the resulting f_{rc} value is

no.	Δm	u_{rc}	f_{rc}
1	1	0	0
2	*EdgeThreshold*	0	0
3	*EdgeThreshold*	1	*EdgeThreshold*

Table 2.1: *Upper and lower bounds for* Δm *and* u_{rc}.

low, these spatial outliers can be removed with a low value for the *OutlierThreshold*. Situations 2 and 3 indicate that the center pixel is not a convincing spatial outlier (Δm=*EdgeThreshold*), as the center pixel and its neighbors deviate just enough for Δm to exceed the *EdgeThreshold* value. Situation 2 is more or less the opposite of situation 1, which described a typical spatial outlier. This makes situation 2 not likely to occur in case of a spatial outlier. A pixel with u_{rc}=1, as shown in situation 3, is also not a spatial outlier. To explain this, the combination of high neighboring membership values (due to the *iMax* cluster) and a high value for u_{rc} already indicates that the pixel is not an outlier. In case of a spatial outlier, a maximum value for u_{rc}=0.5 is expected because it is unlikely that a $\Delta m \geq$*EdgeThreshold* is accompanied with a $u_{rc} >$ 0.5 (again, see equation 2.9). The value of u_{rc}=0.5 is the turning point where, in case of the *iMax* cluster, a transition takes place from outlier to no outlier. Therefore, for situation 3, the maximum of u_{rc} is considered as being 0.5 in case of spatial outliers. The corresponding value of the f_{rc} is than a proper value for the *OutlierThreshold* :

$$OutlierThreshold = EdgeThreshold * 0.5 \tag{2.12}$$

In section 2.4, the results of experiments are shown to verify this value of the *OutlierThreshold*.

2.4 Experiments

To show the improvements of the ggc-FCM compared to traditional FCM, experiments have been carried out. The algorithm is tested on synthetic and real multivariate (RGB) images and the results are compared with the results of the traditional FCM. In all experiments, the fuzzy partition is converted to a crisp partition by applying the procedure of maximum membership. In case of ggc-FCM, this procedure is extended with the *OutlierThreshold*.

2.4.1 Experiment 1a: Removal of spurious pixels in a synthetic image

The artificial image (140x70 pixels) consists of two squares of similar colour (R=150, G=50, B=50) on a different background color (R=125, G=75, B=50). To verify that the outcome of the clustering results is not influenced by unequal cluster sizes, which is a known pitfall of FCM, the amount of foreground pixels (5000) is in balance with the amount of background pixels (4940). The image is contaminated with Gaussian noise to simulate cluster overlap. The standard deviation of the noise varied in range from $\mu = 0$, $\sigma = 0$ to $\mu = 0$, $\sigma = 15$, resulting in 16 experiments in which the outcome of the traditional FCM was compared with the ggc-FCM. For both FCM and ggc-FCM, the number of clusters (c) is set to 2 and the euclidian distance measure is used. In case of ggc-FCM, a 3x3 window contains the a priori spatial knowledge of spurious single pixels. The *OutlierThreshold* is set to $0.375 * 0.5 = 0.1875$, as discussed in section 2.3.6. The number of rejected and misclassified pixels are counted and the results are shown in table 2.2 and 2.3. Figures 2.1 and 2.2 show the corresponding segmented images.

The graph in figure 2.1 shows the partitioning of the measurement space with traditional FCM. The graph shows that the foreground cluster and the background cluster are identified easily. However, if the segmented image is considered, the foreground objects are contaminated with background pixels and vice versa. Due to the added noise, background pixels have shifted to the foreground cluster and foreground pixels have shifted to the background cluster. As the traditional FCM uses no information from the spatial domain, this result is to be expected. Table 2.2 summarizes the clustering results with standard FCM for 16 different noise levels. None of the pixels are rejected during standard FCM clustering. The # FALSE column indicates the number of misclassified pixels. The table shows that the number of misclassifications increases when the noise variance increases due to the increasing cluster overlap.

no.	noise variance	# foreground pixels	# reject	# FALSE	# background pixels	# reject	# FALSE
1	0	5000	0	0	4940	0	0
2	1	5000	0	0	4940	0	0
3	2	5000	0	0	4940	0	0
4	3	5000	0	0	4940	0	0
5	4	5000	0	0	4940	0	0
6	5	4999	0	1	4939	0	1
7	6	4993	0	7	4935	0	5
8	7	4972	0	28	4916	0	24
9	8	4934	0	66	4873	0	67
10	9	4879	0	121	4838	0	102
11	10	4794	0	206	4765	0	175
12	11	4704	0	296	4685	0	255
13	12	4628	0	372	4595	0	345
14	13	4555	0	445	4511	0	429
15	14	4458	0	542	4450	0	490
16	15	4377	0	623	4344	0	596

Table 2.2: *Clustering results for FCM of 16 measurements at different noise levels.*

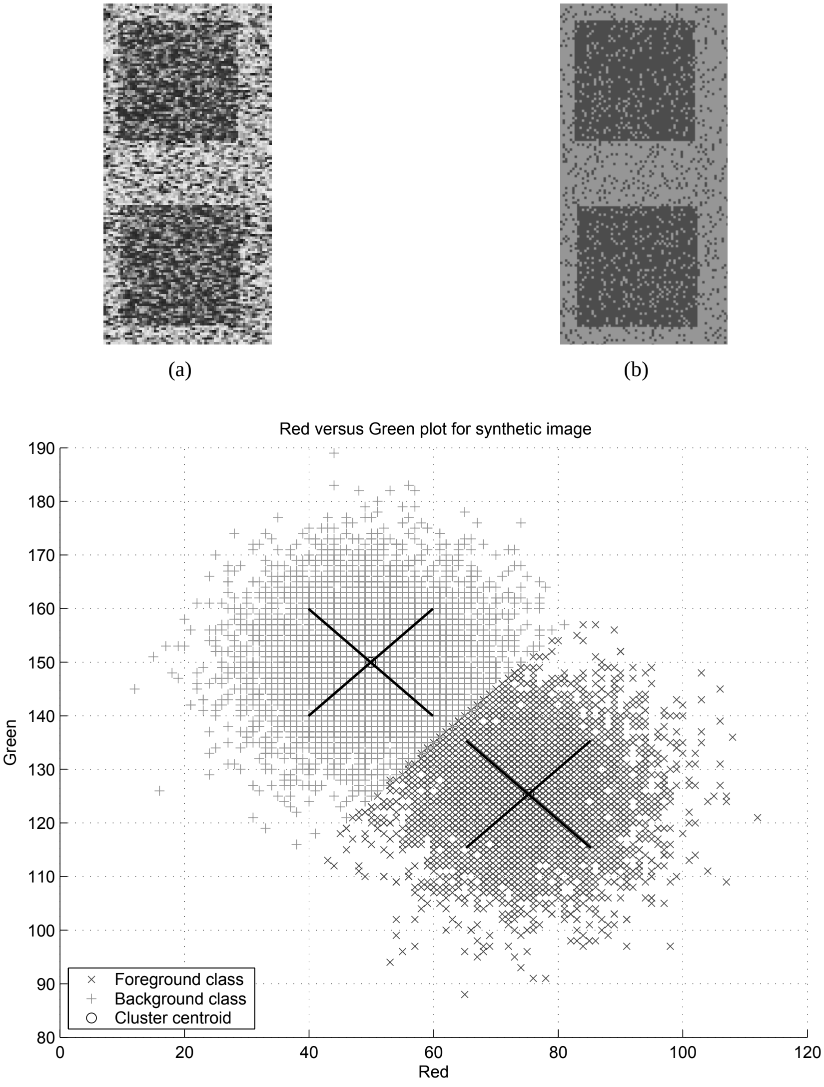

(a) (b)

(c)

Figure 2.1: *Results of traditional FCM. (a) Original image contaminated with Gaussian noise* $(\mu = 0, \sigma = 10)$*; (b) segmented image; (c) Red versus Green plot, the cross hair represents the center of a cluster.*

The results of the ggc-FCM conversely, show that some pixels are rejected (figure 2.2). Due to the noise, these pixels have distinct membership values compared to their spatial neighbors. The use of the condition in the clustering process results in the rejection of these isolated pixels. The condition of those pixels, which is based on the neighboring pixels in the spatial domain, is below the predefined *OutlierThreshold* value. As a result of this, the pixels are classified to the reject class in de defuzzification process. The rejected pixels appear as black pixels in the classified image of figure 2.2(a) and as small black diamonds in the plot of figure 2.2(b). The plot of figure 2.2(b) also shows that these rejected pixels are scattered in the measurement space. The segmented image in figure 2.2(a) shows that the rejected pixels are mostly isolated pixels. This demonstrates that the rejection of pixels in measurement space is solely determined by the geometrically based condition. Table 2.3 summarizes the clustering results with ggc-FCM for 16 different noise levels. Due to the increasing cluster overlap, the number of rejected pixels and the number of misclassifications increases when the noise variance increases. Comparing the results of traditional FCM in table 2.2 and the results of ggc-FCM in table 2.3 shows that clustering with ggc-

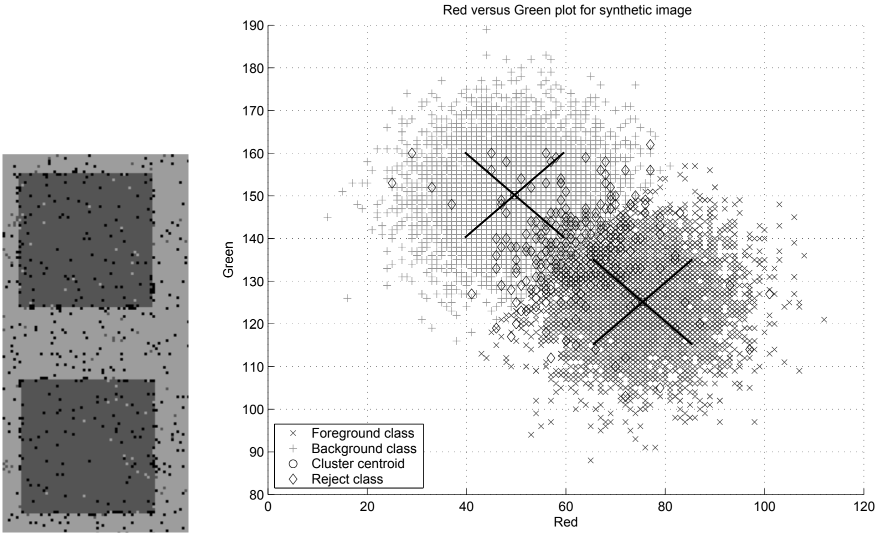

(a) (b)

Figure 2.2: *Results of ggc-FCM. (a) segmented image; (b) Red versus Green plot, the cross hair represents the centre of a cluster.*

FCM results in less misclassifications. Table 2.3 also shows that ggc-FCM rejects pixels even when no or little noise is added to the image. The number of rejected pixels matches with the number of foreground corners. The 4 corner pixels of the two squares are rejected. To prevent this, a higher *EdgeThreshold* value must be chosen. However, the consequence of a higher value of *EdgeThreshold* is that less misclassified pixels will be detected as they will not exceed the *EdgeThreshold*. In this particular case, the number of rejected corner pixels is far less than the the number of missed misclassified pixels would be.

no.	noise variance	# foreground pixels	# reject	# FALSE	# background pixels	# reject	# FALSE
1	0	4992	8	0	4940	0	0
2	1	4992	8	0	4940	0	0
3	2	4992	8	0	4940	0	0
4	3	4992	8	0	4940	0	0
5	4	4992	8	0	4940	0	0
6	5	4991	8	1	4939	0	1
7	6	4982	10	5	4933	5	2
8	7	4961	31	8	4914	16	10
9	8	4922	57	21	4860	61	19
10	9	4863	100	37	4829	74	37
11	10	4776	163	61	4751	144	45
12	11	4676	219	105	4668	196	76
13	12	4606	251	143	4565	244	131
14	13	4528	299	173	4488	267	185
15	14	4430	330	240	4425	333	182
16	15	4346	379	275	4318	357	265

Table 2.3: *Clustering results for ggc-FCM of 16 measurements at different noise levels.*

2.4.2 Experiment 1b: verification of OutlierThreshold value

Two additional experiments have been carried out to evaluate the selection procedure for the *OutlierThreshold* value. In both experiments,the synthetic image as described in section 2.4.1 is used, only this time the noise variance is constant ($\mu = 0,\ \sigma = 10$). The size of window W is 3x3. The number of clusters (c) is set to 2 and the euclidian distance measure is used. The number of rejected and misclassified pixels were counted, for both the foreground class and the background class.

In the first experiment,the value of the *OutlierThreshold* is varied between 0.05 - 0,95 to evaluate the effect of the *OutlierThreshold* on the number of rejected and misclassified pixels. Figure 2.3 shows the number of rejected and misclassified pixels of the foreground class. The graph shows that an increment of the *OutlierThreshold* value is accompanied with an decrement of the number of misclassified pixels and an increment of the number of rejected pixels. The optimal threshold is there where

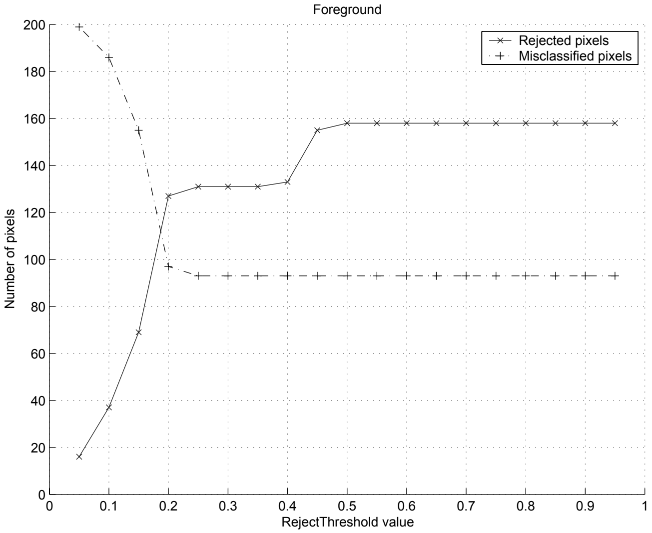

Figure 2.3: *Number of rejected and misclassified pixels for the foreground class for different values of* OutlierThreshold.

the number of misclassified pixels no longer decreases and the number of rejected pixels no longer increases. The graph shows that this holds for threshold values in a range of 0.19 - 0.38. The start value of the range corresponds with the predefined optimal threshold for *OutlierThreshold* ($0.375 * 0.5 = 0.1875$) and the upper value corresponds with the value of Δm* u_{rc}, where u_{rc}=1. As discussed in section 2.3.6, these pixels are not outliers. In figure 2.4, the mean membership deviation (Δm), the membership value of the centroid (u_{rc}) and the calculated condition (f_{rc}) are shown for all pixels with a $\Delta m >$*EdgeThreshold*. The data are sorted on the u_{rc} variable. The graph shows three different area's. Area A shows spatial outliers which must be rejected: high values of Δm and low values of u_{rc}. The pixels in area C have low values of Δm and high of u_{rc}. These pixels are not outliers and should not be rejected, the Δm value of these pixels is just above the *EdgeThreshold* due to to the added noise. In area B, u_{rc} increases rapidly to higher values and the height of the step in the f_{rc} -line coincides with the range of threshold values as mentioned in the paragraph above. To verify that the optimal *OutlierThreshold* is not within the complete range of threshold values but actually a single point, both experiments have been repeated for different noise levels ($\sigma = 5, 8, 12, 15$), different kernel sizes (3,5,7), different number of classes (2,3,4). All experiments showed that the *OutlierThreshold* value,

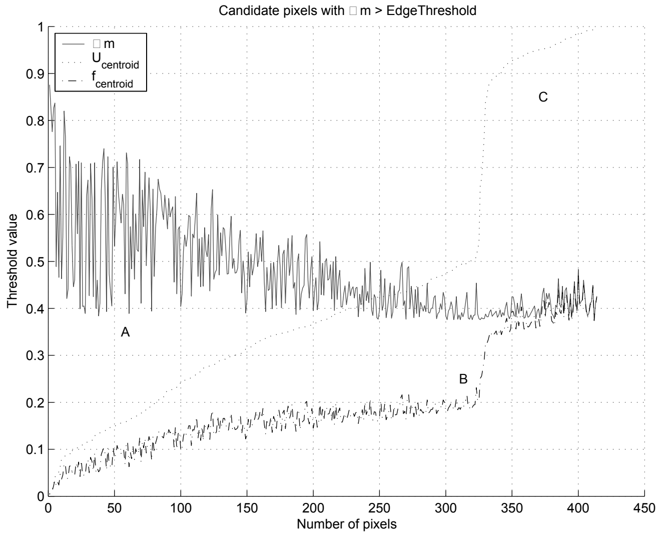

Figure 2.4: *Values of* Δm*,* u_{rc} *and* f_{rc} *for all pixels of synthetic image with* Δm *above* Edge-Threshold *value.*

when selected according to equation 2.12, gives the best results. Higher values for the *OutlierThreshold* only increase the number of rejected pixels.

2.4.3 Experiment 2: Removal of objects in a potato image

In recent potato inspection and sorting, humans are more and more replaced by camera's and computers. To reduce costs, the color images need to be captured with standard low-budget RGB cameras. The images are digitized by a framegrabber and processed by a computer [5]. The computer segments the potato image into several homogeneous regions (classes) and the number of pixels in each class are counted. Based on the number of pixels within a class and a predefined threshold value, the computer accepts or rejects the potato. The 3-CCD camera delivers three different gray-value images (576x768 pixels), which are combined to a single 24 bit RGB image. A prism and three color filters map the incoming light to the three CCD sensors. The quality of the images is low due to the high speed of image grabbing, which makes the images noisy and blurred. Furthermore, the spectral resolution is low due to the limited bandwidth of the three coinciding color filters. The use of multispectral cameras's with higher spectral resolution for potato inspection is not possible yet due the combination of high inspection speed and light insensitivity of these camera's. A consequence of the noisy and limited spectral information of these images is that certain, almost similar colored potato defects are hard to discriminate. This has a negative effect in case of potato sorting as described above. Incorrect segmentation may result in a false rejection of the potato. Additional spatial information is required to discriminate between different defects with similar color. An example of similar colored objects is given in figure 2.5(a). The figure shows a Nicola-potato image (233x134 pixels). The potato contains spots of different size and origin. The large dark spots are the result of a potato disease and the smaller dark spots are typical skin spots for this particular potato cultivar. During segmentation, the skin spots should be ignored because these pixels are wrongfully classified as disease pixels. The sub-image, indicated with the black rectangle, shows the larger disease spot (top left part of the rectangle) and the small skin spots in detail. Without spatial information, one cannot discriminate between the good skin spots and the disease spot, as they have similar spectral properties. Discrimination between the larger disease spots and the smaller skin spots is only possible if a priori knowledge of spot size is used during clustering. In this experiment, the results of clustering with traditional FCM are compared with the results of clustering with ggc-FCM, where ggc-FCM uses a 5x5-neighborhood window to add the spatial a priori knowledge about the skin spot size. In both experiments, the number of clusters is set to 2 and the euclidian distance measure is used. The results of traditional FCM clustering are shown in figure 2.5. As expected, the similar colored small spots are all classified into the disease class. Applying ggc-FCM to the potato image gives the results as shown in figure 2.6. With the 5x5 kernel, small objects receive such a low condition value (<*OutlierThreshold*) that these objects are rejected in the defuzzyfication procedure. The rejected pixels appear as black colored pixels in the segmented image of figure 2.6(b). The graph of figure 2.6(c) shows that most of the rejected pixels are scattered over the disease cluster. This indicates that mainly disease pixels are rejected and that the majority of skin pixels are classified correctly. The rejected skin pixels are not included in the disease class and therefore do not influence the segmentation results negatively. The experiment shows that the use of a priori spatial information of spot size during clustering makes it possible to discriminate between objects with similar spectra. The blob located just above the middle of the image is classified as disease because the area of the blob is larger than the area covered by the 5x5 window. An increased window size will remove this blob.

2.5 Conclusions and further research

In this paper, a technique to guide FCM clustering based on geometrical information is presented. The use of ggc-FCM clustering as a multivariate image segmentation

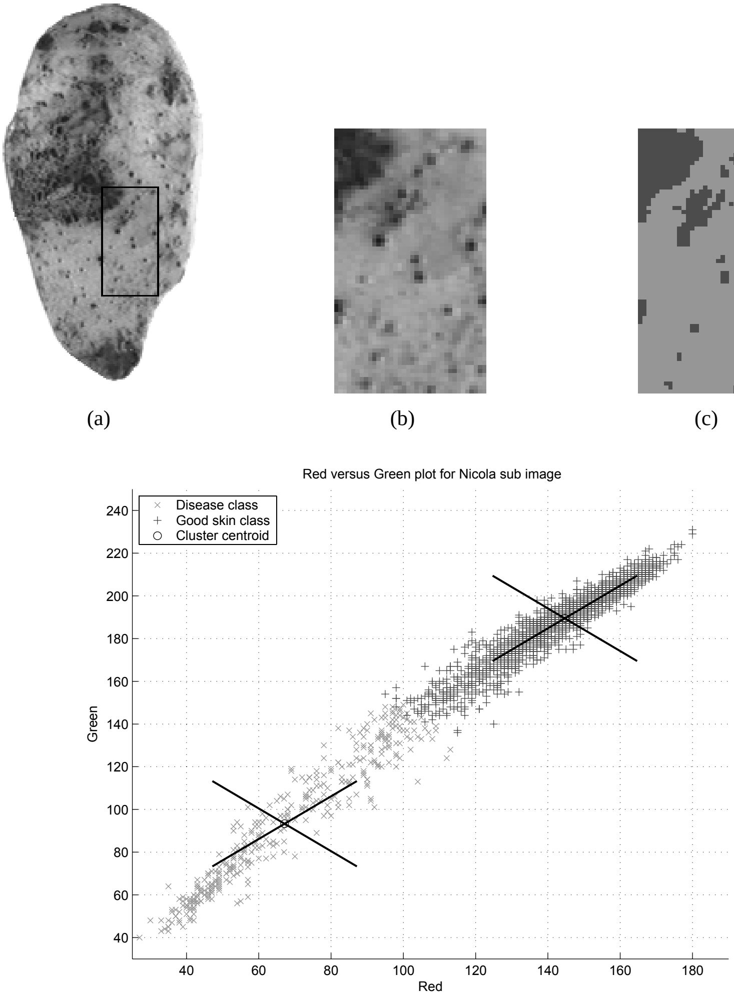

(a) (b) (c)

(d)

Figure 2.5: *Results of traditional FCM. (a) Original potato image; (b) potato sub image; (c) segmented sub image; (d) Red versus Green plot, the cross represents the center of a cluster.*

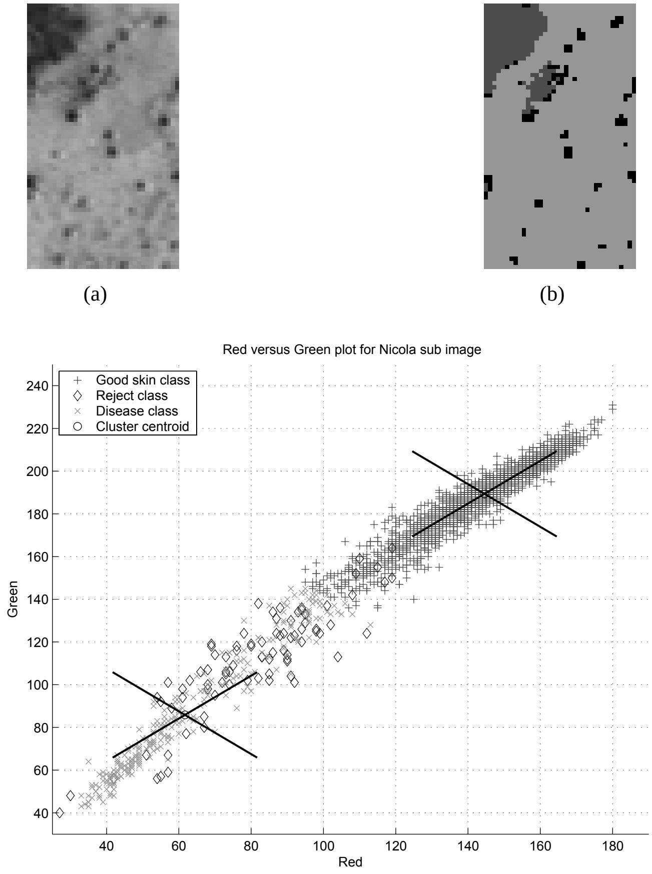

(a) (b)

(c)

Figure 2.6: *Results of ggc-FCM. (a) Original sub image; (b) segmented sub image; (c) Red versus Green plot, the cross represents the center of a cluster.*

process clearly shows improvements above clustering with traditional FCM. The addition of a priori information from the spatial domain makes it possible to intervene in the clustering process and guide the clustering. A window of variable size is sufficient to store a priori spatial information about spurious pixels or small objects. An outlier threshold value determines which pixels are removed in the defuzzification procedure, where at the same time edge pixels are preserved. The optimal value for this threshold can be determined. As a result, no additional parameters settings are required for ggc-FCM compared to traditional FCM. Future research will include the incorporation of more geometrically based conditions. Conditions that are especially designed to search for a specific shape in the spatial domain can be used to replace a traditional sequence of segmentation and shape detection with a single FCM-clustering procedure.

2.6 Acknowledgements

The authors wish to thank Professor L.M.C. Buydens and the reviewers for their useful comments and contributions to the paper.

Bibliography

[1] J. R. Mansfield, M. G. Sowa, G. B. Scarth, R. L. Somorjai, and H. H. Mantsch, "Analysis of spectrosopic imaging data by Fuzzy C-Means clustering," *Analytical Chemistry*, vol. 69, pp. 3370–3374, 1997.

[2] L. Hall, A. M. Bensaid, L. Clarke, R. P. Velthuizen, M. S. Silbiger, and J. Bezdek, "A comparison of neural network and fuzzy clustering techniques in segmenting magnetic resonance images of the brain," *IEEE Transactions on Neural Networks*, vol. 3, no. 5, pp. 672–682, 1992.

[3] J. Bezdek, L. Hall, and L. Clarke, "Review of mr image segmentation techniques using pattern recognition," *Medical Physics*, vol. 20, no. 4, 1993.

[4] J. Bezdek, *Pattern Recognition with Fuzzy Objective Functions*. New York: Plenum Press, 1981.

[5] J. Noordam, G. Otten, A. Timmermans, and B. van Zwol, "High-speed potato grading and quality inspection based on a color vision system," in *SPIE, Machine Vision and Its Applications* (K. W. Tobin, ed.), vol. 3966, (San Jose, Californie), pp. 206–220, SPIE, 2000.

[6] H. Frigui and R. Krishnapuram, “A comparison of fuzzy shell clustering methods for the detection of ellipses,” *IEEE Transactions on Fuzzy Systems*, vol. 4, no. 2, pp. 193–200, 1996.

[7] A. Ouahab Boudraa, “Automated detection of the left ventricular region in magnetic resonance images by Fuzzy C-Means model,” *International Journal of Cardiac Imaging*, vol. 13, pp. 347–355, 1997.

[8] M. R. Rezaee, *Application of fuzzy techniques in image segmentation*. PhD thesis, University of Leiden, 1998.

[9] S. H. Park, I. D. Yun, and S. U. Lee, “Color image segmentation based on 3D clustering: Morphological approach,” *Pattern Recognition*, vol. 21, no. 8, pp. 1061–1076, 1998.

[10] T. Næs and B. Mevik, “The flexibility of fuzzy clustering illustrated by examples,” *Journal of Chemometrics*, vol. 13, pp. 435–444, 1999.

[11] A. M. Bensaid, *Improved fuzzy clustering for pattern recognition with applications to image segmentation*. PhD thesis, South Florida, 1994.

[12] W. Pedrycz, “Conditional Fuzzy C-Means,” *Pattern Recognition Letters*, vol. 17, pp. 625–631, 1996.

[13] P. Geladi and H. Grahn, *Multivariate Image Analysis*. John Wiley & Sons Ltd., 1996.

2.7 Appendix

The combination of the update formulas for the membership values, cluster centroids and condition lead to the following pseudo code for the ggc-FCM:

```
Initialization:
Choose c, the number of centroids.
Provide random initial values for center matrix $\mathbf{V}$,
Calculate the kernel dependent $EdgeThreshold$ value :

    $EdgeThreshold = \frac{floor(\frac{s}{2})s}{s^2 - 1}$

Start of iteration loop
1 compute membership values :

    $u_{ik} = \frac{f_k}{\sum_{j=1}^{c} \left( \frac{d_{ik}}{d_{ij}} \right)^{\frac{2}{m-1}}}$

2 Compute new centroids

    $\mathbf{v}_i = \frac{\sum_{k=1}^{n} u_{ik}^{m} \mathbf{x}_k}{\sum_{k=1}^{n} u_{ik}^{m}}$

3 Determine the majority class iMax of neighboring pixels:

    $iMax = i \mid \max_{i}(\mathbf{sum\_u_{rc}})$

4 Calculate mean membership deviation $\Delta m_{rc,imax}$ :

    $\Delta m_{rc,imax} = \frac{1}{s^2 - 1} \sum_{r'c' \varepsilon W} \left| u_{rc,imax} - u_{r'c',imax} \right|$

if $\Delta m_{rc,imax} > EdgeThreshold$:

    $f_{rc} = \Delta m_{rc,imax} \, u_{rc,imax}$

5 Check for convergence :
If convergence goto 1, else stop
```

```
End of iteration loop.
6 Defuzzify partition matrix U :
if $f_{rc} < OutlierThreshold$: add pixel to reject class
else perform procedure of Maximum Membership
```

Chapter 3

Unsupervised segmentation of predefined shapes in multivariate images

Abstract

Fuzzy C-means (FCM) is an unsupervised clustering technique and is often used for the unsupervised segmentation of multivariate images. In traditional FCM the clustering is based on spectral information only and geometrical relationship between neighboring pixels is not used in the clustering procedure. In this paper, the Spatially Guided FCM (sg-FCM) algorithm is presented which segments multivariate images by incorporating both spatial and spectral information. Spatial information is described by a geometrical shape description and can vary from a local neighborhood to a more extended shape model such as the hough circle detection. A modified FCM objective function uses the spatial information as described by the shape model. This results in a segmented image in which the construction of the cluster prototypes is influenced by spatial information. The performance of Spatially Guided FCM is compared with both FCM and the sequence of FCM and a majority filter. The sg-FCM segmented image shows more homogeneous regions and less spurious pixels.

3.1 Introduction

The use of the unsupervised Fuzzy C-Means (FCM) clustering [1] to segment a multivariate image in meaningful regions has been a research topic for many decades [2, 3, 4, 5, 6, 7]. The main reason for the popularity of FCM as an image segmentation technique is its transparency and unsupervised nature. FCM is especially applied as segmentation technique in cases where only few multivariate images with no a priori (e.g. spectral) information are available and no training set can be extracted from these multivariate images to train a supervised classifier [8, 4]. Such images are produced by Magnetic Resonance Imaging (MRI) devices and multispectral cameras in fruit and vegetable inspection. Multispectral images reveal information about the spectral properties of the product constituents. This offers possibilities to discriminate between similar 'colored' defects and to detect latent defects and diseases. The detection of these latent defects and diseases is of great importance as they affect the long-term quality of the product.

Known drawbacks of FCM such as the required parameter for the number of clusters, its sensitivity for initialization and its sensitivity of clusters with different number of objects have not led to any obstruction given the number of widespread applications [5, 8]. However, a known disadvantage of applying FCM as a multivariate image segmentation technique is that the information from the spatial domain is ignored. Only the spectral information determines the partitioning of the measurement space. Although multivariate imaging offers possibilities to differentiate between both objects of similar spectra and different spatial correlations, FCM can not utilize this property. It is clear that only the extra spatial information can discriminate between different objects with overlapping clusters in the spectral domain. Furthermore, if no a priori information about the spectra is available, information about the shape of the objects in the image is sometimes known. However, traditional FCM cannot use this a priori spatial information during the clustering process.

This has been recognized by several authors and a number of FCM based applications have been reported where spatial information is combined with spectral information to improve segmentation results. The majority of applications use a sequence of both spectrally and spatially based segmentation operations [6, 9, 10]. In these applications, the FCM segmented image is followed by a spatially based filter which tries to correct the segmentation errors. Although in some cases good results are obtained, the spatially based filter can solely correct segmentation errors $afterwards$ en never intervene during the spectrally based clustering. As a result, not all segmentation errors can be corrected by this approach. Therefore, several other ideas have been presented in literature which all try to use spatial information during the clustering process by modifying the objective function of FCM [7, 11, 12, 13, 14, 15]. In some modifications the idea is to use FCM as an image compression tool and therefore the focus of the algorithm is on keeping the original image characteristics and remove the unimportant details [11, 12]. This is an undesirable effect in food inspection as small details may indicate initial formation of diseases.

In a variant of the standard k-means (a crisp version of FCM), called the contig *k*-means [13, 15], both spectral and spatial information are combined in a new cost function that is minimized iteratively. This cost function is a weighted sum of the compactness of the clusters and the contiguity of pixels in spatial domain. The algorithm requires that the user specifies a parameter λ to define the relative importance of these two properties.

Another technique is a combined classifier approach in which the results of a spatial classifier and a spectral classifier are combined [14]. The algorithm starts with an initial labelling performed by an unsupervised clustering method in the spectral domain. The segmentation is then performed iteratively for both spatial and spectral domain. At the end of each iteration, results of both spectral and spatial classifier are combined. The segmentation performance gradually improves over the iterations until a stable state is reached. As both classifiers are combined convergence of the algorithm can be a burden and is not guaranteed.

The Geometrically Guided Conditional FCM (ggc-FCM) [7] is able to include a priori locally spatial information to classify spurious pixels or small sized blobs into a reject class. However, in applications such as product inspection where each pixel must be assigned to a true product class, the use of a reject class is impractical.

The advantage of Spatially Guided FCM (sg-FCM) presented in this paper is that it overcomes the reject class and is developed to segment multivariate images by incorporating both spatial and spectral information. The algorithm uses a modified objective function that allows a priori spatial information to guide the clustering process and requires no parameters as in the contig *k*-means approach. New aspects are that various shaped objects can be detected during clustering by using an analytical shape description. This makes it possible to search for a specific shape during clustering. These are the main differences and advantages of the sg-FCM algorithm compared to the traditional FCM algorithm and the aforementioned algorithms.

The paper is organized as follows: Section 3.2 discusses the principle of sg-FCM, the theory FCM and the modified objective function for sg-FCM. In section 3.3 the theory of sg-FCM to detect objects of different shape and size based on a geometrical model is discussed. Section 3.4 shows the results of clustering multivariate images with sg-FCM and FCM. In the last section, the conclusions are given.

3.2 Spatially Guided Fuzzy C-Means clustering

3.2.1 Principle of sg-FCM

In case of clustering multivariate images with the traditional FCM algorithm, the spatial information is not used during clustering. The construction of cluster prototypes is solely based on the spectral information. The rationale of sg-FCM is to include spatial information, described by a geometrical shape description, during the construction of the cluster prototypes. This means that both the spectral and spatial neighborhood of a pixel determine the contribution of a pixel to a cluster prototype. In theory, any arbitrary shape can be detected during clustering provided that there is a geometrical shape description (geometrical model) available. A geometrical model can vary from a simple local neighborhood model to describe outliers or small blobs, to a more complex model to detect any predefined shape. Figure 3.1 shows the principle of sg-FCM. During each FCM iteration, pixels or groups of pixels in the segmented image are compared with the predefined geometrical model. The difference between the geometrical model and the pixels in the segmented image described by the geometrical model result in a value for an additional mismatch variable. A high value for this variable indicates a mismatch between the geometrical model and pixels described by the model in segmented image, a low value indicates a math between the model and pixels in the segmented image. This mismatch variable has been used by a modified FCM where the construction of cluster prototypes is influenced by the value of this variable. This results in a segmented image in which the construction of the cluster prototypes is influenced by spatial information, reflected by the geometrical model. The principle of FCM and the modified FCM are described in the following sections.

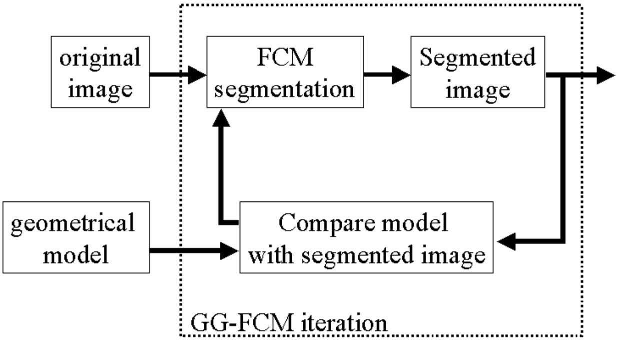

Figure 3.1: *The principle of sg-FCM.*

3.2.2 Fuzzy C-Means Clustering (FCM)

Given a set of n data objects, $X = \mathbf{x}_1, ..., \mathbf{x}_n$, the FCM algorithm minimizes the weighted within group sum of squared error objective function $J(U, \mathbf{V})$ [1]:

$$J(U,\mathbf{V}) = \sum_{k=1}^{n}\sum_{i=1}^{c} u_{ik}^{m} d^2(\mathbf{x}_k, \mathbf{v}_i) \tag{3.1}$$

where $\mathbf{x}_k$ is the k-th p-dimensional data vector, $\mathbf{v}_i$ is the prototype of the center of cluster i, u_{ik} is the degree of membership of $\mathbf{x}_k$ in the i-th cluster, m is a weighting exponent on each fuzzy membership ($m > 1$), $d(\mathbf{x}_k, \mathbf{v}_i)$ is a distance measure between object $\mathbf{x}_k$ and cluster prototype $\mathbf{v}_i$, n is the number of objects and c is the number of clusters. A solution of the objective function $J(U, \mathbf{V})$ can be obtained via an iterative process where the degrees of membership u_{ik} and the cluster prototypes $\mathbf{v}_i$ are updated via:

$$u_{ik} = \frac{1}{\sum_{j=1}^{c}\left(\frac{d_{ik}}{d_{jk}}\right)^{\frac{2}{m-1}}} \tag{3.2}$$

with c the number of clusters, d_{ik} the distance between object k and cluster i, d_{jk} the distance between object k and cluster j,

$$\mathbf{v}_i = \frac{\sum_{k=1}^{n} u_{ik}^{m} \mathbf{x}_k}{\sum_{k=1}^{n} u_{ik}^{m}} \tag{3.3}$$

with the constraints:

$$u_{ik} \in [0,1], \qquad \sum_{i=1}^{c} u_{ik} = 1 \quad \forall k, \qquad 0 < \sum_{k=1}^{n} u_{ik} < N \quad \forall i \tag{3.4}$$

A detailed description of FCM is described in literature [1].

3.2.3 Fuzzy C-Means with auxiliary variable

As stated in section 3.2.1, sg-FCM is based on a modified version of FCM [16] to incorporate a priori spatial information in the clustering process. This modified version of FCM uses an auxiliary variable to add a priori information (spectral or spatial) to influence the clustering. Usually, clustering is considered as an unsupervised routine where no information about the underlying spectral structure of the objects is known. However, in cases where clustering is used and a priori information is known about some objects, it might be advantageous to use this a priori information to influence the clustering process. This type of clustering can be considered as an intermediate mode between supervised and unsupervised clustering where supervised data (a priori information) is combined with unsupervised data. In literature [16], this idea is implemented for FCM and has resulted in a modified objective function for FCM:

$$J(U,\mathbf{V}) = \sum_{k=1}^{n}\sum_{i=1}^{c} u_{ik}^{m} d^{2}(\mathbf{x}_k,\mathbf{v}_i) + \alpha \sum_{k=1}^{n}\sum_{i=1}^{c}(u_{ik} - f_{ik}b_k)^{m} d^{2}(\mathbf{x}_k,\mathbf{v}_i) \tag{3.5}$$

The first term of equation 3.5 is the standard objective function for FCM, as described in section 3.2.2. The boolean variable b_k in the second term indicates if a priori information about object k is known and the variable f_{ik} encapsulates the a priori information for object k about cluster i. The parameter α is a scaling factor to maintain a balance between the supervised and unsupervised data and is proportional to the ratio supervised/unsupervised data [16]. If no a priori information is available, the boolean variable in second term is set to zero and the objective function returns to the standard objective function for FCM, with an extra scaling factor $(1+\alpha)$ (the extra scaling factor $(1+\alpha)$ has no impact on the clustering results and can be ignored). The introduction of an auxiliary variable leads to a new update procedure for the membership value u_{ik} and the cluster prototype $\mathbf{v}_i$ is (m=2):

$$u_{ik} = \frac{1}{1+\alpha}\left\{\frac{1+\alpha\,(1-b_k\sum_{l=1}^{c} f_{lk})}{\sum_{l=1}^{c}\frac{d_{ik}^{2}}{d_{lk}^{2}}} + \alpha\, f_{ik}b_k\right\}, \qquad \mathbf{v}_i = \frac{\sum_{k=1}^{n} u_{ik}^{2}\mathbf{x}_k}{\sum_{k=1}^{n} u_{ik}^{2}} \tag{3.6}$$

High values of f_{ik} will enhance the membership of object k for cluster i and low values of f_{ik} will weaken the membership for cluster i. Analogously, by assigning $b_k = 0$ in equation 3.6 in case of no a priori information, the update formula for the partition matrix returns to the standard equation for FCM. As described in section 3.2.1, the value of f_{ik} is determined by the difference between a geometrical shape model and the segmented image. The geometrical model contains the a priori shape information which is used to influence the clustering via the variable f_{ik}. In order to update the value for f_{ik} during the clustering, a modification is required which will be described in the next section.

3.2.4 Modifications for Spatially Guided FCM (sg-FCM)

In literature [16], it is assumed that a priori information never changes during the clustering process. This means that the value of the parameters b_k and f_{ik} in equation 3.6 are manually set beforehand and remain fixed during the clustering process. For the method presented in this paper, the values of b_k and f_{ik} are not fixed and can change during the clustering process since it is not known before the clustering starts which objects (pixels) are described by the geometrical model. As the algorithm gradually iterates, a value of f_{ik} is set for those objects that are described by the geometrical model. As stated in the previous section, the boolean variable b_k is set to 1 if a priori information for object k is available. If this is not the case, the boolean variable b_k is set to zero and the update equation (3.6) reduces to the standard update equation for FCM. However, the same result can be obtained when f_{ik} is set to zero for all clusters and equation 3.6 returns also to the standard update equation for FCM (in both situations, the scaling factor α remains). Now, instead of using two variables b_k and f_{ik}, a single variable f_{ik} is sufficient to guide the clustering. For the algorithm presented in this paper the boolean variable b_k is set to 1 for all objects and the variable f_{ik} is used to guide the clustering process. With $b = 1$ for all objects, equation 3.6 simplifies to:

$$u_{ik} = \frac{1}{1+\alpha}\left\{\frac{1+\alpha\left(1-\sum_{l=1}^{c} f_{lk}\right)}{\sum_{l=1}^{c}\frac{d_{ik}^2}{d_{lk}^2}} + \alpha f_{ik}\right\} \tag{3.7}$$

When no a priori information is present, f_{ik} is set to zero and the standard membership update formula of equation 3.2 is used. However, if a priori information about some objects is available, the modified membership update formula of equation 3.7 is used instead. In the following section, two different geometrical shape models that determine the value for f_{ik} are considered. First, a local neighborhood window is used to describe outlier pixels and small blobs. Section 3.3.2 describes a more complicated model to detect circles with different diameters.

3.3 Spatial shape models

3.3.1 Local Neighborhood

For the detection of outlier pixels and small blobs, membership values of surrounding neighboring pixels determine the value of variable f_{ik} for each pixel. The value of f_{ik} is an implicit measure of similarity for a pixel compared to surrounding neighbors. The value of f_{ik} varies between 0 and 1, depending on the similarity between neighboring pixels. If surrounding pixels have the same membership values $f_{ik} = 0$ whereas $f_{ik} = 1$ if surrounding pixels have deviate membership values. As a result, membership values of spurious pixels in the spatial domain can be influenced indirectly when their neighbors have different membership values. The membership values in the partition image determine the value of f_{ik}. A partition image is a folded column of the partition matrix **U**: the number of rows in the partition matrix **U** is equal to the number of rows (nr) times the number of columns (nc) of the original

image. This makes that each column in the partition matrix can be arranged to an image with same spatial dimensions as the original multivariate image. Such a rearranged column is called a partition image [7].
The matrix index k, which corresponds with object k in the partition matrix **U** and data matrix **X**, also corresponds with a position (row, col) in the partition image. A pixel at position (row, col) in the partition image corresponds to position $k = row \times nc + col$ in both the matrices **U** and **X**. Figure 3.2 shows the relationship between a pixel at position (row, col) in a partition image and the same position in the partition matrix **U**. To determine for which cluster the current pixel must be enhanced, the majority class (i_{max}) of the neighborhood is determined. To calculate i_{max}, the membership values covered by the neighborhood window are added for each cluster i. The cluster with the highest sum is considered as the i_{max} cluster. This is the cluster the center pixel of the window presumably belongs to. For this particular center pixel, the average membership deviation $(\Delta m_{i_{max}k})$ of the center pixel compared to the memberships of neighboring pixels is determined:

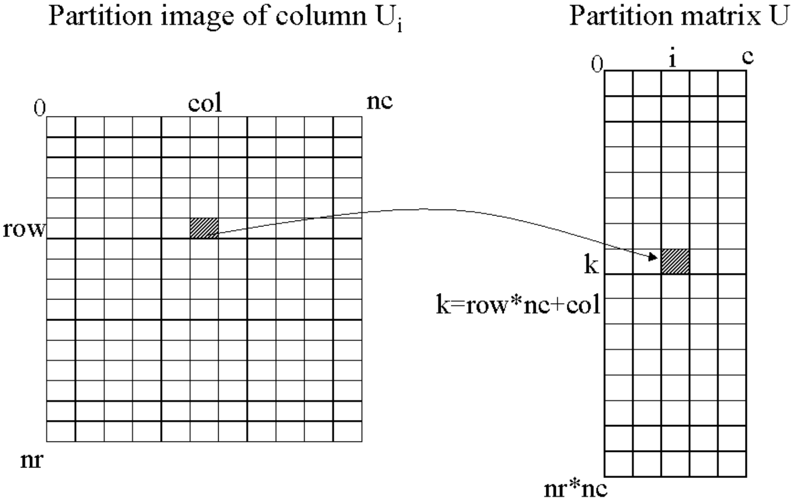

Figure 3.2: *The relationship between pixels in the partition image and partition matrix.*

$$\Delta m_{i_{max}k} = \frac{1}{s^2 - 1} \sum_{(k' \in W)} \left| u_{i_{max}k'} - u_{i_{max}k} \right| \tag{3.8}$$

where $\Delta m_{i_{max}k}$ is the average membership deviation for the pixel at position k of partition image i_{max}, W is a neighborhood window with (odd) size s, $u_{i_{max}k'}$ is the degree of membership of the neighbor pixel at position $k^{'}$ in the window W of partition image i_{max} and $u_{i_{max}k}$ is the degree of membership of the center pixel in the window of partition image i_{max}. For the subsequent iteration $(t+1)$ the variable $f_{i_{max}k}$ is updated with the average membership deviation $\Delta m_{i_{max}k}$ of current iteration (t):

$$f_{i_{max}k}(t+1) = f_{i_{max}k}(t) + \Delta m_{i_{max}k}(t) \tag{3.9}$$

For the clusters $i \neq i_{max}$, the value of f_{ik} is weakened with Δm_{ik}:

$$f_{ik}(t+1) = f_{ik}(t) - \Delta m_{ik}(t) \tag{3.10}$$

where the value of f_{ik} is bound between 0 and 1. For a homogeneous region the average membership deviation Δm will be zero and no spatial guidance of pixel k occurs via the variable f_{ik}. After each iteration step, the error between iteration t and the previous iteration $t-1$ is calculated :

$$E_t = \|U_t - U_{t-1}\| \tag{3.11}$$

If error E_t is below a predefined value of the stop criterion ε, a new iteration step of the sg-FCM begins with the updated f_{ik} for each pixel k. The value for ε is set beforehand and determines when the sg-FCM is stopped, identical as with FCM. The conditioning procedure as described above does not start before the error E_t is below a small value (δ) to prevent that the sg-FCM gets trapped in a local minimum.

3.3.2 Circle detection with sg-FCM

As stated in section 3.2.1, the sg-FCM algorithm can detect and emphasize objects of arbitrary shape during clustering. In this section, a model to detect solid circles of unknown radius is described. A Hough transform [17, 18, 19] is implemented for the circle detection procedure which searches for circular shaped objects in the segmented image. The Hough transform method of shape analysis uses a constraint equation relating points in image space, usually edge points, to possible parameter values of the searched shape. The Hough transform is a general shape detection technique which is capable to detect any shape which has been parameterized. To determine possible circle candidate pixels in the sg-FCM segmented image, an edge detection procedure is performed on the segmented image. These edge points serve as starting points for the Hough transform. Once a circle has been detected, the majority class (i_{max}) of the points within the circle is determined. Those pixels that are not classified to the i_{max} class are enhanced for the i_{max} class by increasing the value of f_{ik} with the membership deviation ($\Delta m_{i_{max}k}$). This enhancing and weakening is similar as in the local neighborhood approach as described in the previous section. Pixels outside the detected circles remain unconditioned.

3.4 Experiments

To show the performance of sg-FCM, experiments have been carried out on synthetic and real world multivariate images. The sg-FCM algorithm is compared with both traditional FCM and the sequence of traditional FCM followed by a majority filter (FCM-MAJORITY). A majority filter is a spatial neighborhood filter that changes the class of the center pixel within an odd window W to the majority class of all the pixels in window W. The sequence of a spectral based segmentation such as FCM and a majority filter is known as a combination which gives good and satisfying results and is therefore interesting to compare with. Random numbers are used for the initialization of the cluster centroids in each experiment. After the clustering procedure, the fuzzy images are converted to crisp images by applying the maximum membership procedure. This means that an object is classified to the cluster with highest membership.

3.4.1 Instrumentation

The real world potato and peppers image of experiments 2 and 3 are captured by a color camera. For the potato image, a Sony 3-CCD color camera was used. A prism in the camera splits the incoming light of the visible spectrum into a Red, Green and Blue part and the light is mapped on the corresponding CCD. A framegrabber in the computer digitizes the 3 images and delivers 3 different 8-bit gray-value images, which result in a multivariate color image with 3 variables (Red,Green and Blue). The values for the three variables Red, Green and Blue in the synthetic color images are created manually by pixel manipulation.

The multispectral candy image of experiment 4 is recorded with an ImSpector V7 imaging spectrograph (Spectral Imaging Ltd. Oulu, Finland) mounted on a Peltier cooled Qimaging PMI-1400EC monochrome camera. The ImSpector V7 produces a multispectral image where the 396-736 nm part of the electromagnetic spectrum is recorded in 257 small bands (every 1.3 nm) for every pixel. The incoming light is split by a prism-grating-prism and projected on the 2 dimensional CCD in the camera. One dimension of the CCD records the line pixels (spatial axis) and the other dimension contains the spectral information (spectral axis) of each pixel. A 2-dimensional spectral image is obtained by moving the object under the ImSpector during recording. The translation table used to move the object with respect to the camera is a Lineartechniek Lt1-SP5-C8-600 translation table driven by a SDHWA 120 programable microstepping motor driver (Ever Elettronica, Italy). The stepsize of the translation table was chosen to match the spatial resolution of the spatial axis. The used lighting setup consists of two Dolan-Jenner PL900 illuminators (Andover St. Lawrence, Mass.) with 150 W quartz halogen lamps. The scene was illuminated by two glass fiber optic line arrays (Vision Light Tech) of 0.002 inch × 6 inch aperture. Two cylinder lenses (Dolan Jenner) were positioned in front of the line arrays. Detailed information about the used multispectral imaging setup and the spatial and spectral calibration procedure is described in literature [20].

3.4.2 Experiment 1: Segmentation of a synthetic image

The synthetic image experiment demonstrates the principle of the spatially guided clustering and shows the effect of different noise levels on the clustering. The artificial image (140x70 pixels) consists of two squares of same colour (R=150,G=50,B=50) on a different background colour (R=125,G=75,B=50). To verify that the outcome of the clustering results is not influenced by unequal cluster sizes, which is a known pitfall of FCM, the amount of foreground pixels (5000) is in balance with the amount of background pixels (4940). The image is contaminated with gaussian noise to simulate cluster overlap. The standard deviation was fixed for different RGB values and varied in range from $\mu = 0$, $\sigma = 0$ to $\mu = 0$, $\sigma = 20$, resulting in 21 experiments in which the outcome of the sg-FCM was compared with both the traditional FCM and the sequence of traditional FCM + majority filter (FCM-MAJORITY). For both FCM and sg-FCM, the number of clusters (c) is set to 2, m=2, $\varepsilon = 0.0001$ and the euclidian distance measure is used. In case of sg-FCM and FCM-MAJORITY, a 3×3 window serves a simple geometrical model and contains the a priori spatial knowledge of spurious single pixels. The experiment is repeated for 10 times with random initialization values for the cluster centroids and after each experiment the number of misclassified pixels is counted. The results are averaged and depicted in figure 3.5.

Figure 3.4(a) shows the graph of the Red versus Green variable of the original image contaminated with gaussian noise ($\mu = 0$,$\sigma = 10$). The cluster overlap between the foreground and background pixels, which is due to the gaussian noise, is clearly visible. The FCM segmented image in figure 3.3(b) shows that foreground objects are contaminated with background pixels and vice versa. Owing to the added noise, background pixels have shifted to the foreground cluster and foreground pixels have shifted to the background cluster. As traditional FCM uses only spectral information and no information from the spatial domain, this result is to be expected. The graph of the Red versus Green variable in figure 3.4(b) shows the FCM partitioned measurement space. The graph shows two well separated clusters and the misclassi-

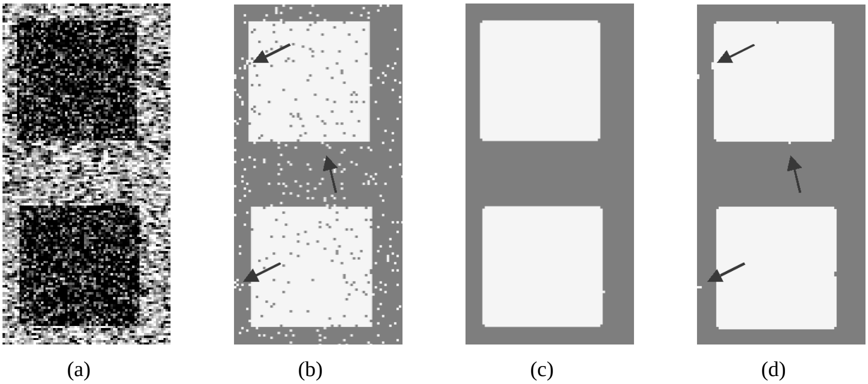

Figure 3.3: *Results of FCM, sg-FCM and FCM-MAJORITY for synthetic RGB image with gaussian noise (*$\mu = 0, \sigma = 10$*). (a) original image contaminated with gaussian noise (*$\mu = 0, \sigma = 10$*); (b) FCM segmented image; (c) sg-FCM segmented image; (d) FCM-MAJORITY segmented image.*

fied foreground and background pixels. Figure 3.3(c) shows the sg-FCM segmented image. The improvement of the segmentation due to the extra spatial information is unambiguous, the two foreground squares and the background are almost correctly segmented. The sg-FCM graph in figure 3.4(c) shows that foreground pixels appear in the background cluster and vice versa. This cluster overlap is a result of the added a-priori spatial information which guides spurious pixels to the other class (the background class pixels which are in the foreground cluster are not clearly visible in the graph because the points of the foreground class are plotted on top of the background class points). The graph shows 8 pixels misclassified as background and a single pixel misclassified to the foreground class. The result of FCM-MAJORITY is shown in figure 3.3(d) and the graph is shown in figure 3.4(d). Although the results of sg-FCM (figure 3.3(c))and FCM-MAJORITY (figure 3.3(d))look very similar, there are differences in multiple regions where spurious pixels are lumped within the 3×3 window. In those regions, the majority filter fails to correct the pixels owing to a abundance of spurious pixels within the window W. Examples of such corresponding regions are indicated by arrows in both the FCM and FCM-MAJORITY segmented images. The lower left arrow indicates such a region in the FCM segmented image in figure 3.3(b). The same region in the FCM-MAJORITY segmented image in figure 3.3(d) shows that the majority filter cannot correct this abundance of pixels which results in two misclassified pixels. The latter example shows the major advantage of sg-FCM, in which pixels are gradually guided to the other class in each iteration. A a

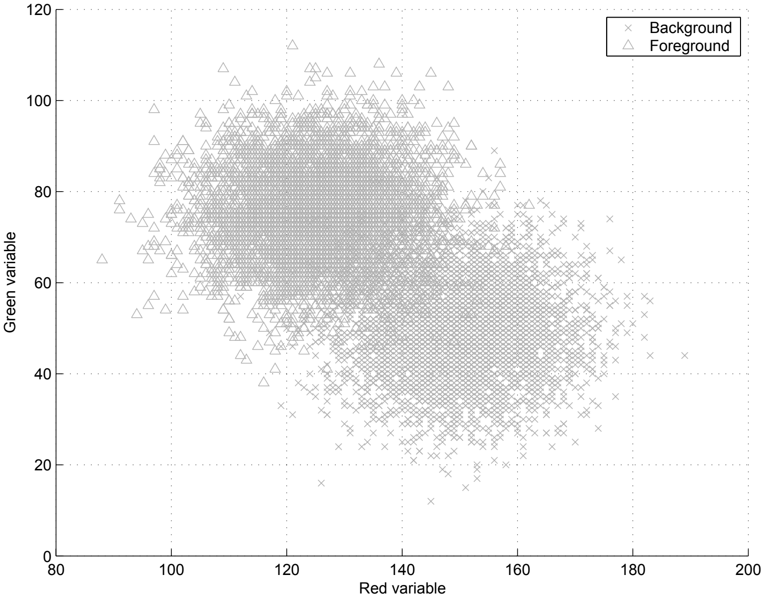
Background
Foreground
Green variable
Red variable
0
20
40
60
80
100
120
80
100
120
140
160
180
200

(a)

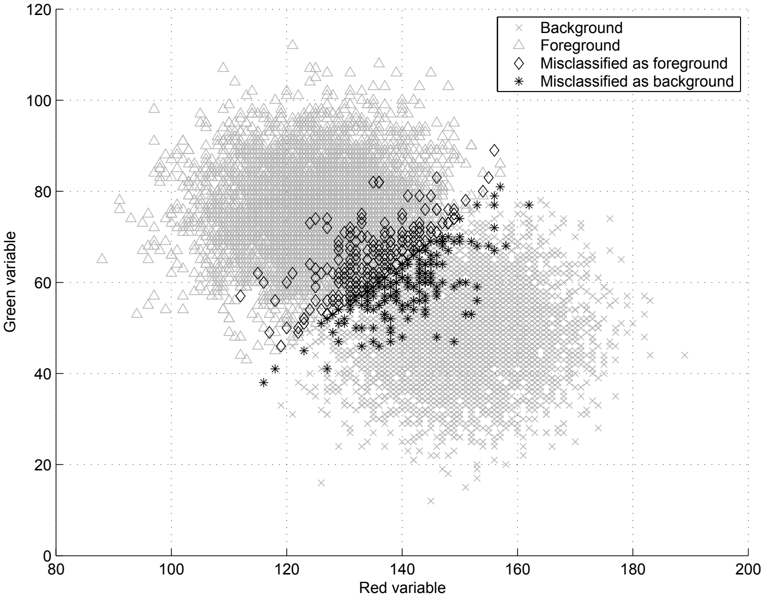
Background
Foreground
Misclassified as foreground
Misclassified as background
Green variable
Red variable
0
20
40
60
80
100
120
80
100
120
140
160
180
200

(b)

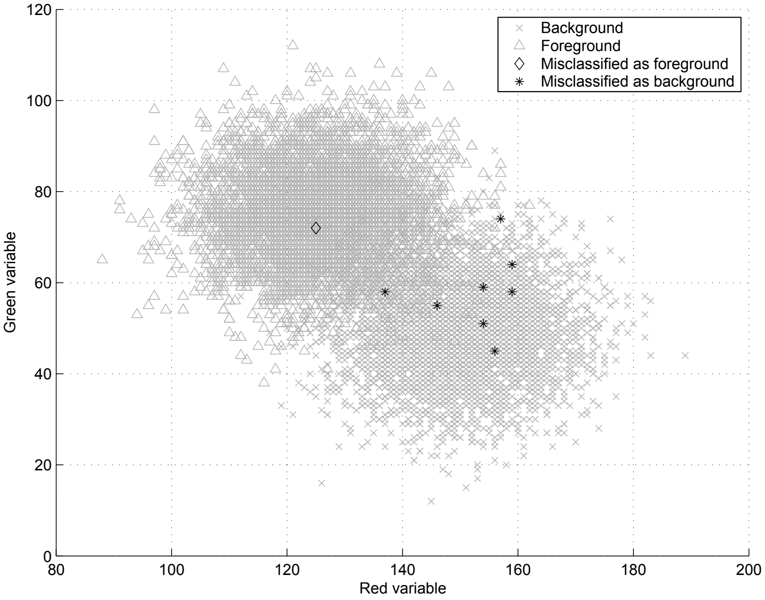

(c)

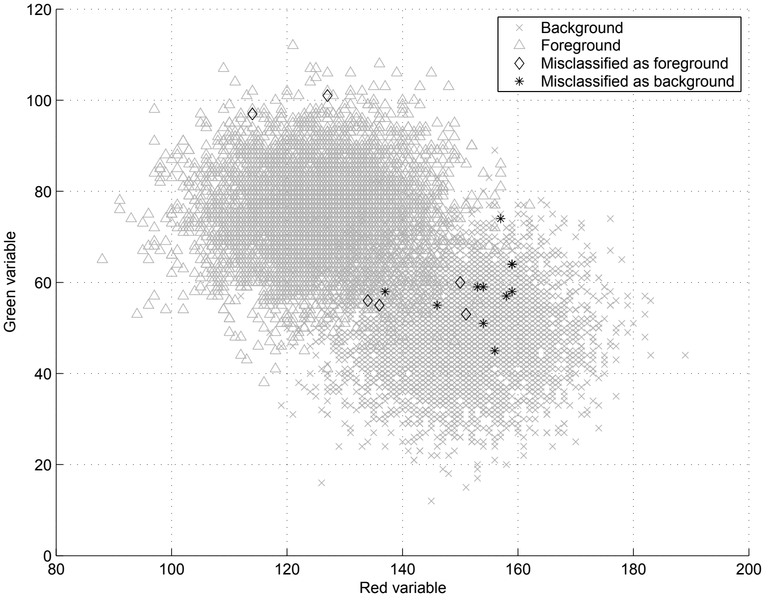

(d)

Figure 3.4: *Graph of Red versus Green variable for original image, FCM, sg-FCM and FCM-MAJORITY for synthetic RGB image with gaussian noise ($\mu = 0, \sigma = 10$). (a) original image; (b) FCM result; (c) sg-FCM result; (d) FCM-MAJORITY result;*

result, stronger spatial guidance is possible in contrast with the FCM + majority filter sequence where the correction must be carried out in a single iteration.

Figure 3.5 shows this effect more clearly where the differences between FCM, sg-FCM and FCM-MAJORITY are depicted in 2 separate graphs for 21 different noise levels. Figure 3.5(a) shows the percentage of misclassified pixels for the 3 corresponding experiments in a single graph. The graph clearly shows that FCM is outperformed by both sg-FCM and FCM-MAJORITY. Figure 3.5(b) shows the enlarged region of figure 3.5(a) between 0-2% of the misclassified pixels. The zoomed graph shows that between experiments 6 and 11 the results of FCM and sg-FCM are more or less equal. For increasing noise levels, the difference becomes more distinct and sg-FCM performs better than FCM-MAJORITY. Here, the noise results in an abundance of spurious pixels that can no longer be corrected by the 3×3 window of the majority filter. For the experiments 1-9 the percentage of misclassified pixels is fixed at 0.08% (8 pixels) for the FCM-MAJORITY approach, whereas the percentage of misclassified pixels of sg-FCM slowly increases with the noise level. As shown in figure 3.3(d), the 8 misclassified pixels correspond with the number of foreground corner pixels of two squares. This result is to be expected as for any foreground corner pixel the number of background pixels is larger(5) than the number of foreground pixels (3)in case of 8-connectivity within the 3×3 window. This is an important drawback of FCM-MAJORITY as in images with many enveloped objects all corner pixels will be misclassified.

3.4.3 Experiment 2: Blob removal in a multivariate potato image

A real-world image of a potato demonstrates how a priori information about a certain blob size can be used to discriminate between objects with similar spectra during clustering. In this experiment,the multivariate image is segmented by FCM, sg-FCM and FCM-MAJORITY. The image is shown in figure 3.6(a). The left image shows a nicola-potato image (233x134 pixels, pixel size= 0.5 mm.). The potato contains spots of different size and origin. The large dark spots are the result of a potato disease and the smaller dark spots located at the lower part of the potato are typical skin spots for this particular potato cultivar. During segmentation, the small skin spots should be ignored because these pixels are misclassified as disease pixels. Without spatial information, one cannot discriminate between the good skin spots and the disease spot, as they have similar spectral properties. Discrimination between the larger disease spots and the smaller skin spots is only possible if a-priori knowledge of spot size is used during clustering. The sg-FCM uses a 5×5-neighbourhood window to add the spatial a-priori knowledge about the skin spot size. In both experiments, the number of clusters is set to 2, m=2, $\varepsilon = 0.0001$ and the euclidian distance measure is used. The results of FCM clustering are shown in figure 3.6(b). As expected, the

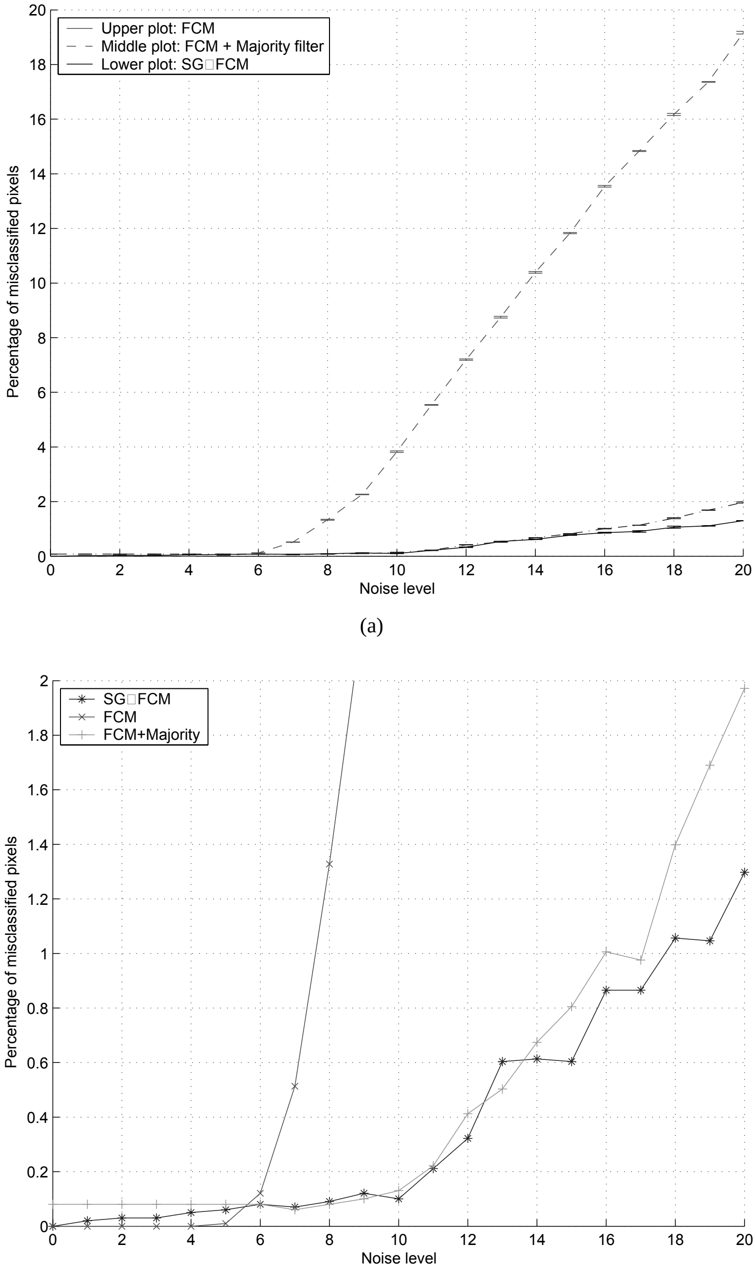

(a)

(b)

Figure 3.5: *(a) Percentage of misclassified pixels for sg-FCM, FCM and FCM-MAJORITY for synthetic RGB image with different noise levels; (b) Zoomed region between 0-2% of misclassified pixels.*

similar coloured small spots are all classified into the disease class. Applying sg-FCM to the potato image gives the results as shown in the image of figure 3.6(c). With the 5×5 window, the pixels of small blobs receive such a condition value that these pixels are guided into the good skin class. The experiment shows that the use of a-priori spatial information of spot size during clustering makes it possible to discriminate between objects with similar spectra. The result of FCM-MAJORITY with a 5×5 window is shown in figure 3.6(d) and indicates that not all of the smaller spots have been removed, in contrast with the sg-FCM result.

3.4.4 Experiment 3: Segmentation of a multivariate image of peppers

In this experiment a multivariate RGB image is segmented with FCM, sg-FCM and FCM-MAJORITY. The image (145x148 pixels, pixel size= 0.5 mm.) consists of peppers of different shape, colour and size. Several specular refections are visible in the image owing to the shiny surface of the peppers. This results in spurious specular pixels and regions which are enveloped by spurious edges. The original image is shown in figure 3.7(a) and contains the classes dark green pepper, light green pepper, red pepper, shadow (black) and specular reflections (white). For the initialization of the FCM and sg-FCM routines, the number of classes is set to 5, m=2, $\varepsilon = 0.0001$ and the euclidian distance is used. A 3×3 window is selected during the sg-FCM clustering which serves as the geometrical model that describes the small edges and spurious pixels. The image shown in figure 3.7(b) is segmented by the traditional FCM. It shows that some of segmented regions are indeed enveloped by spurious edges, especially those regions which corresponds to specular reflections. Figure 3.7(c) shows the result after clustering with sg-FCM with the 3×3 window. Both the spurious pixels and spurious envelopes around the specular regions are removed. The extra spatial information sees to it that spurious edge pixels are merged with the class of the surrounding pixels. The image depicted in figure 3.7(b) is the result of the FCM-MAJORITY segmentation with a 3×3 window. It shows that the greater part of the spurious pixels are removed but almost all of the spurious envelopes are left intact. The images segmented by sg-FCM and FCM-MAJORITY show the difference between both approaches. In sg-FCM, pixels can gradually move to another class after each iteration, whereas the FCM + majority filter combination tries to correct all segmentation errors in a single iteration, which is not always possible.

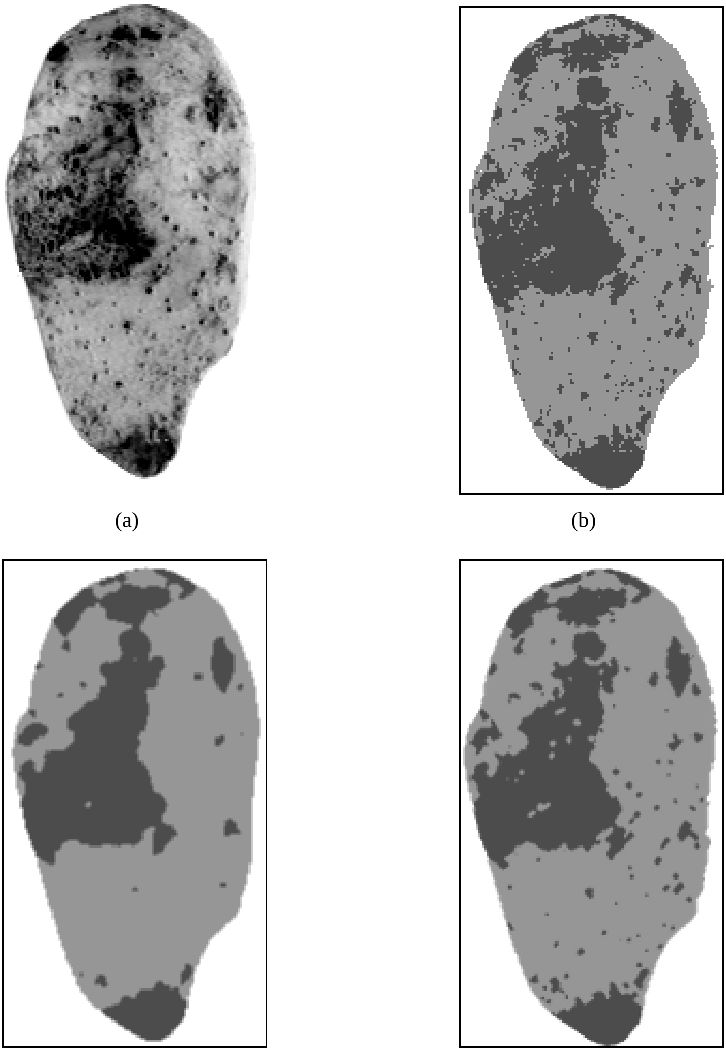

(a) (b)

(c) (d)

Figure 3.6: *Results of traditional FCM, sg-FCM and FCM-MAJORITY for Nicola potato image. (a) original Nicola potato image; (b) FCM segmented image; (c) sg-FCM segmented image; (d) FCM-MAJORITY segmented image.*

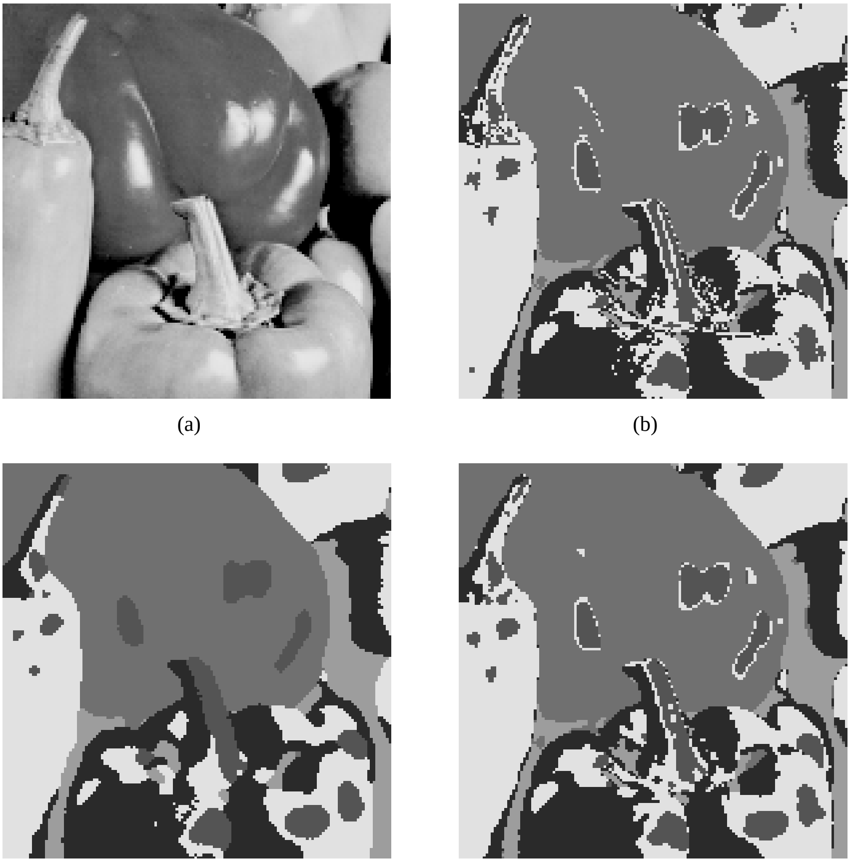

(a) (b)

(c) (d)

Figure 3.7: *Results of traditional FCM, sg-FCM and FCM-MAJORITY for peppers image. (a) original image of peppers; (b) FCM segmented image; (c) sg-FCM segmented image; (d) FCM-MAJORITY segmented image.*

3.4.5 Experiment 4: Circle detection in a multivariate candy image

In this experiment, a multivariate image with different kind of candy of different colour and shape is segmented with sg-FCM, FCM and FCM-MAJORITY. For the initialization for FCM and sg-FCM routines, the number of clusters is set to 4, m=2, $\varepsilon = 0.00001$ and the euclidian distance measure is used. The image size is 320 x 286 pixels (pixel size=0.14 mm.) and is recorded with the ImSpector imaging setup as described in section 3.4.1. Because of computer memory limitation the number of 257 variables of the original multivariate image was reduced to 12 variables, where each plane is the average of 20 planes. E.g. the first 20 wavelengths are averaged to form plane 1, the next 20-40 form plane 2 etc. Although in general this reduction technique may remove small spectral features, it is permitted for this image as the spectra are smooth and do not contain small spectral features within the window of 20 planes. The background of the image contains no information and is removed from the image before the clustering was started. The image contains 4 pieces of rectangular shaped candy, 3 pieces of circular shaped candy (M&M) with a shiny surface and 1 circular shaped candy (peppermint) with a matt surface. Both the circular M&M's and the peppermint have different diameter, which is not known a priori. A pseudo-colour image of the candy is shown in figure 3.8(a). The image contains the colour classes red M&M, blue M&M, white peppermint and dark yellow candy, The shiny surface of the different candy produces specular reflections on most pieces of candy. These reflections influence the segmentation result, as shown in the FCM segmented image of figure 3.8(b) where the reflections are clearly visible on the three smaller circles and the rectangular shaped candy. The FCM classified the specular regions to the class of the two lower rectangular shaped candy bars (light gray). The image also shows that the 4 candy bars and the two lower circles are surrounded by spurious edge pixels which are located on the transition between object and background.

A-priori knowledge such as the homogeneity of the circular shaped candy is used by sg-FCM to remove the specular regions and the spurious edge pixels. The edge image and the detected circles after the Hough transform are shown in figure 3.8(c) and 3.8(d). The Hough image shows that 4 circle candidates have been detected, 3 M&M's and the peppermint. These circle candidates are used to determine the value for the condition f_{ik} in sg-FCM to guide the clustering process. The sg-FCM segmented image, visible in figure 3.8(e), shows that the specular regions of the 3 M&M's have been guided to the correct M&M class. Furthermore, the spurious edge pixels that surrounded the lower M&M and the peppermint are classified correctly.

The FCM-MAJORITY segmented image in figure 3.8(f) shows that only single pixels are removed in the rectangular shaped candy bar. The spurious edges and the specular reflections on the circular candy cannot be removed by the 3×3 majority filter. This is

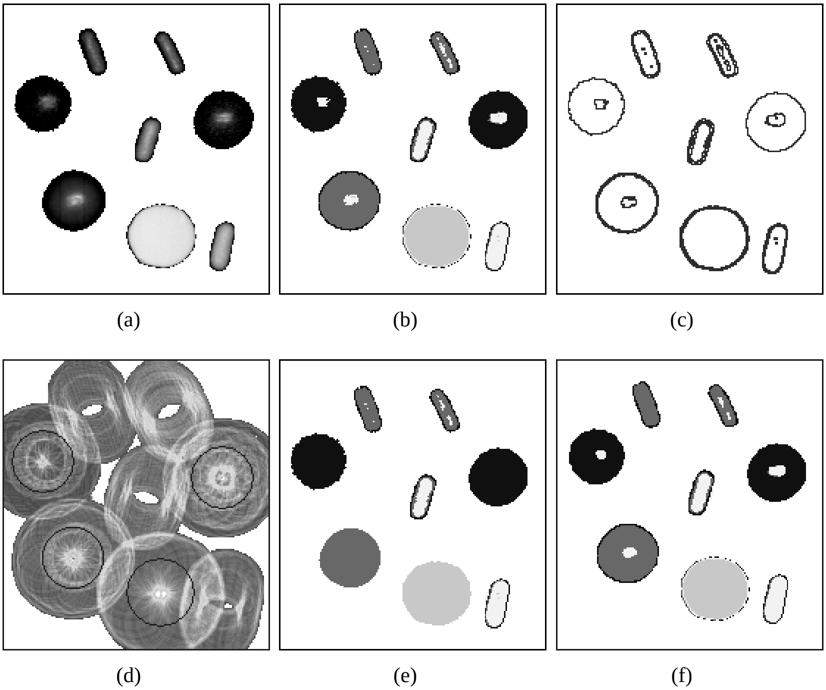

(a) (b) (c)

(d) (e) (f)

Figure 3.8: *Results of traditional FCM, sg-FCM and FCM-MAJORITY for a multivariate candy image. (a) original candy image; (b) FCM segmented image; (c) the detected edges; (d) Hough image with 4 detected circles; (e) sg-FCM segmented image; (f) FCM-MAJORITY segmented image.*

because the FCM + majority filter combination lacks the a-priori spatial information which serves as the geometrical model in sg-FCM for circle detection.

3.5 Conclusion

In this paper, Spatially Guided Fuzzy C-Means (sg-FCM) is presented to segment multivariate images using both spectral and spatial information. The technique is based on Fuzzy C-Means clustering (FCM) and uses information from the spatial domain to guide de spectrally based clustering. The addition of a priori shape information from the spatial domain makes it possible to intervene in the clustering process and correct segmentation errors during clustering. By using specific a priori information reflected by a geometrical shape description, objects of different shape and size can be detected in the multivariate image. The performance of Spatially Guided FCM is compared with both FCM and the sequence of FCM and a majority filter (FCM-MAJORITY) in experiments with multivariate images where spectral information is not sufficient to discriminate between objects. The sg-FCM segmented images showed more homogeneous regions and less spurious pixels compared to FCM and FCM-MAJORITY results.

3.6 Acknowledgements

This work was partially funded by the Dutch Ministry of Economic Affairs under the IOP (Innovation Oriented Research) programme and the Ministry of Agriculture, Nature Management and Fisheries. The authors acknowledge the contribution of G. Polder and G. van der Heijden of Plant Research International in Wageningen with the use of their spectral imaging equipment.

Bibliography

[1] J. Bezdek, *Pattern recognition with fuzzy objective functions*. New York: Plenum Press, 1981.

[2] M. Goldberg and S. Shlien, “A clustering scheme for multispectral images,” *IEEE Transactions on Systems, Man and Cyberbetics*, vol. 8, no. 2, pp. 86–92, 1978.

[3] R. L. Cannon, J. V. Dave, and J. Bezdek, “Efficient implementation of the fuzzy c-means clustering,” *IEEE Transactions on Pattern Analysis and Machine Intelligence*, vol. 8, no. 2, 1986.

[4] L. Hall, A. M. Bensaid, L. Clarke, R. P. Velthuizen, M. S. Silbiger, and J. Bezdek, “A comparison of neural network and fuzzy clustering techniques in segmenting magnetic resonance images of the brain,” *IEEE Transactions on Neural Networks*, vol. 3, no. 5, pp. 672–682, 1992.

[5] M. Yang, “A survey of fuzzy clustering,” *Mathematical and Computer Modelling*, vol. 18, no. 11, pp. 1–16, 1993.

[6] M. R. Rezaee, *Application of fuzzy techniques in image segmentation*. PhD thesis, University of Leiden, 1998.

[7] J. C. Noordam and W. H. A. M. van den Broek, “Multivariate image segmentation based on geometrically guided fuzzy c-means clustering,” *Journal of Chemometrics*, vol. 16, pp. 1–11, 2002.

[8] J. Bezdek, L. Hall, and L. Clarke, “Review of MR image segmentation techniques using pattern recognition,” *Medical Physics*, vol. 20, no. 4, pp. 1033–1048, 1993.

[9] A. O. Boudraa, “Automated detection of the left ventricular region in magnetic resonance images by fuzzy c-means model,” *International Journal of Cardiac Imaging*, vol. 13, pp. 347–355, 1997.

[10] S. H. Park, I. D. Yun, and S. U. Lee, “Color image segmentation based on 3D clustering: a morphological approach,” *Pattern Recognition*, vol. 21, no. 8, pp. 1061–1076, 1998.

[11] T. N. Pappas, “An adaptive clustering algorithm for image segmentation,” *IEEE Transactions on Signal Processing*, vol. 40, no. 4, pp. 901–914, 1992.

[12] Y. A. Tolias and S. M. Panas, “Image segmentation by a fuzzy clustering algorithm using adaptive spatially constrained membership functions,” *IEEE Transactions on Systems, Man and Cybernetics*, vol. 28, no. 3, 1998.

[13] J. Theiler and G. Gisler, “A contiguity-enhanced k-means clustering algorithm for unsupervised multispectral image segmentation,” in *Proceedings of SPIE*, vol. 3159, pp. 108–118, 1997.

[14] P. Paclik, R. P. W. Duin, and G. v. Kempen, “Multi-spectral image segmentation algorithm combining spatial and spectral information,” in *SCIA 2001*, (Bergen, Norway), 2001.

[15] S. Roberts, G. Gisler, and J. Theiler, “Spatial-spectral image analysis using classical and neural algorithms,” in *Proceedings of the Artificial Neural Networks in Engineering*, pp. 425–430, ASME press, New York, 1996.

[16] W. Pedrycz and J. Waletzky, “Fuzzy clustering with partial supervision,” *IEEE Transactions on Systems, Man and Cybernetics*, vol. 27, no. 5, pp. 787–795, 1997.

[17] J. Illingworth and J. Kittler, “A survey of the hough transform,” *Computer Graphics and Image Processing*, vol. 44, pp. 87–116, 1998.

[18] H. Yuen, J. Princen, J. Illingworth, and J. Kittler, “Comparative study of Hough transform methods for circle finding,” *Image and Vision Computing*, vol. 8, no. 1, pp. 71–77, 1990.

[19] G. Gerig and F. Klein, “Fast contour identification through efficient Hough transform and simplified interpretation strategy,” in *8th International Conference on Pattern Recognition*, pp. 498–500, IEEE Computer Society, 1986.

[20] G. Polder, G. van der Heijden, and I. Young, “Spectral image analysis for measuring ripeness of tomatoes,” *Transactions of the ASAE*, vol. 45, no. 4, pp. 1155–1161, 2002.

Chapter 4

Multivariate image segmentation with cluster size insensitive Fuzzy C-Means

Abstract

This paper describes a technique to overcome the sensitivity of fuzzy C-means clustering for unequal cluster sizes in multivariate images. As FCM tends to balance the number of points in each cluster, cluster centers of smaller clusters are drawn to larger adjacent clusters. In order to overcome this, a modified version of FCM, called Conditional FCM, is used to balance the different sized clusters. During the clustering process, the ratios between the cluster sizes are determined and a corresponding condition is calculated. This condition value balances the influence of objects from larger clusters to smaller clusters. Experiments with the cluster size insensitive FCM (csi-FCM) on different numerical datasets, synthetic and real multivariate images for different number of clusters and cluster sizes show the improvement compared to FCM and FMLE.

4.1 Introduction

The present consumer market demands high quality vegetables and fruits. Some consumer criteria are related to the presence of external defects, deformations and visible diseases. Inspection systems based on image analysis offer a possibility to inspect the quality of these products in advance. To detect external defects existing visual inspection systems available on the market use gray-value or colour cameras. However, the discrimination between similar defects can be a burden for these camera systems [1]. Furthermore, latent defects or diseases remain invisible for these systems. The detection of these latent defects is of great importance as these defects affect the long-term quality of the product. Only use of the spectral properties of the constituents of these defects offers possibilities to determine latent defects and discriminate between similar defects. Multivariate images such as produced by Magnetic Resonance Imaging (MRI) devices and multispectral cameras reveal information about the constituents of the product under inspection. In cases where only a single image or a few images with no a priori spectral information is available, no training set can be extracted from these images to train a supervised classifier. Fuzzy C-Means (FCM) is especially applied as an unsupervised segmentation technique for those images [2, 3]. The unsupervised nature of FCM and its ability to detect clusters of different shape such as spherical, elliptical, shells and lines makes it a versatile and popular technique [4, 5] for the segmentation of Magnetic Resonance (MR) images [6, 7], multispectral images [2, 8] and Red/Green/Blue (RGB) color images [9, 8]. Such multivariate images are produced by computer vision based inspection systems [1] where cameras inspect the product for defects. The computer segments the image into several classes and the number of pixels in each class is counted. Based on the number of pixels within a class and a predefined threshold value, the computer accepts or rejects the product under inspection. For those type of multivariate images with multiple classes, the number of pixels in a defect class, which represents the defects, is much lower than the pixels in the remaining classes.

When FCM is applied as a clustering technique to segment these images, care should be taken when the number of pixels in the different classes diverge. The center of the smaller clusters tends to drift to the adjacent larger clusters. As a result, the partitioning of the data space, and thus the final segmentation, will be influenced by this cluster size sensitivity. Incorrect segmentation may result in a false rejection of the product under inspection.

The sensitivity for unequal cluster sizes is a well-known drawback of all least-squares-based algorithms [6, 10]. The reason for this tendency is that FCM uses a sum of squared errors objective function and approximately-equal cluster populations result in smaller values of this objective function [11, 12]. As a result, FCM solutions tend to equalize cluster populations.

In literature, two FCM based techniques have been reported that overcome this cluster size sensitivity [13, 3]. The semi-supervised FCM (ssFCM) algorithm [3] is a FCM based clustering technique that uses weight factors to balance the different cluster sizes. It uses the Euclidean norm as a measure of distance to search for hyperspherical shaped clusters. Objects in small clusters receive higher weight factors than objects in larger clusters. Objects with higher weight factor prevent the centers of small clusters from drifting towards larger clusters. The user must select the objects that receive a weight factor and also determine the value for this weight factor. This user intervention requires a-priori information about the final classes of the objects and the cluster sizes, which may not always be available a-priori. Another difficulty of this method is that the value of these weight factors is dataset size dependent.

The second alternative for the cluster size sensitive FCM is the Fuzzy Maximum Likelihood Estimation (FMLE) algorithm [13], which accounts for variations in cluster shapes, cluster densities and the number of pixels in each class. The exponential distance function of the FMLE algorithm requires the computation of the clusters covariance matrices and their corresponding inverses. The computation of such a covariance matrix requires a large number of training points. In practice, only a finite number of points are used to estimate the covariance matrix. If there are not enough data points available in the dataset, the covariance matrix becomes singular and the FMLE algorithms breaks down. Besides the risk of covariance matrix singularity there is also the computation time property. As the dimension of the data increases, the calculation of the covariance matrix, the inverse covariance matrix and the determinant becomes more and more time consuming [14, 9]. These two issues make the FMLE algorithm less suitable as an alternative for the cluster size sensitive FCM and this probably explains why the FCM with the Euclidian distance is preferred in many applications for the segmentation of multivariate images [9].

The FCM-based technique presented in this paper overcomes the cluster size sensitivity of FCM. It requires neither a-priori information about the final classes of the objects nor information about the size of the clusters. During clustering, the a-priori cluster probability is determined and updated after each iteration. This cluster probability is used to balance the unequally sized clusters between intermediate iterations. This has resulted in a cluster size insensitive version of FCM (csi-FCM) suited for the segmentation of multivariate images.

The paper is organized as follows: Section 4.2 discusses the FCM algorithm and the principle of csi-FCM. Section 4.3 shows the results of experiments with small numeric datasets, synthetic and real world multivariate images. For small numeric datasets, the performance of csi-FCM is compared with the performance of both FCM and ss-FCM. For the segmentation of multivariate images obtained from computer vision based inspection systems, the results of csi-FCM are compared with the results of FCM and FMLE. In the last section, the conclusions are given.

4.2 Theory

4.2.1 Fuzzy C-Means clustering (FCM)

Given a set of n data patterns, $X = \mathbf{x}_1, ..., \mathbf{x}_n$, the FCM algorithm minimizes the weighted within group sum of squared error objective function $J(U,\mathbf{V})$ [11]:

$$J(U,\mathbf{V}) = \sum_{k=1}^{n} \sum_{i=1}^{c} u_{ik}^{m} d^2(\mathbf{x}_k, \mathbf{v}_i) \tag{4.1}$$

where $\mathbf{x}_k$ is the k-th p-dimensional data vector, $\mathbf{v}_i$ is the prototype of the center of cluster i, u_{ik} is the degree of membership of $\mathbf{x}_k$ in the i-th cluster, m is a weighting exponent on each fuzzy membership, $d(\mathbf{x}_k, \mathbf{v}_i)$ is a distance measure between object $\mathbf{x}_k$ and cluster center $\mathbf{v}_i$, n is the number of objects and c is the number of clusters. A solution of the objective function $J(U,\mathbf{V})$ can be obtained via an iterative process where the degrees of membership u_{ik} and the cluster centers $\mathbf{v}_i$ are updated via:

$$u_{ik} = \frac{1}{\sum_{j=1}^{c} \left(\frac{d_{ik}}{d_{jk}} \right)^{\frac{2}{m-1}}} \tag{4.2}$$

with d_{ik} the distance between object k and cluster i, d_{jk} the distance between object k and cluster j,

$$\mathbf{v}_i = \frac{\sum_{k=1}^{n} u_{ik}^{m} \mathbf{x}_k}{\sum_{k=1}^{n} u_{ik}^{m}} \tag{4.3}$$

with the constraints:

$$u_{ik} \in [0,1], \qquad \sum_{i=1}^{c} u_{ik} = 1 \quad \forall k, \qquad 0 < \sum_{k=1}^{n} u_{ik} < N \quad \forall i \tag{4.4}$$

According to the update formula for the cluster prototypes (equation 4.3), objects with low membership values for that particular cluster have a small contribution to the final position of that particular cluster prototype. This is the general principle on which csi-FCM is based: by weakening membership values of objects that belong to the larger cluster, the contribution of those weakened objects to the cluster centers of the smaller clusters will be small. As a result, the cluster centers of the smaller clusters will not drift to the larger adjacent cluster. A modified version of FCM, called conditional FCM [15], is used to weaken the membership values of objects. The principle of conditional-FCM is discussed in the next section.

4.2.2 Conditional Fuzzy C-Means clustering

Conditional FCM (c-FCM) is a FCM based clustering technique where the clustering is influenced by an auxiliary variable to guide the outcome of the clustering process. The original idea of c-FCM is that in cases where clustering is used and some a-priori information is available, it might be advantageous to use this a-priori information to influence the clustering process [15]. This a-priori information is translated in a value for the auxiliary variable, which influences the clustering. A fixed value for this auxiliary variable is given beforehand or the value is continuously updated during clustering [8]. The principle of c-FCM is as follows: For each labelled pattern $\mathbf{x}_k$, there exists an auxiliary condition variable f_k, further referred to as condition, where f_k ranges from [0,1]. The update procedure for the partition matrix U is now changed into:

$$u_{ik} = \frac{f_k}{\sum_{j=1}^{c} \left(\frac{d_{ik}}{d_{jk}} \right)^{\frac{2}{m-1}}} \tag{4.5}$$

with the modified constraint

$$\sum_{i=1}^{c} u_{ik} = f_k \tag{4.6}$$

For condition values equal to 1, the object is unconditioned and the partition update procedure is similar to the partition update procedure of FCM. A small value of the condition results in a low membership value for all clusters, which minimizes the contribution of that particular object to all cluster centers.

4.2.3 Cluster size insensitive FCM (csi-FCM)

The general principle of the technique presented in this paper is to weaken the contribution of objects from larger clusters to the prototypes of smaller clusters to prevent smaller clusters from drifting towards larger adjacent clusters. This is achieved by assigning low conditional values to objects of larger clusters and giving high conditional values to objects of smaller clusters. As a result, objects with low membership values u_k for cluster i contribute less to the final position of cluster prototype i, according to equation 4.3. Objects of the smallest cluster are unconditioned, their contribution to the prototype of the smallest cluster is maximal when the condition f_k for these objects is set to 1. The objects of the remaining clusters receive a condition which is less then 1 ($f_k < 1$) to minimize their contribution to the prototype of the smaller clusters. The condition value is determined by P_i, the a-priori probability of selecting the ith cluster:

$$P_i = \frac{N_i}{N} \tag{4.7}$$

where N_i is the number of points in cluster i after defuzzification and N is the total number of points in the dataset. The a-priori cluster probabilities are determined and updated during clustering by converting the fuzzy partition matrix U to a crisp partition matrix. The procedure of maximum membership is used to defuzzify each object in the partition matrix U. The maximum membership procedure assigns object k to the class C with the highest membership:

$$C_k = arg_i\{max_{(i=1,2,...,c)}(u_{ik})\} \tag{4.8}$$

Objects which are classified to class i during the defuzzification stage receive a condition equal to:

$$f_{k,i} = 1 - P_i \tag{4.9}$$

where $f_{k,i}$ is the condition for an object k classified to class i in the defuzzification stage.

As stated above, the contribution of objects from the smallest cluster to the prototype of the smallest cluster is maximal when the condition of these objects is set to 1. In order to obtain a condition f_k=1 for the objects of the smallest cluster, a scaling is required for the conditions. First,the smallest prior probability is determined:

$$P_{i_{\min}} = P_i \quad | \quad P_i < P_j; \quad j = 1,2,...,c; \quad i \neq j \tag{4.10}$$

Now the scale factor is determined as to scale all condition values:

$$ScaleFactor = \frac{1}{1 - P_{i_{\min}}} \tag{4.11}$$

Combining the scalefactor and the condition results in a condition value $f_{k,i}$ for object k classified to class i:

$$f_{k,i} = \frac{1}{(1 - P_{i_{\min}})} * (1 - P_i); \qquad i = 1,2,...,c \tag{4.12}$$

The equation above shows that in cases when $P_i = P_{i_{min}}$, the objects of the smallest cluster are unconditioned.

After each iteration step, the error between iteration t and the previous iteration $t-1$ is calculated:

$$E_t = \|U_t - U_{t-1}\| \tag{4.13}$$

If error E_t is below a predefined value of the stop criterion ε, a new iteration step of the csi-FCM starts with a new condition $f_{k,i}$ for each object. The value for the stop criterion ε is set beforehand, identical as with FCM. To prevent that the csi-FCM gets trapped in a local minima, the csi-FCM algorithm is initialized with FCM. Once the FCM is stopped, the csi-FCM algorithm continues with the values for the centroids and membership values obtained from the FCM iteration.

4.3 Experiments

Experiments have been carried out to compare the performance of csi-FCM with three different FCM based techniques. In the first experiment, a known numeric dataset with unequal cluster sizes is considered to compare the csi-FCM results with ssFCM and FCM. In the second experiment, the results of segmenting a synthetic multivariate image with unequal classes with FCM, csi-FCM and FMLE are compared. The experiment is repeated for different noise levels to simulate different degrees of cluster overlap. In the third experiment, the sensitivity of the initialization of both csi-FCM and FMLE are compared. As both algorithms use FCM to initialize the values for the prototypes, the effect of using different values for the stop criterion ε is studied. In the last 2 experiments, real world multivariate images with an unequal number of pixels per class are segmented with FCM, FMLE and csi-FCM to compare the segmentation performance. Unless mentioned otherwise, random numbers are used for the initialization of the cluster centres. The maximum membership procedure is used in all experiments to convert the fuzzy partition matrix to a crisp partition matrix.

4.3.1 Instrumentation

Two different experimental setups are used to record the multivariate images. The potato image in experiment 4 is recorded with a 3 CCD Sony camera where a prism in the camera splits the incoming light of the visible electromagnetic spectrum into a red, green and blue part for each corresponding CCD. The 3 CCD images are digitized by a framegrabber in the computer combined to a multivariate color image with 3 variables (Red, Green and Blue). The values for red, green and blue in the synthetic color images of experiment 2 are created manually via the computer.

The multispectral minced meat image in experiment 5 is recorded with an ImSpector V7 imaging spectrograph (Spectral Imaging Ltd. Oulu, Finland) mounted on a Peltier cooled Qimaging PMI-1400EC monochrome camera. The ImSpector V7 produces a multispectral image where the 396-736 nm part of the electromagnetic spectrum is recorded in 257 small bands (every 1.3 nm) for every pixel. The incoming light is split by a prism-grating-prism and projected on the 2 dimensional CCD in the camera. One dimension of the CCD records the line pixels (spatial axis) and the other dimension contains the spectral information (spectral axis) of each pixel. A 2-dimensional spectral image is obtained by moving the object under the ImSpector during recording. Detailed information about the used multispectral imaging setup is described in literature [16].

4.3.2 Experiment 1: numerical example with unequal clusters

In this experiment, two known datasets with 2 and 3 classes are used [6]. Dataset number 1 consists of 43 two-dimensional vectors falling into 1 of 2 groups. The larger group is made up of 40 points and the smaller group contains 3 points. Dataset number 2 consists of 3 groups, the largest group consists of 40 points, the second largest group consists of 6 points and the smallest group is made up of 3 points. Figure 4.1(a) shows the results of clustering with FCM using c=2, m=2, $\varepsilon = 0.00001$ and the Euclidean norm. The figure shows that the center of the smaller cluster drifts to the larger cluster due to the tendency of FCM to equalize the number of points in the cluster. With csi-FCM, the centers of smaller clusters are prevented from drifting to larger clusters by assigning low conditional values to all objects of the larger cluster. As a result, objects with low condition values have less influence on the position of the prototype of the smaller cluster and the prototype stays at its original position. This is shown in figure 4.1(b) where the csi-FCM finds the desired clusters correctly.

Figure 4.2 shows the result for a dataset with 3 classes. Again, FCM assigns objects from the larger cluster to the smaller cluster in order to equalize the number of points in each cluster. Figure 4.2(b) shows that csi-FCM can handle multiple unequal classes, the desired clusters are found correctly. The ssFCM algorithm and the csi-FCM algorithm give similar result for both experiments, only csi-FCM requires no a-priori information.

4.3.3 Experiment 2: segmentation of a synthetic image with 3 unequal classes

Figure 4.3(a) shows a synthetic multivariate image with 3 variables (Red, Green and Blue) and 3 classes: a background class (R=125, G=75, B=50), a square class (R=150, G=50, B=50), which consists of 2 equally sized squares, and a rectangle class (R=150, G=75, B=50). The image contains 9940 pixels, the background contains of 8145 pixels, the 2 small squares both contain 1080 pixels and the small horizontal rectangle contains 715 pixels. The value of a pixel in a single image plane ranges between 0 and 255. Gaussian noise is added to the image to simulate adjacent clusters with different overlap. The noise varies in range from $\mu = 0$, $\sigma = 0$ to $\mu = 0$, $\sigma = 8$, resulting in 8 images of increasing cluster overlap. The images are segmented with FCM, csi-FCM and FMLE with parameters c=3, m=2, $\varepsilon = 0.00001$. The true cluster center values are used as initial values for the cluster centers to verify that the results are not affected by centroid initialization. The number of misclassified pixels for FCM, csi-FCM and FMLE are counted during the experiments and are listed in table 4.1 for the 8 different noise values. The FMLE was not able to segment the first synthetic image as this image contained no noise and thus no covariance ma-

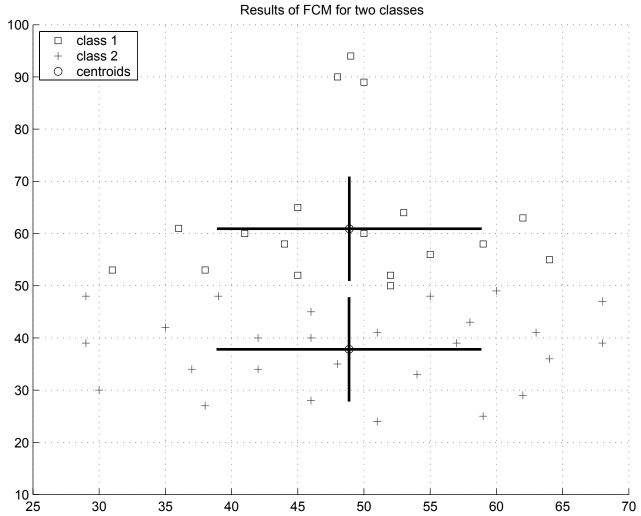

(a)

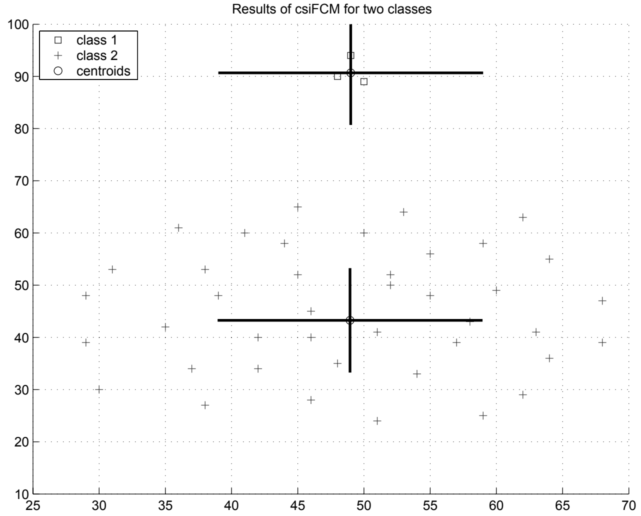

(b)

Figure 4.1: *Two clusters of unequal size. (a) Results of clustering with FCM, (b) Results of clustering with csi-FCM.*

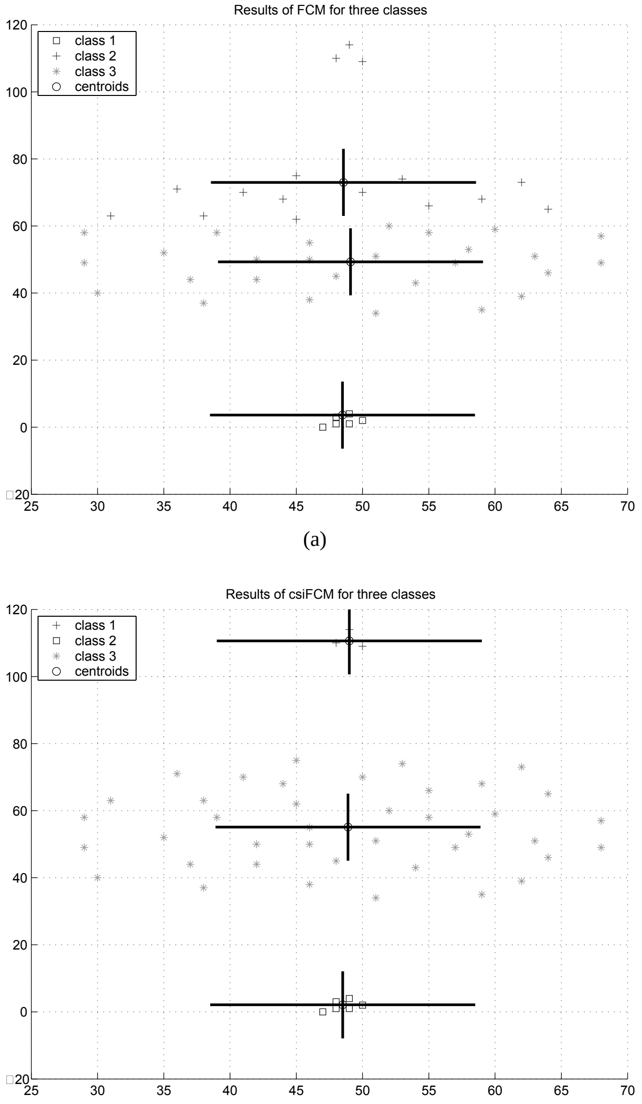

(a)

(b)

Figure 4.2: *Three clusters of unequal size. (a) Results of clustering with FCM, (b) Results of clustering with csi-FCM.*

trix could be estimated. The results show that the csi-FCM and the FMLE algorithm outperform the FCM algorithm for all noise levels. It shows that the number of misclassified pixels for FCM increases rapidly, even for small values of the noise. As the cluster overlap increases, the FMLE algorithm performs better than the csi-FCM.

image no.	noise variance	# misclassified pixels FCM	# misclassified pixels csi-FCM	# misclassified pixels FMLE
1	0	0	0	NA
2	1	0	0	0
3	2	0	0	0
4	3	76	3	13
5	4	3594	49	49
6	5	3795	148	83
7	6	3964	339	265
8	7	4191	584	425

Table 4.1: *Number of misclassified pixels after clustering with FCM, csi-FCM and FMLE at different noise levels.*

To visualize the difference of clustering outcome between FCM and csi-FCM, the result of image 6 (noise $\mu = 0$, $\sigma = 5$) is shown. The FCM segmented image in figure 4.3(b) shows that the background and the small rectangle class are not well segmented, pixels of the square class appear in the rectangle and pixels of the rectangle class appear in the background. The corresponding plot of the Red versus Green variable, as shown in figure 4.4(a), explains this. The plot shows that the center of the small rectangle cluster is closely located to the center of the adjacent larger background cluster. As a result of this, pixels of the rectangle class are classified both to the background class and the square class. Furthermore, pixels of the background class are classified as rectangle. Although the 2 squares are correctly segmented, the plot shows that the prototype of the cluster is not positioned in the center of the cluster, which indicates that this prototype is also drawn to the larger background cluster. Figure 4.3(c) shows the segmented image after clustering with csi-FCM. The 3 different objects are clearly visible and only few pixels are misclassified. The 3 corresponding clusters are clearly visible in the plot, as shown in figure 4.4(b). The prototypes are located in the center of the cluster, which indicates that the larger background cluster does not affect the location of the smaller cluster centners. The image depicted in figure 4.3(d) visualizes the condition value for each pixel. A dark color represents a low condition value and a white value corresponds with a high condition value. As expected, the majority of background pixels receive a low condition and the pixels of the small rectangle remain unconditioned, the condition for those pixels is set to 1.

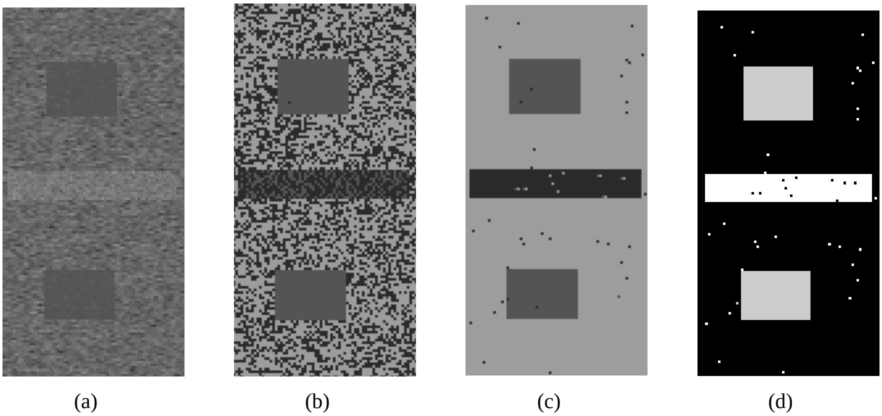
(a) (b) (c) (d)

Figure 4.3: *Synthetic image with noise* $\mu = 0$, $\sigma = 5$ *containing three classes of unequal size, a background class, a square class and a rectangle class. (a) Original noisy image with three classes; (b) Results of clustering with FCM; (c) Results of clustering with csi-FCM; (d) Conditional image generated by csi-FCM.*

4.3.4 Experiment 3: sensitivity to the initialization of csi-FCM and FMLE

As only the csi-FCM and the FMLE algorithm require an initial partition of the dataset by FCM, a sensitivity analysis is performed. In this experiment, synthetic image 6 from experiment 2 is used with noise level $\mu = 0$, $\sigma = 5$. The value of the stop criterion ε for FCM is varied and in two experiments the effect on the csi-FCM and FMLE clustering result is evaluated. The FCM stop criterion ε ranges from 0.05 till 1.0 in steps of 0.05, which results in 20 experiments with different values for the stop criterion. For each value of ε, the experiment is repeated 10 times with random initialization values for the cluster centroids. The initialization values are stored and used in the FCM for both the csi-FCM and FMLE experiment. The csi-FCM and the FMLE algorithm stop when the number of misclassified pixels no longer decreases or when the algorithm is trapped in a local minimum. The average number of runs, the number of local minima and the required computation time are shown in table 4.2. The results of the initialization sensitivity experiment show that csi-FCM always converges to a minimum and correctly partitions the dataset. The FMLE algorithm conversely, fails 84 out of 200 runs to partition the dataset correctly and ends in a local minima. From the experiment, it turned out that there is no correlation between the absolute value of ε used to stop the FCM and the occurrence of a false

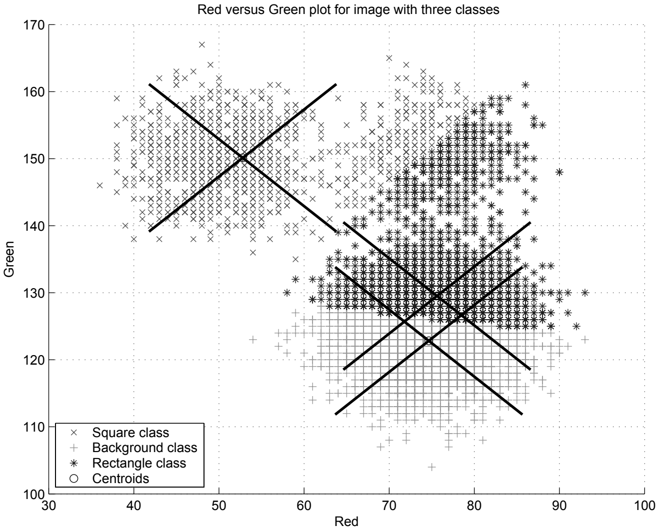

(a)

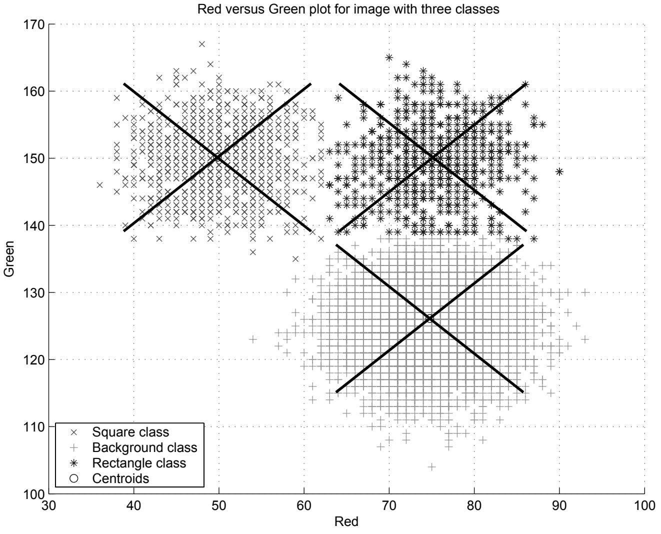

(b)

Figure 4.4: *Plot of Red versus Green variable after clustering the synthetic image. (a) Results of clustering with FCM; (b) Results of clustering with csi-FCM.*

	csi-FCM	FMLE
Number of iterations	21.6	23.1
Average computation time (sec.)	8.28	15.23
Number of local minima	0	84

Table 4.2: *Results of initialization sensitivity of csi-FCM and FMLE after 200 runs.*

minima. A false minima occurs when the initialization values for the cluster centers are not well selected and do not depend of the absolute value of ε. The results do show that csi-FCM is less sensitive for cluster centroid initialization in comparison with FMLE. Furthermore, FMLE requires more iterations and thus more computation time to achieve the same partition.

4.3.5 Experiment 4: segmentation of a multivariate potato image

In this experiment, a part of a multivariate potato image is segmented in 3 classes. The image contains the classes potato skin, potato greening (large area in the left top of figure 4.5(b)) and the fungus rhizoctonia (black spots). The subimage is segmented with FCM, csi-FCM and FMLE using c=3, m=2, $\varepsilon = 0.00001$. The FCM clustering results are shown in figure 4.5(c). The segmented image shows that FCM erroneously merges the classes greening and black spots and oversegments the larger potato skin class in two different classes in order to equalize the number of pixels per cluster. As a result, the black spot class remains undetected due to the small number of pixels in this class. Figure 4.5(d) shows the segmented image after clustering with csi-FCM. The 3 different classes are correctly segmented, the black spot class and the greening class are nog longer merged and the pixels of the potato skin class are in a single class. The conditional image of figure 4.5(e) shows the condition of each pixel. Again, the colors vary from white (high condition value) to dark (low condition value). In the image, the white color of the black spot class pixels indicate that these pixels are unconditioned, as this class is the minority class. The pixels of the potato skin class receive a low value for the condition, as this class is the largest class. The corresponding plots of the Red versus Green variable of the FCM and csi-FCM are shown in figure 4.6. The effect of conditioning is clearly visible in the csi-FCM plot. The center of the smaller black spot class is no longer drawn to the adjacent greening class, which is the case in the FCM-plot of figure 4.6(a). The plot also shows that the conditioning not only affects the center of the smallest cluster, all cluster centers are positioned at different locations after the csi-FCM clustering. The potato image is also segmented with FMLE and the results of both algorithms are the

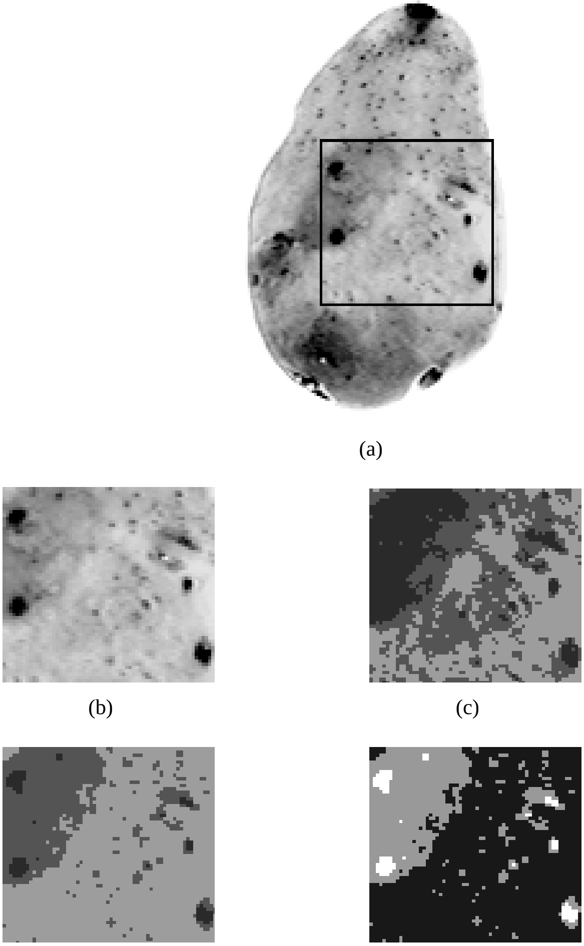

(a)

(b)

(c)

(d)

(e)

Figure 4.5: *Segmenting a potato image with 3 classes: good skin, greening and black spots. (a) Original potato image; (b) Subimage; (c) Results of clustering with FCM; (d) Results of clustering with csi-FCM; (e) Conditional image generated by csi-FCM.*

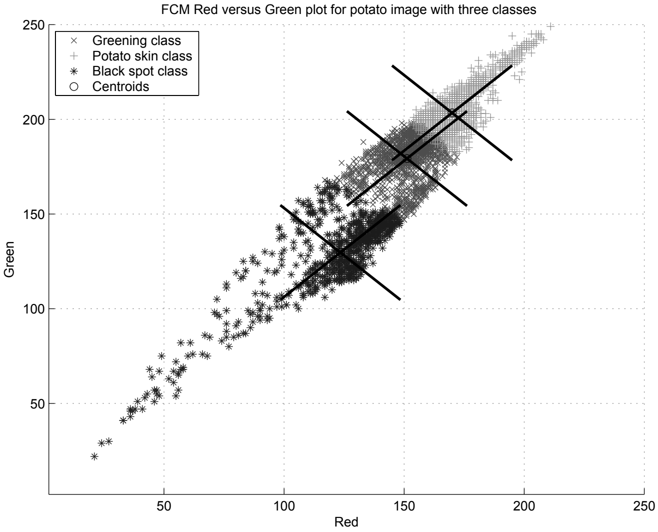

(a)

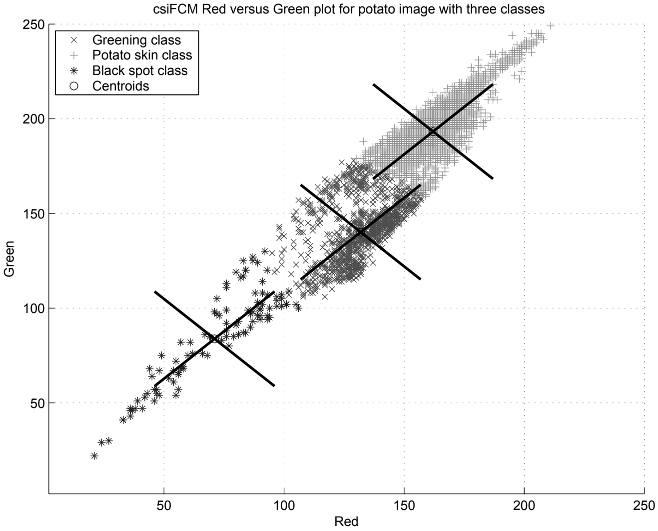

(b)

Figure 4.6: *Plot of Red versus Green variable after clustering potato subimage. (a) Results of clustering with FCM; (b) Results of clustering with csi-FCM.*

same. Although the required number of iterations is the same for both FMLE and csi-FCM, the required computation time differs. The average required computation time after 10 runs is 14.8 seconds for csi-FCM and 22.2 seconds for FMLE.

4.3.6 Experiment 5: segmentation of a multivariate image of minced meat

In this experiment, a multivariate image with 4 unequal classes is segmented with FCM, csi-FCM and FMLE using c=4, m=2, $\varepsilon = 0.00001$. The image is recorded with the ImSpector imaging setup as described in section 4.3.1. The number of 257 variables of the original multivariate image is reduced otherwise a covariance matrix and its inverse, required by the FMLE algorithm, cannot be calculated due to computer memory limitation. Therefore, the image is reduced to 12 planes, where each plane is the average of 20 planes. E.g. the first 20 wavelengths are averaged to form plane 1, the next 20-40 form plane 2 etc.

The image size is 320 x 286 pixels. The image contains a petri disk filled with a piece of minced meat with the classes petri disk, dark meat, light meat and fat, as shown in figure 4.7(a). The difference between dark meat and light meat is caused by the amount of blood in the meat. The dark gray pixels represent the dark meat class and the white spots represent the fat class. The light meat class surrounds the fat class and gradually turns into the dark meat class. The classes dark meat, light meat and fat contain overlap and are therefore hard to separate. The entire image is segmented in the experiment but only the subimages are shown to improve the visualization of the differences. Random values for the centroids are selected and the experiment is repeated for 10 times. The average number of iterations required by FCM, csi-FCM and FMLE after 10 runs are shown in table 4.3. The results of the preceding FCM initialization are not included in the results of both csi-FCM and FMLE. The results in table 4.3 indicate that the FMLE converges not as fast as csi-FCM, the FMLE requires more than 3 times the number of iterations compared to csi-FCM. Further-

	FCM	csi-FCM	FMLE
Number of iterations individual algorithm	73	49	168
Average computation time for segmentation (sec.)	560	398	3297
Average computation time for a single iteration (sec.)	7.7	8.1	19.6

Table 4.3: *Results segmenting the multivariate minced meat image with FCM, csi-FCM and FMLE.*

more, a single iteration of FMLE requires 2.4 more computation time because of the calculation of the covariance matrix and its inverse for each cluster. This makes the csi-FCM 8.3 times faster than FMLE for this multivariate image. Table 4.4 shows the average percentage of pixels per class for the three algorithms after segmentation. The percentage of pixels classified as petri disk is approximately equal for the 3 experiments, which is to be expected as this class is quite distinctive from the remaining classes. The difference between the FCM segmented image and the csi-FCM segmented image is most distinctive in the fat class. The FCM classifies 11.7% of the pixels as fat, as shown in figure 4.7(c), whereas the csi-FCM classifies merely 6.4% of the pixels as fat, shown in figure 4.7(d). The percentages of the pixels per class in table 4.4 show that not only the fat class is affected by the conditioning, also the number of pixels in the light meat and dark meat class is different compared to the FCM segmented image.

	petri disk	dark meta	light meat	fat
FCM	7.8	40	40.5	11.7
csi-FCM	7.9	49.7	36.0	6.4
FMLE	7.4	79.8	12.1	0.7

Table 4.4: *Average percentage of the pixels per class after clustering the entire multivariate minced meat image with FCM, csi-FCM and FMLE.*

The FMLE cannot successfully segment the image without data preprocessing. Certain pixels of the fat class in the image are over-illuminated and must be removed before clustering. Without the removal of the over-illuminated pixels the FMLE becomes unstable and fails to converge. Figure 4.7(e) shows the image segmented with FMLE after the removal of the over-illuminated pixels. The classes fat and dark meat are recognizable, but the light meat class is merged with the dark meat class and the fat pixels are classified as light meat class. Few pixels, merely 0.7% according to table 4.4, are classified as fat by FMLE (not visible in the subimage). The FMLE underestimates the fat class and and overestimates the dark meat class. Because the true class of the pixels is unknown, a product expert evaluated the segmented images. The expert considers the fat class as overestimated in the FCM segmented image, whereas the csi-FCM segmented image is considered to be more in resemblance with the original image.

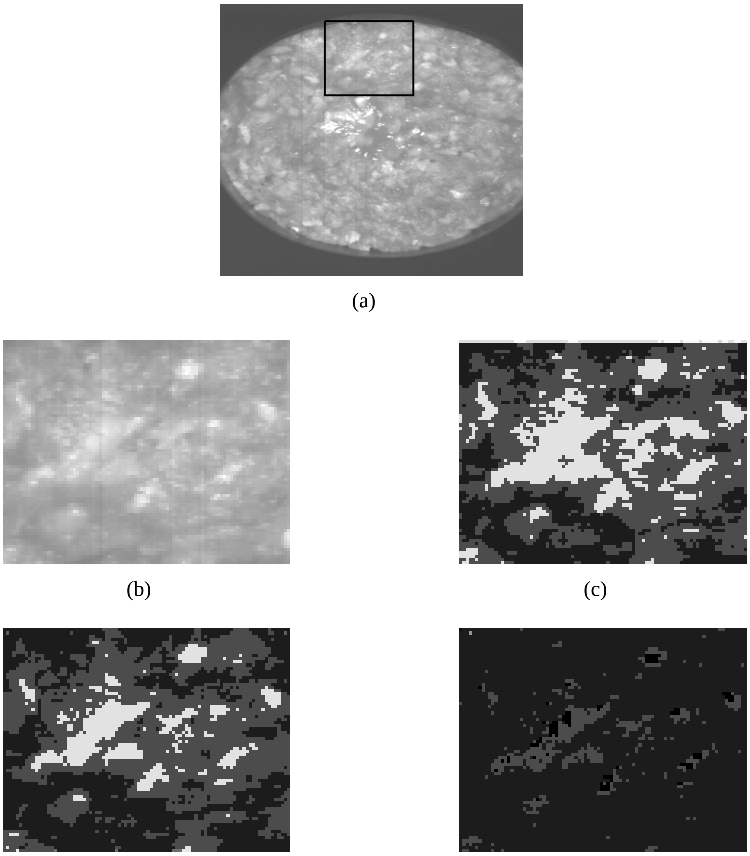

(a)

(b)

(c)

(d)

(e)

Figure 4.7: *Segmenting a multivariate image of minced meat with FCM, csi-FCM and FMLE. (a) Original meat image; (b) Subimage of minced meat; (c) Results of clustering with FCM; (d) Results of clustering with csi-FCM; (e) Results of clustering with FMLE.*

4.4 Conclusions

A modification of FCM to overcome the sensitivity of FCM for unequal cluster sizes in multivariate images is presented in this paper. The csi-FCM algorithm uses a modified version of FCM to reduce the influence of objects of larger clusters. Objects of larger clusters receive lower condition values in order to reduce their contribution to the position of small cluster centers. Between subsequent FCM iterations, the a-priori class probability is calculated and this probability determines the condition value for each object. This makes csi-FCM unsupervised in its calculation of the condition value. Besides the required number of clusters no additional parameter settings are required.

Experiments with numerical datasets with unequal number of points per class show that csi-FCM detects the classes correctly, in contrast with FCM. The sensitivity experiment shows that csi-FCM is less sensitive for good cluster prototype initialization values compared to FMLE. The use of csi-FCM for the segmentation of multivariate images clearly shows improvement compared with FCM in case of hyper-spherical shaped clusters with unequal number of points. Classes that remain undetected or incorrectly estimated by FCM or FMLE are correctly detected by csi-FCM.

4.5 Acknowledgements

This work was partially funded by the Dutch Ministry of Economic Affairs under the IOP (Innovation Oriented Research) programme and the Ministry of Agriculture, Nature Management and Fisheries.

Bibliography

[1] J. Noordam, G. Otten, A. Timmermans, and B. van Zwol, “High-speed potato grading and quality inspection based on a color vision system,” in *SPIE, Machine Vision and its Applications* (K. W. Tobin, ed.), vol. 3966, (San Jose, Californie), pp. 206–220, SPIE, 2000.

[2] J. Bezdek, L. Hall, and L. Clarke, “Review of MR image segmentation techniques using pattern recognition,” *Medical Physics*, vol. 20, no. 4, pp. 1033–1048, 1993.

[3] A. M. Bensaid, L. O. Hall, J. Bezdek, and L. Clarke, “Partially supervised clustering for image segmentation,” *Pattern Recognition*, vol. 29, no. 5, pp. 859–871, 1996.

[4] A. Baraldi and P. Blonda, “A survey of fuzzy clustering algorithms for pattern recognition - part 2,” *IEEE Transactions on Systems, Man and Cybernetics*, vol. 29, no. 6, pp. 786–801, 1999.

[5] M. Yang, “A survey of fuzzy clustering,” *Mathematical and Computer Modelling*, vol. 18, no. 11, pp. 1–16, 1993.

[6] A. M. Bensaid, *Improved fuzzy clustering for pattern recognition with applications to image segmentation*. PhD thesis, South Florida, 1994.

[7] L. Hall, A. M. Bensaid, L. Clarke, R. P. Velthuizen, M. S. Silbiger, and J. Bezdek, “A comparison of neural network and fuzzy clustering techniques in segmenting magnetic resonance images of the brain,” *IEEE Transactions on Neural Networks*, vol. 3, no. 5, pp. 672–682, 1992.

[8] J. Noordam and W. van den Broek, “Multivariate image segmentation based on geometrically guided fuzzy c-means clustering,” *Journal of Chemometrics*, vol. 16, no. 1, pp. 1–11, 2002.

[9] F. Behloul, B. Lelieveldt, A. Boudraa, and J. Reiber, “Optimal design of radial basis function neural networks for fuzzy-rule extraction in high dimensional data,” *Pattern Recognition*, vol. 35, no. 3, pp. 659–675, 2002.

[10] C. Wong, C. Chen, and S. Su, “A novel algorithm for data clustering,” *Pattern Recognition*, vol. 34, pp. 425–442, 2001.

[11] J. Bezdek, *Pattern Recognition with Fuzzy Objective Functions*. New York: Plenum Press, 1981.

[12] J. Bezdek, “Cluster validity with fuzzy sets,” *Journal of Cybernetics*, vol. 3, no. 3, pp. 58–73, 1974.

[13] I. Gath and A. Geva, “Unsupervised optimal fuzzy clustering,” *IEEE Transactions on Pattern Analysis and Machine Intelligence*, vol. 11, no. 7, pp. 773–781, 1989.

[14] J. Hoffbeck and D. Landgrebe, “Covariance matrix estimation and classification with limited training data,” *IEEE Transactions on Patern Analysis and Machine Intelligence*, vol. 18, no. 7, pp. 763–767, 1996.

[15] W. Pedrycz, “Conditional Fuzzy C-Means,” *Pattern Recognition Letters*, vol. 17, pp. 625–631, 1996.

[16] G. Polder, G. van der Heijden, and I. Young, “Spectral image analysis for measuring ripeness of tomatoes,” *Proceedings of the Annual Meeting of the ASAE*, vol. 00308, pp. 1–14, 2002.

Chapter 5

A new strategy for the modelling and representation of classes in multivariate images

Abstract

This paper describes a new procedure for the estimation of classes in multivariate images. The Feedback Multivariate Model Selection (FEMOS) procedure combines unsupervised and supervised classifiers with a model evaluation criterion to extract classes from the multivariate image in an iterative manner. The procedure uses a subset of the multivariate image to estimate a general model and evaluates this model with the original multivariate image via a model evaluation criterion. The FEMOS procedure can be applied for the unsupervised segmentation of multivariate images or for training and test set estimation from multivariate images. Furthermore, a new coloring scheme, called class coloring, is presented for coloring of class labels in segmented images. The coloring of class labels is automated which makes it independent of the number of classes and shows more resemblance with the pseudocolor multivariate image. The FEMOS procedure is tested on different real world multivariate images and the results are compared with csi-FCM, a clustering algorithm. The results show that the FEMOS procedure outperforms traditional routines in terms robustness and accuracy when applied as either unsupervised segmentation technique or class modelling technique.

5.1 Introduction

With the availability of multispectral camera's which operate in the visible or near infrared region of the electromagnetic spectrum new application areas become available in which both spatial information and spectral resolution can be used. The development and applications of such multispectral imaging systems has been reported for the quality inspection of poultry [1, 2] and chickens [3], measurement of ripeness of tomatoes [4], quality inspection of citrus fruits [5], inspection of cherries [6], spatial distribution of soluble solids in kiwi fruit and melons [7, 8] and detection of parasites in cod fillets [9]. In the above inspection applications, the goal was to detect small defects or abnormalities in the object under inspection with multispectral imaging. To quantify the amount of defects or abnormalities in the inspected object classification of the spectra is required.

For the classification of multispectral images several supervised and unsupervised techniques are available which are thoroughly described in literature [10]. The unsupervised techniques are able to partition the image in regions based on a user selected number of classes but the huge amount of data in multispectral images requires computational demands which are not feasible in most applications. A widely used approach is to apply an unsupervised classifier to a small sample of the image data for the estimation of the classes and then classify the entire multivariate image using a supervised classifier trained with the estimated model [11]. It has been shown that this strategy leads to under or overestimated classes in the segmented image [12]. Furthermore, different samplings may result in different segmentation results due to the random nature of the sampling procedure. The supervised techniques require a labelled training set from which the class boundaries are determined. Usually, a representative training must be obtained from the multispectral image set which can be a challenging task as there are multiple image bands to explore. A procedure for selecting a representative training set and test set from multivariate images is based on multivariate image analysis (MIA), as described thoroughly in literature [13]. MIA uses Principal Component Analysis (PCA) for dimension reduction and with three selected score images a pseudo color image is constructed which is used for visualization and region selection. This procedure has been followed in several applications [9, 14] for the selection of training and test sets. The use of PCA as a dimension compression technique has the advantage that the majority of the variance is presented by the first few principal components (pc). This reduces the exploration time as only the first few pc plots and score images have to be explored. However, it is well known that variation does not always correspond with the embedded information and thus transforming the data may not visualize all the information [15]. In these cases, exploring the original data is preferred which, of course, can also be carried out with the MIA procedure. However, the exploration becomes more difficult and time consuming because the information is spread over the full dimension of the data.

A characteristic feature of the MIA procedure is the possibility of a rough explorative analysis of the multivariate image as regions in both the spatial and spectral domain can be explored and visualized quickly. However, to select a training set from the multivariate image with the MIA procedure, an exact selection of regions is required which can be a challenging task. Pixels between two or more classes, the so called mixed pixels, make the selection of a single class difficult. If a selection is made too wide, the mixed pixels are included in the model and much misclassification will occur. If the regions are made too narrow, correct classification will occur but with a remainder of mixed pixels. In case of class overlap, quite a number of pixels are in classes which are difficult to define. In case of overlapping classes or very dense score plots the authors suggest the use of local models in which only a part of the image is explored [13]. However, a disadvantage of local models is that larger objects may remain undetected because only part of them is shown in each local image [13].

Other difficulties are the accuracy and the robustness of the MIA procedure. It is not possible to verify that that all relevant classes have been selected, due to dense classes, class overlap or mixed pixels small classes may be overlooked and therefore will not be included in a training set. To prevent this, a thoroughly time consuming course to fine exploration of the multivariate image is required. As the user selects regions for training set extraction, the robustness of a training set cannot be guaranteed. Although one can state that the MIA procedure is an attractive method for global exploration, it is time consuming for training set selection and requires a lot of user experience.

Still, the MIA procedure inherently contains a very important evaluation characteristic as the user can immediately evaluate the quality of a selected region. The continuously switching between the spatial and spectral domain gives the user a visual feedback about the quality of the selected region and the user can adjust the selection if necessary. In this paper a heuristic procedure called Feedback Multivariate Model Selection (FEMOS) is presented in which this so-called visual feedback is automated. Classes are estimated from the multivariate image, the classes are used to segment the entire image and the quality of the segmented image is evaluated via a model evaluation criterion which compares the segmented image with the original multivariate image. The output of the model evaluation criterion serves as a measure of fit between the current model and the multivariate image and can be considered as the essential core of the procedure. The outcome of the model evaluation criterion is used to minimize the difference between the original image and the segmented image by updating the used model in an iterative loop until a stop criterion is fulfilled.

As the FEMOS procedure is a general procedure for the modelling of classes it is not dependent on a particular classification technique or image type which makes it widely applicable. The goal of the presented work is to present a general procedure to estimate the available classes in a multivariate image without attempting to present a new clustering routine or to estimate the exact number of classes. The paper is organized as follows: Section 5.2 discusses the rationale of the FEMOS procedure. Section 5.3 shows the results of experiments with different real world multispectral images. In the last section, the conclusions are given.

5.2 Theory

5.2.1 Rationale of Feedback Multivariate Model Selection

The Feedback Multivariate Model Selection (FEMOS) procedure is a training set estimation procedure for multivariate images where the visual feedback principle as described in the previous paragraph is implemented through a model evaluation criterion that compares the segmented image with the original image. This model evaluation criterion, which is at the heart of the FEMOS procedure, guides a model estimator based on the difference between the original and the segmented image. The principle of FEMOS is depicted in figure 5.1. The procedure starts with an initialization step in which an initial class model of the image is created via a sampled subset. This initial model is updated in an iterative loop in which the number of classes increases after each run until a stop criterion is fulfilled.

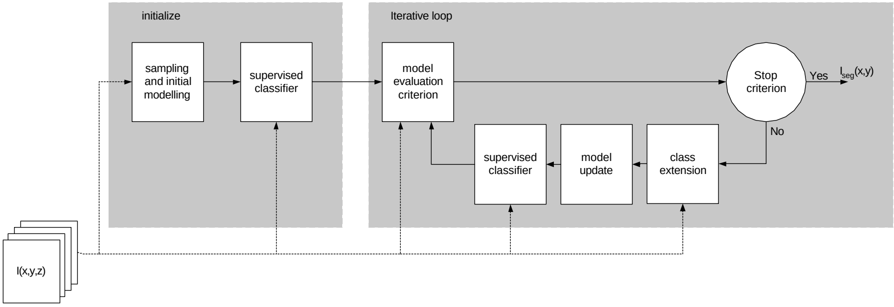

Figure 5.1: *The principle of Feedback Multivariate Model Selection.*

5.2.2 Principle in detail

The initialization step consists of a sample and initial modelling stage and a supervised classifier. In the sample and initial modelling stage, a subset of pixels is taken from the multivariate image via stratified random selection. In stratified random sampling, the image is divided into squares and in each square a number of randomly located pixels are taken. With this subset, an initial two class model is estimated by an unsupervised classifier. The output of this sample and initial modelling stage is called a general model and consist of the centroid and covariance matrix for each class. With this general model, a supervised classifier is trained in the next stage and the entire image is classified with the supervised classifier. The result of the initialization stage is a segmented image with two classes and a corresponding general model consisting of a centroid and a covariance matrix for both classes.

With this general model and the corresponding segmented image, the model evaluation criterion is evaluated. The model evaluation criterion evaluates all classes of the segmented image with a predefined criterion. Usually, a similarity criterion is selected which assumes that the image consists of homogeneous classes. The class which gives the worst criterion performance is labelled as the candidate class and will be further explored in subsequent class extension stage if the stopcriterion is not fulfilled.

In the class extension stage, a two-class unsupervised classification is performed on a subset of pixels from the segmented image which are labelled with the candidate class label. The subset is obtained again via stratified random sampling. The underlying idea is that the bad performance of the candidate class is due to the fact that this class contains two or more classes. The outcome of the class extension stage is an estimated two class model consisting of a centroid and a covariance matrices for the two classes. The cluster size insensitive FCM (csi-FCM) is used here as unsupervised classifier in order to overcome the sensitivity of FCM for clusters which have an unequal number of points [16].

In the model update stage, the original centroid and covariance matrix of the candidate class in the general model are replaced by the two new centroids and covariance matrices of the class extension stage. Now, the general model has been refined as the number of classes have increased by one. The data that represents the new refined general model is clustered by the unsupervised classifier to rearrange the complete general model.

In the last stage of the feedback loop a supervised classifier is trained with the updated general model and the entire multivariate image is classified. The linear discriminant analysis (LDA) is used here as supervised classifer[10]. In the next run, a new iteration is carried out in which the updated general model and the segmented image are evaluated by the model evaluation criterion again. When the procedure stops, the resulting estimated general model contains a centroid and a covariance matrix for each individual class.

5.2.3 Model evaluation criterion

As mentioned in the previous paragraph, different criteria can serve as model evaluation criterion that must relate with the available information in the image. Usually, homogeneous regions are assumed and two criteria will be discussed in this paragraph which can be applied. First, variance is considered as criterion for homogeneous regions. The variance (VAR) within class i can be calculated via:

$$VAR_i = \frac{1}{N_i} \sum_{j=1}^{N_i} ((\mathbf{I}(x,y,\lambda)\ \&\&\ I_i(x,y)) - \mathbf{v}_i)^2 \tag{5.1}$$

where i is the current class, N_i is the number of pixels in the segmented image with label i, $\mathbf{I}(x,y,\lambda)$ is the original 3-dimensional multivariate image composed of a number of images $I(x,y)$ recorded at different wavelengths (λ), $I_i(x,y)$ is the image containing only pixels of class i, and $\mathbf{v}_i$ is the centroid of class i from the general model. The first part of the equation is a masking operation (&&) where all pixels classified to class i are extracted from the original image. Then, the variance between these pixels and the centroid $\mathbf{v}_i$ from the general model is calculated. If there are more classes covered within the current class i, the variance will increase and the class is a candidate for further exploration. This equation implicitly holds the principle of visual feedback as it relates the segmented image $(I_i(x,y))$ with the estimated centroid $\mathbf{v}_i$ of the general model.

Another model evaluation criterion which also includes the covariance matrix of the estimated class is the average mahalanobis distance (AM_i) between the pixels assigned to class i and the centroid of class i:

$$\begin{aligned} AM_i &= \tfrac{1}{N_i}\textstyle\sum_{j=1}^{N_i} \quad ((\mathbf{I}(x,y,\lambda)\ \&\&\ I_i(x,y) - \mathbf{v}_i)^T \mathbf{Cov_i^{-1}} \\ &\qquad\qquad (I(x,y,\lambda)\ \&\&\ I_i(x,y) - \mathbf{v}_i))^2 \end{aligned} \tag{5.2}$$

where AM_i is the averaged mahalanobis distance, i is the current class, N_i is the number of pixels in the segmented image with label i, $\mathbf{I}(x,y,\lambda)$ is the original 3-dimensional multivariate image composed of a number of images $I(x,y)$ recorded at different wavelengths (λ), $I_i(x,y)$ is the segmented image containing only pixels of class i, $\mathbf{v}_i$ and $\mathbf{Cov}_i^{-1}$ are respectively the centroid of class i and the inverse covariance matrix of class i from the general model. In general, other evaluation criteria are possible as long as the criterion describes the difference between class i from a general model and the pixels assigned to that class i in the segmented image. In multivariate images with homogeneous regions with no or little variance, the calculation of a covariance matrix and its inverse can be a burden. In that case the variance criterion may be used as it solely based on the variance in each class and thus easy to calculate. Also, the use of the euclidian distance instead of the mahalanobis distance in both unsupervised and supervised classifiers is preferred with these type of images.

5.2.4 Stop criterion

A stop criterion is required to end the iteration loop of the FEMOS procedure. As the FEMOS procedure uses an unsupervised classification technique to estimate a model for the multivariate image it is possible to use one of the many cluster validation techniques (e.g. Partition Density for FCM [17]) which is related to the used unsupervised classification technique. A cluster validation technique tries to estimate the number of classes by calculating a criterion for a range of number of classes. The number of classes which correspond to a maximum or minimum value for this criterion (this is validation technique dependent) is assumed to be the correct number of classes. However, the large number of published cluster validation techniques already indicate that there is no single technique which performs well for different images. Experiments with different cluster validation techniques have confirmed this [17]. Therefore, a stop criterion is developed which is based on the particular model evaluation criterion (see equation 5.1) used instead. An advantage of such a criterion is that it is independent of the used unsupervised clustering technique, in contrast with general cluster validation techniques. In case of the variance criteria, the stop criterion is based on the scaled variance (SVAR) for all available classes:

$$SVAR_i = \frac{1}{\sum_{j=1}^{c} VAR_i} VAR_i \qquad \forall\, i = 1..c \tag{5.3}$$

where c is the number of classes and VAR_i is the calculated variance in class i, according to equation 5.1. The scaling limits the range for VAR_i between $0-1$, where lower values of VAR_i result in a more precise model. A threshold value is set by the user that defines the stop criterion, the procedure stops if the value of $SVAR_i$ is below the threshold value. The FEMOS procedure is implemented in a stand alone application and extensive experiments with different type of images have shown that the threshold value is less image dependent then user dependent. A threshold value of 0.25 gives good results for different type of images, as will be shown in the experiments.

5.2.5 Visualization and coloring of images and graphs

Multivariate image as pseudo color image

In order to visualize the multispectral image for the user a pseudo color image has to be created. In the MIA procedure, three score images are selected to form a pseudo color image. However, if no PCA is performed, score images are not available and three variables from the original image must be selected to represent these as Red, Green and Blue. A drawback of this method is that only three variables at a time can be shown at once. Finding out which components to choose and how to combine them may lead to testing many combinations. A faster and very simple procedure to create a pseudo color image from a raw N-dimensional multivariate image is to distribute the N variables over the three color bands Red, Green and Blue of the color image. The distribution of the N variables over the three color bands can be done equally or according to a specific function, like the function that describes the color sensitivity of the human eye. For each color band, the assigned variables are averaged and scaled to the dynamic range of the color band, usually between 0 and 255. The advantage of this procedure is that no variable selection is required and that all the variables are included in the pseudo color image.

Coloring of segmented images and graphs

A common method to visualize the segmented image is to represent the segmented pixels with a color that corresponds with a predefined label. This way of labelling can give good contrast but the colors for the labels must be assigned beforehand. Another method which shows more visual resemblance with the original (pseudo color) image is to use the centroid of the class as color for the label instead. This method is called class coloring. In case of a multivariate image with N variables, the N-dimensional centroid must be reduced to a 3-dimensional pseudo centroid. This dimension reduction can be determined in either a similar way as described in paragraph 5.2.5 or according to a user defined function. The result is that both the multivariate image and the segmented image are represented as pseudo color images which share the same color mapping, which makes them easy to compare.

The same coloring procedure can be used for the visualization of data, centroids and covariance matrices in graphs. During a clustering process or after training a supervised classifier, the original image, the segmented image and the corresponding class information can all be visualized in similar colorings.

The major advantage of class coloring is that it is independent of the number of classes in the segmented image. Traditionally, if an extra class is required to describe the data, a new label is created with a corresponding assigned color for the segmented image. With the presented class coloring method, a label color is automatically created as is just the (pseudo color) centroid of the new class. In the section 5.3.2 and 5.3.3 the multispectral images are displayed according to the class coloring method.

5.2.6 Combing spatial and spectral information

The model evaluation criteria as described in paragraph 5.2.3 is based on spectral information only. The mutual spatial relationship between pixels or the position of pixels in the image is not exploited by the evaluation criterion yet. Noise, outliers and mixed pixels in the image may influence the estimation of the general model as they contribute heavily on the output of the model evaluation, as shown in equation 5.1. As a result of this, the class containing these spurious pixels will have the worst performance and is abusively marked as the candidate class for sub class exploration. It is advisable that these type of pixels are removed from the set if this information is available. The evaluation criteria can easily be extended so that spatial information can be used during the model estimation procedure. Equation 5.1 is extended with a spatial filter operation according to:

$$VAR_i = \frac{1}{N_i} \sum_{j=1}^{N_i} \left((\mathbf{I}(x,y,\lambda) \ \&\& \ \mathscr{F}_s(I_i(x,y))) - \mathbf{v}_i \right)^2 \tag{5.4}$$

where i is the current class, N_i is the number of pixels in the segmented image with label i, $\mathscr{F}_s$ is the spatial filter operation, $\mathbf{I}(x,y,\lambda)$ is the original 3-dimensional multivariate image composed of a number of images $I(x,y)$ recorded at different wavelengths (λ), $I_i(x,y)$ is the image containing only pixels of class i, and $\mathbf{v}_i$ is the centroid of class i from the general model. The spatial filtering is applied on pixels with label i in the segmented image before the calculation of the summed variance is performed. To perform the spatial filtering in practice, all corresponding pixels with label i are transformed to a 2D image (spatial domain) and the spatial filter operation is applied to this image. After the filtering operation, the remaining pixels are backtransformed to spectral domain and the model evaluation criterion is applied to the remaining pixels of class i. The effect of this ordering is that noise or outliers have no effect on the model estimation process. The type of spatial filter applied depends on the spatial structure of the image. Choosing an appropriate filter is application depended and no general rule for selecting a particular filter for a specific image type can be given. E.g., typical structures in an image are formed by edge pixels which are positioned on a transition between regions in the image. After applying a window operation like a binary morphological open operation [18], which is a combined morphological erode-dilate operation, edges of single pixels are removed and remaining blobs and structures are preserved. The averaged mahalanobis criterion (equation 5.2) can be extend with the spatial filter in the same way.

5.2.7 Implementation issues

As described in the previous paragraphs, the FEMOS procedure takes a subset of the image via stratified random sampling. The size of the subset is a user adjustable parameter, although this parameter has a lower bound. The lower bound of this parameter is determined by the dimension of the data and the used classification techniques. In case of linear decision boundaries, the required number of points in each class is linear related with the dimension of the data, with quadratic classifiers, this relation becomes quadratic [19]. There is no upper bound for the sampling size, using more points only effects the speed of the procedure.

5.3 Experiments

Experiments with different type of multivariate images have been performed in which the performance of FEMOS is evaluated for its segmentation performance for different applications. In the first experiment, a multispectral image of wood is explored which has been described in literature [20]. The image is explored with both the MIA procedure and the FEMOS procedure and the segmentation results are compared. Another application of FEMOS will be shown in the second example where an multispectral French fries image is segmented in regions containing several defects and diseases. Although some of these defects and disease are visible for the human eye, multispectral imaging is required to detect defects which appear invisible for the human observer. The example will show that FEMOS will be able to estimate all the relevant classes from the multispectral image, including the for human invisible latent defects. In the third experiment, the performance of FEMOS procedure is evaluated when applied as a clustering technique. A color image of a African violet plant is segmented by both FEMOS and csi-FCM. The flower in the image contains yellow pistils which are difficult to segment and label in a single class as the small pistils in the flowers form classes with very few points.

5.3.1 Instrumental

The color images used in the experiments are captured by a Sony 3-CCD colour camera. A prism in the camera splits the incoming light of the visible spectrum into a Red, Green and Blue part and the light is mapped on the corresponding CCD. A framegrabber in the computer digitizes the 3 images and delivers 3 different 8-bit gray-value images, which result in a multivariate colour image with 3 variables (Red,Green and Blue). To obtain homogeneous lighting on the camera's field of view, a special lighting chamber with high-frequency fluorescent tubes (6500K) was used.

Figure 5.2 depicts the multispectral imaging measurement setup which is used for the acquisition of multispectral French fries images. The multispectral French fries images are recorded with an ImSpector V9 imaging spectrograph (Spectral Imaging Ltd. Oulu, Finland) mounted on a Peltier cooled Qimaging PMI-1400EC (Burnaby, Canada) monochrome camera. The camera contains a Kodak KAF-1400EC class II CCD sensor (Eastman Kodak, Rochester,USA). The ImSpector V9 produces a multispectral image where the 430-900 nm part of the electromagnetic spectrum is recorded in 104 small bands (every 4.5 nm) for every pixel. The incoming light is split by a prism-grating-prism and projected on the 2 dimensional CCD in the camera. The CCD size is 1320 pixels along the spatial axis and 1035 pixels along the spectral axis of the system. Since the number of pixels in the spectral direction is larger than the number of distinguishable wavelength bands according to the specifications the pixels can be binned with a factor 9 ($1035/104 \approx 9$). A 2-dimensional spectral image is obtained by moving the object under the ImSpector during recording. The translation table used to move the fries with respect to the camera is a Lineartechniek Lt1-SP5-C8-600 translation table driven by a SDHWA 120 programable microstepping motor driver (Ever Elettronica, Italy). The stepsize of the translation table was chosen to

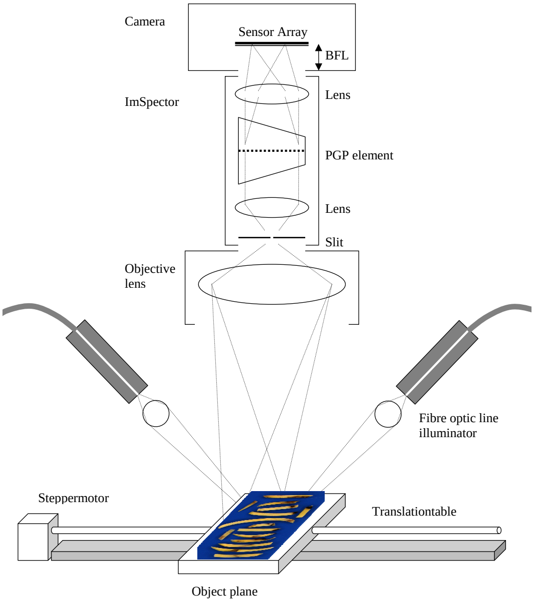

Figure 5.2: *An overview of the multispectral imaging setup.*

match the spatial resolution of the spatial axis. The number of steps was chosen to capture the entire plate with French fries. The resulting images have a spatial resolution of 318 × 560 square pixels and a spectral dimension of 104 bands (about 100 MB) The used lighting setup consists of two Dolan-Jenner PL900 illuminators (Andover St. Lawrence, Mass.) with 150 W quartz halogen lamps. The scene was illuminated by two glass fiber optic line arrays (Vision Light Tech) of 0.002 inch × 6 inch aperture. Two Rod lenses were positioned in front of the line arrays. Detailed information about the used multispectral imaging setup and the spectral calibration is described in literature [21].

5.3.2 Experiment with a multispectral image of pine and spruce wood

In this experiment, a 7 band multispectral image (680,740,800,840,1010,1110 nm) is explored with the FEMOS procedure. The image is recorded with a PbS camera and a filter wheel (detailed information of the measurement setup can be found literature [22]). The image consists of two wooden disks and a pseudo color image is shown figure 5.3(a). The upper disk in the image is cut from a spruce tree (with a crack), the lower disk in the image is cut from a pine tree and both disks contain several rings of wood and bark. The multispectral image is previously explored with the MIA procedure [20] and the corresponding score plot is shown in figure 5.3(b). The goal of the original work was to investigate if three specific spatial regions in both disks contain the same chemical information. The spatial regions are the two types of wood in the center region (dead xylem and a thin outer layer of living xylem), two types of bark (dead floem and a thin layer of living floem) and the thin layer under the bark (living xyelem). The (non selected) upper left cluster in the score plot corresponds with the background class and is ignored in the analysis. The three clusters visible in the lower right corner of the score plot are selected according to the MIA method and are backprojected in a single combined score image of figure 5.3(c). This MIA score image shows corresponding regions in both disks, the center heart of the upper disk (compression wood) is shown as a ring in the lower disk (living xylem) and also the bark wood of both disks shows spectral spectral resemblance.

The result of the FEMOS procedure with the default setting of 0.25 for the stop criterion is shown in figure 5.3(d). By using the variance criterion the similarity based segmented image reveals more detailed information about the outer and internal regions of the wood compared with the MIA analysis. Both disks reveal additional rings below the bark wood which are visible in the other disk, either as additional bark wood rings or as regions in the internal heart. Furthermore, the FEMOS segmented image shows that the physical-chemical composition of the center part of the

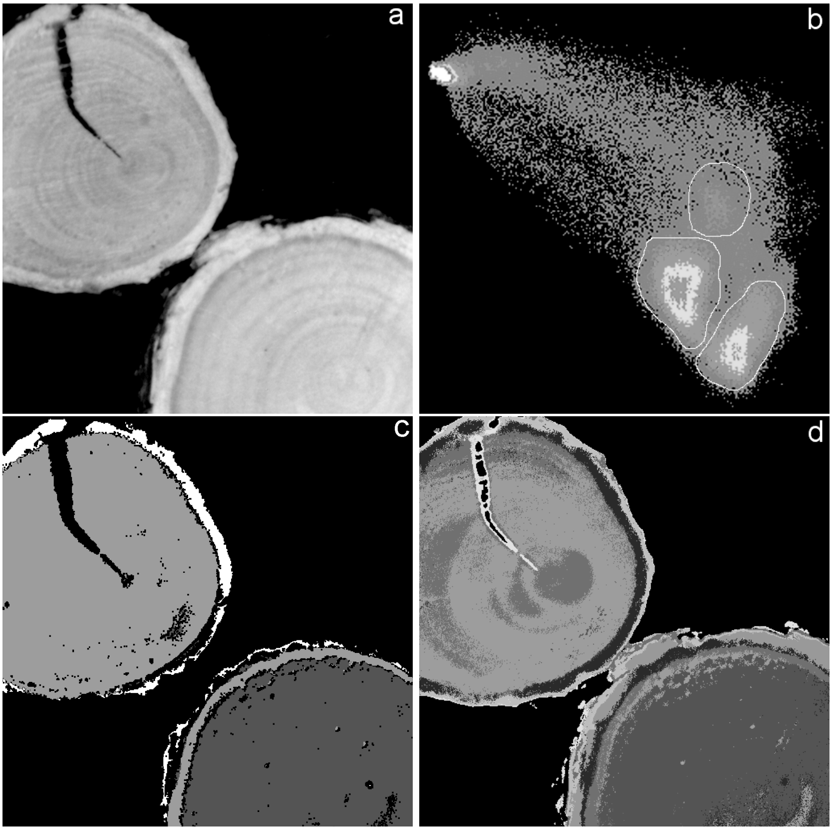

Figure 5.3: *A multispectral image of wood. (a) The pseudo-color image; (b) Score plot; (c) MIA combined score image; (d) The FEMOS 9-class segmented image.*

upper disk is not homogeneous, parts in the center of the upper pine disk are spectrally similar to some of the bark wood rings of the spruce disk. This is not visible in the MIA segmented images, due to mixed pixels and the small number of pixels in these regions these regions are not visible as individual clusters in the score plot with any combination of the PC's which makes the reproduction of the FEMOS segmented image with MIA analysis a challenging task. This example shows the superior value of the FEMOS procedure where just a single run reveals detailed information of present classes in the multispectral wood image.

5.3.3 Latent defect detection in multispectral French fries image

In a recently presented research [23] both RGB color and multispectral images taken from fries from different cultivars are classified for the inspection of defects and diseases. In this paper the feasibility is investigated to improve discrimination between potato skin and potato defects and diseases on French fries with multispectral imaging, in comparison with color imaging. A product expert labelled all visible defects before the image acquisition. In this research MIA was applied for the exploration of the multivariate images and training and test sets were extracted from the images. The multispectral French fries images are recorded with the multivariate imaging setup as described in paragraph 5.3.1. The image are preprocessed according to a procedure which is thoroughly described in literature [23]. Besides defects like internal and external rot, peel, external damaging and internal browning, some of the fries contain the defect greening. Potatoes turn green on a cumulative exposure to light as a result of the formation of chlorophyll. Such tubers develop a bitter taste, off -flavor and cause health hazards and, in some specific instances, death because of high solanine content [24, 25, 26]. The concern with green potatoes is not the chlorophyll, which is tasteless and harmless, but the solanine which develops in the the same area along with the chlorophyll. Therefore, green potatoes must be removed as these components affect the quality of potatoes and potato products, especially in respect to appearance, texture and nutritive value. Heavily greening is visible for the human eye and thus detection with standard RGB color cameras is sufficient. An extensive multispectral analysis of the multivariate images showed that a number of fries showed similar spectra as the fries with greening although the product expert did not label these fries as greening. In fact, the product expert labelled these fries as good fries. Figure 5.4 shows the original color image taken with the RGB color camera. The fry in the upper part of the image is marked with number one, the fry in the lower part of the image is marked number two. Fry number one was labelled as good fry, fry number two was labelled as greening. On both fries, a circular marker indicates the location of the spectral point analysis. These spectra including the second derivatives of these spectra are shown in the graphs of respectively figure 5.4(b) and figure 5.4(c). Both spectra in the graph with the second derivative show a peak in the 670-680 nm region, a region which is known to be the absorbtion wavelength of chlorophyll-a. The extra shoulder in the spectra of marker 2 at 650 nm is owing to chlorophyll-b, as both chlorophylls are present in green potatoes[24]. Therefore, the fry with marker one is considered to contain some greening, though invisible for the human eye. This image represents a type of problems in multivariate images where the modelling of (latent) classes can be troublesome with MIA as only a thorough time consuming exploration might detect all classes. The MIA analysis of this image

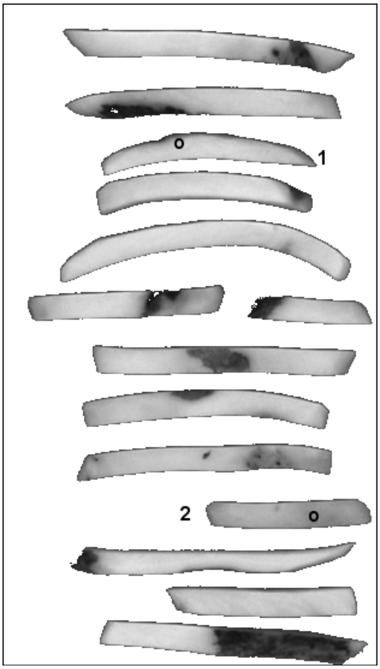

(a) The original RGB image

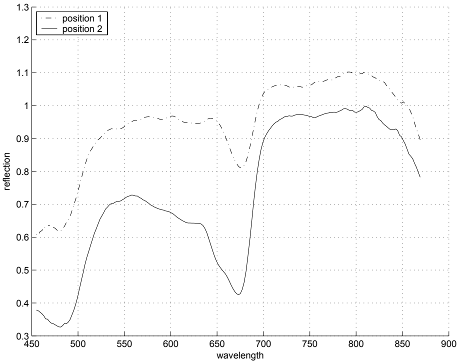

(b) The original spectra

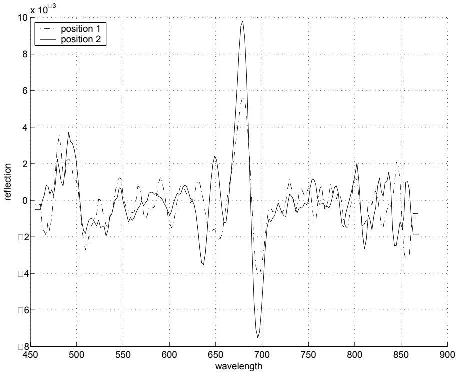

(c) The 2nd derivative of the spectra

Figure 5.4: *Original RGB color image and both original and 2nd derivative spectra for marked positions on fry 1 and 2.*

showed that the invisible greening was only visible in PC-8 and required the use of local models.

In images with these type of problems, the FEMOS procedure is a good alternative for the detection of all available classes. Therefore, the French fries image is processed with the FEMOS procedure to investigate if the FEMOS procedure is able to extract all classes from the image, including the invisible greening class. Figure 5.5 shows the result of the FEMOS procedure where the multivariate image is segmented. The variance model evaluation criterion is used with a stop criterion threshold set to 0.25. According to the labels assigned by the product expert, the FEMOS procedure correctly segmented the image in the classes peel, good flesh, external damaging and greening. Is it shown in the image that the fries marked as one and two in figure 5.5 are assigned to the same greening label. Besides the two marked fries, more regions in the image received the greening label. The inspected spectra of those regions indeed showed convincing correspondence with the spectra as shown in the figures 5.4(b) and 5.4(c). This example shows the surplus value of FEMOS procedure as a general

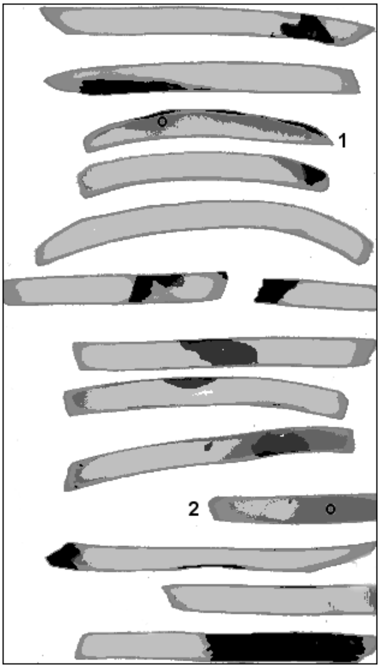

Figure 5.5: *The FEMOS segmented image.*

class extraction technique for multivariate image containing different classes. In a single run of the FEMOS procedure the segmented image showed all available classes, whereas the MIA exploration and model extraction is time consuming and does not guarantee all available classes are extracted. This makes the FEMOS procedure more accurate than the MIA approach for the extraction and modelling of classes.

5.3.4 Clustering with FEMOS procedure

In this experiment, the FEMOS procedure is applied as an unsupervised clustering technique to show the ability of FEMOS as a general class estimation technique compared to csi-FCM. The focus of the experiment is on the robust and accurate representation of all available information, a criterion which easily can be examined by a visual comparison between the original and the segmented image. Therefore, a 3-variable spectral color image (RGB) of a known object is used. The used RGB image is an African Violet plant (Saintpaulia Ionantha Wendl) and the original RGB color image is shown in figure 5.6. The image contains five classes: background white, black soil, purple flower with yellow heart and green leaves. Although the yellow hearts in the purple flower color have a bright color, the hearts are difficult to segment in a single class owing to the small number of yellow pixels. The saturated white background is removed from the image via a image threshold operation (254,254,254). There remains some background around and between the leaves due to shadows. The image is segmented by csi-FCM and the FEMOS procedure. For csi-FCM, the examined number of classes range from 5 till 14 and for each number of classes the experiment is repeated 5 times to reduce initialization influences. In csi-FCM, the mahalanobis distance is used as distance criterion, the fuzziness parameter m=2 and the stopcriterion $\varepsilon = 0.000001$. Five runs with FEMOS and variance criterion are performed. The stopcriterion for the FEMOS procedure is set to 0.25. Figure 5.6 shows the graphs with the covariance and centroids (only the Red (R) and Green (G) variables are shown in the graphs) and the csi-FCM 13 class segmented image of the African violet plant. In all csi-FCM segmented images the yellow flower heart class is completely missed. The increase in classes from 5 till 14 has only resulted in an oversegmented green leave class (7 classes) and an oversegmented blue flower class (5). In all 45 csi-FCM segmented images the yellow flower heart class is merged with the white background class. This is also visible in the 13 class graph of figure 5.6 where an abundance of covariance matrices is located in the lower left corner, representing a number of dark colored classes green leaves ($R \approx 60-100; G \approx 60-100$) and purple flowers ($R \approx 30-40; G \approx 50-80$). In the upper right corner of the 13 class graph, a single white background class ($R = 244; G = 247$) and a gray background class($R = 174; G = 183$) is visible. In the 5 class graph, two green leave classes ($R = 61,102; G = 66,99$), two purple flower classes

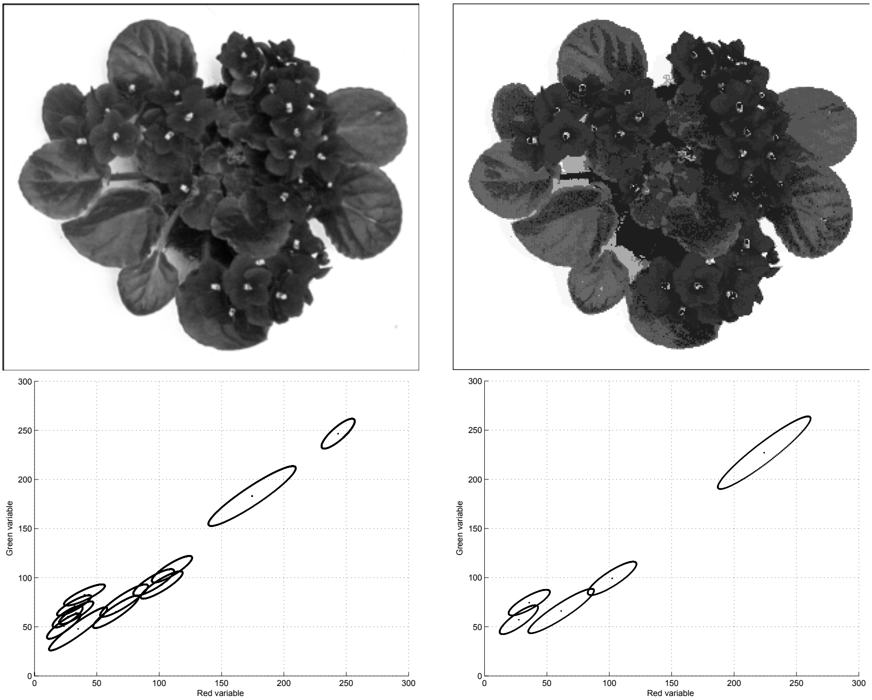

Figure 5.6: *The original RGB color African Violet (upper left), the 13 class csi-FCM segmented image (upper right), the centroids and covariance matrices graphs of the 13 class model (lower left) and the 5 class model (lower right).*

($R = 28 - 36; G = 57 - 75$) and a single white background class ($R = 244; G = 227$) is visible. In the FEMOS segmented image as shown in figure 5.7, the yellow heart class is clearly visible and in all 5 runs, the class is correctly segmented and labelled as a single class. The number of clusters in the obtained general model varied from 8 till 11, the segmented images and graphs of both models are also shown in the figure. Both FEMOS segmented images show that the fundamental information about leaves, background and flower is preserved. The yellow heart class ($R = 240; G = 227$) is clearly visible as an extra class in the right corner of the 8-class graph, next to the white background class ($R = 246; G = 241$). Compared to the 8-class model, the 11-class FEMOS segmented image has two additional background classes and one extra green leave class, as shown more clearly in the corresponding graphs. The difference between csi-FCM and FEMOS is clearly visible if the graphs of both Figures 5.6

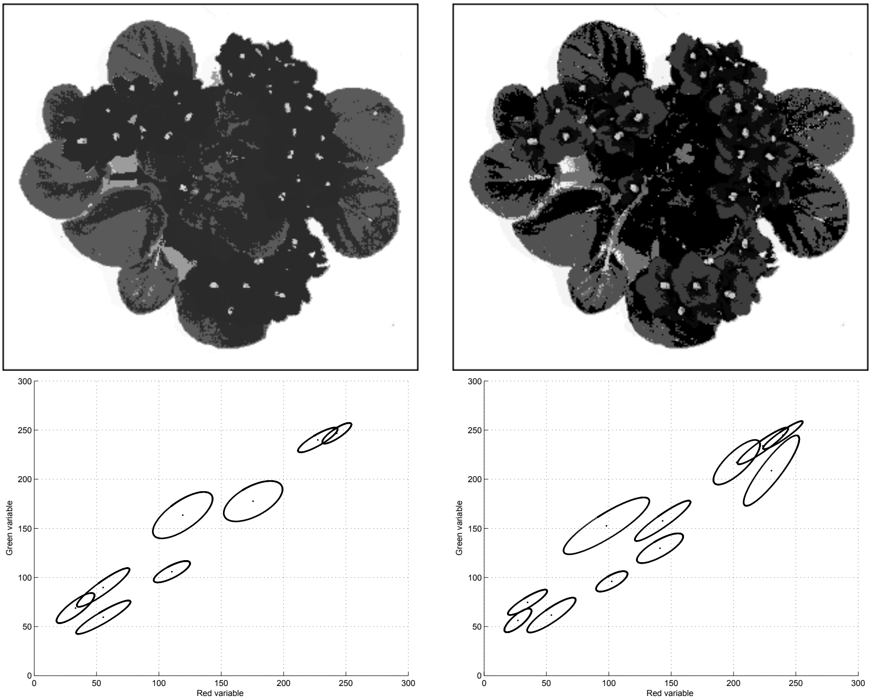

Figure 5.7: *The FEMOS segmented African Violet: the 8-class segmented image (upper left), the corresponding covariance and centroid graph (lower left), the 11-class segmented image (upper right) and the corresponding covariance and centroid graph (lower right).*

and Figure 5.7 are compared. Although there is some overlap between the white background class and the yellow heart class, the FEMOS procedure is consequently successful in estimating the yellow heart class. The csi-FCM clustering technique is not capable in properly modelling all the classes of this African violet image. The example shows that when the FEMOS procedure is applied as an unsupervised classifier the results are accurate and precise compared to a traditional unsupervised classifier like csi-FCM. Although the number of classes in the general model may vary, the represented information does not. For all five runs, the FEMOS procedure extracts the relevant information from the image.

5.4 Discussion and conclusion

Although the FEMOS procedure shows resemblance with traditional clustering techniques, it should not be considered as a new clustering technique. The number of resulting clusters produced by the FEMOS procedure is not constant for different runs, as shown in the third experiment. This is caused by the class extension stage, see Figure 5.1, where a subset of pixels from the candidate class are clustered in two classes with an unsupervised classifier. It is not guaranteed the used classifier exactly estimates the two subclasses and thus one of the classes is split instead. Eventually, the appropriate subclasses will be extracted by the FEMOS procedure due to the cluster validation criterion, though this is in contrast with traditional clustering techniques as shown in experiment three where an increase of clusters results merely in an increase of oversegmented classes while the relevant classes are missed. The Feedback Multivariate Model Selection procedure presented in this paper is a general class modelling approach which can be applied for the unsupervised segmentation of multivariate images or training and test set estimation from multivariate images. The procedure uses a subset of the multivariate image to estimate a general model and evaluates the used model with the original multivariate image via a model evaluation criterion. The procedure is not classifier dependent, in this paper the csi-FCM and LDA were selected for respectively the unsupervised and supervised classifier. The use of subsets allows the FEMOS procedure to handle even huge multivariate images and avoid large data storage or computation times. FEMOS' single parameter is a threshold value for the stop criterion and determines the amount of detail in the segmented image. An exact value for the stop criterion is not required as the segmentation outcome is mainly user or application dependent, but experiments with different type of multispectral images have shown that a threshold value of 0.25 results in detailed segmented images. A new visualization technique for segmented images or graphs is also presented which improves visual comparison with the original image. This technique is called class coloring and automatically generates color labels for segmented images or graphs. Experiments have shown that the FEMOS method has a superior value compared to the traditional Multivariate Image Analysis method for the estimation of latent or small classes for training or test sets. This is confirmed when the FEMOS method is applied as an unsupervised segmentation routine where traditional routines are outperformed in terms robustness and accuracy.

5.5 Acknowledgements

This work was partially funded by the Dutch Ministry of Economic Affairs under the IOP (Innovation Oriented Research) programme and the Ministry of Agriculture, Nature Management and Fisheries. The authors acknowledge the contribution of G. Polder and G. van der Heijden of Plant Research International in Wageningen with the use of their spectral imaging equipment. The authors wish to thank Ron Wehrens for his useful comments and contributions to the paper. Torbjörn Lestander is acknowledged for his contribution to the wood experiment.

Bibliography

[1] B. Park, Y. Chen, and R. Huffman, “Integration of visible/NIR spectroscopy and multispectral imaging for poultry carcass inspection,” *Journal of Food Engineering*, vol. 30, pp. 197–207, 1996.

[2] K. C. Lawrence, W. R. Windham, B. Park, and J. Buhr, “Hyperspectral imaging for poultry contaminant detection,” *NIR News*, vol. 12, no. 5, pp. 3–6, 2001.

[3] J. Wold and K. Kvaal, “Mapping lipid oxidation in chicken meat by multispectral imaging of autofluorescence,” *Applied Spectroscopy*, vol. 54, no. 6, pp. 900–909, 2000.

[4] G. Polder, G. van der Heijden, and I. Young, “Spectral image analysis for measuring ripeness of tomatoes,” *Transactions of the ASAE*, vol. 45, pp. 1155–1161, 2002.

[5] N. Aleixos, J. Blasco, F. Navarron, and E. Molt, “Multispectral inspection of citrus in real-time using machine vision and digital signal processors,” *Computers and Electronics in Agriculture*, vol. 33, pp. 121–137, 2002.

[6] D. Guyer and X. Yang, “Use of genetic artificial neural networks and spectral imaging for defect detection on cheries,” *Computers and Electronics in Agriculture*, vol. 29, pp. 179–194, 2000.

[7] P. Martinsen and P. Schaare, “Measuring soluble solids distribution in kiwifruit using near-infrared imaging spectroscopy,” *Postharvest Biology and Technology*, vol. 14, no. 3, pp. 271–281, 1998.

[8] J. Sugiyama, “Visualisation of sugar content in the flesh of a melon by near-infrared imaging,” *Journal of Agricultural and Food Chemistry*, vol. 47, pp. 2715–2718, 1999.

[9] J. Wold, F. Westad, and K. Heia, “Detection of parasites in cod fillets by using SIMCA classification in multispectral images in the visible and NIR region,” *Applied Spectroscopy*, vol. 55, no. 8, pp. 1025–1034, 2001.

[10] B. vandeGinste, D. Massart, L. Buydens, S. de Jong, P. Lewi, and J. Smeyers-Verbeke, *Handbook of Chemometrics and Qualitmetrics: Part B.* Data handling in science and technology-volume 20B, Amsterdam: Elsevier, 1998.

[11] J. Banfield and A. Raftery, “Model-based gaussian and non-gaussian clustering,” *Biometrics*, vol. 49, pp. 803–821, 1993.

[12] R. Wherens, L. Buydens, C. Fraley, and A. Raftery, “Model-based clustering for image segmentation and large datasets via sampling,” Technical report 424, Department of Statistics, University of Washington, February 13 2003.

[13] P. Geladi and H. Grahn, *Multivariate Image Analysis*. John Wiley & Sons Ltd., 1996.

[14] W. van den Broek, *Chemometrics in spectroscopic near infrared imaging for plastic material recognition*. PhD thesis, Catholic University of Nijmegen, 1997.

[15] W. Chang, “On using principal components before separating a mixture of two multivariate normal distributions,” *Applied Statistics*, vol. 32, no. 3, pp. 267–275, 1983.

[16] J. Noordam, W. van den Broek, and L. Buydens, “Multivariate image segmentation with cluster size insensitive Fuzzy C-Means,” *Chemometrics and Intelligent Laboratory Systems*, vol. 64, no. 1, pp. 65–78, 2002.

[17] M. R. Rezaee, B. Lelieveldt, and J. Reiber, “A new cluster validity index for the Fuzzy C-Means,” *Pattern Recognition Letters*, vol. 19, pp. 237–246, 1998.

[18] R. Haralick and L. Shapiro, *Computer and Robot Vision*, vol. 1. Addison-Wesley Publishing Company, Inc., 1992.

[19] K. Fukunaga, *Introduction to Statistical Pattern Recognition, 2nd edition*. San Diego: Academic Press, 1990.

[20] P. Geladi, “New challenges in multivariate image analysis,” in *Eastern Analytical Symposium*, vol. 1, EAS, 2002.

[21] G. Polder, G. W. A. M. van der Heijden, L. C. P. Keizer, and I. T. Young, “Calibration and characterization of imaging spectrographs,” *Journal of Near Infrared Spectroscopy*, vol. 11, pp. 193–210, 2003.

[22] P. Geladi, J. Swerts, and F. Lindgren, “Multiwavelength microscopic image analysis of a piece of painted chinaware,” *Chemometrics and Intelligent Laboratory Systems*, vol. 24, pp. 145–167, 1994.

[23] J. Noordam, W. van den Broek, and L. Buydens, “Perspective of inline control of latent defects and diseases on french fries with multispectral imaging,” in *SPIE, Food Safety and Agricultural Monitoring* (Y. R. Chen and G. E. Meyer, eds.), vol. 5271, (Providence, Rhode Island USA), SPIE, 2003.

[24] L. Dao and M. Friedman, “Chlorophyll, chlorogenic acid, glycoalkaloid and protease inhibitor content of fresh and green potatoes,” *Journal of Agricultural and Food Chemistry*, vol. 42, no. 3, pp. 633–639, 1994.

[25] E. J. Edwards, R. E. Saint, and A. H. Cobb, “Is there a link between greening and light-enhanced glycoalkaloid accumulation in potato (Solanum Tuberosum L) tubers,” *Journal of the Science of Food and Agriculture*, vol. 76, pp. 327–333, 1998.

[26] P. Slanina, “Solanine (glycoalkloids) in potatoes: toxicological evaluation,” *Food and Chemical Toxicology*, vol. 28, pp. 759–761, 1990.

Chapter 6

Detection and classification of latent defects and diseases on raw French fries with multispectral imaging

Abstract

This paper describes an application of both multispectral imaging and RGB color imaging for the discrimination between different defect and diseases on raw French fries. Four different potato cultivars generally used for French fries production are selected from which fries are cut. Both multispectral images and RGB color images are classified with parametric and non-parametric classifiers. The effect of applying different preprocessing techniques on the spectra prior to classification was also investigated. The best classification results in terms of accuracy, yield and purity are obtained with a modified version of standard normal variate (snv_mod) preprocessing for different classifiers and potato cultivars. The classification results of the multispectral images are compared with RGB images and the results show that the support vector classifier gives the best classification performance for the snv_mod preprocessed multispectral images and k-nearest neighbors classifier gives the best classification performance for raw RGB images. The detection of the latent greening defect in French fries with the exploration of multispectral images shows the additional value of multispectral imaging for French fries. A comparison between the

multispectral images and the RGB color images confirms this since this type of defect is not visible in the color images.

6.1 Introduction

The consumer market for post harvest food products demands a high quality. Quality criteria are not only related to the presence of external defects, deformations and visible diseases, but also to the presence of ingredients and constituents which are harmful or even toxic for humans. The spatial distribution of the defects and diseases require the use of inspection systems based on image analysis. Existing visual inspection systems commercially available on the market often use gray-value cameras to detect external defects. Until recently, inspection systems equipped with gray value camera's were sufficient for the detection of defects in French fries as the discrimination between good fries and defect fries could easily be obtained. Traditionally, consumers have preferred that French fries are prepared from potatoes that have been peeled before being cut into pieces. However, potato wedges and French fries that are still (partially) covered with peel have become more available and more acceptable in the past years. It is assumed that consumers perceive these products to be more healthy and natural compared to the original French fries. Previously reported inspection systems [1, 2, 3] for whole potatoes are equipped with 3 CCD colour camera's but cannot differentiate between good product and various defects successfully because these systems lack spectral resolution. Therefore, new trends as described above for the discrimination between peel and different defects and diseases make demands on these systems that no longer can be fulfilled. Only use of the spectral properties of specific constituents and ingredients offers possibilities for the discrimination. In literature [4], the visible and near infrared regions of the electromagnetic spectrum are investigated for the detection of internal and external potato defects on whole potato tubers. The selected wavelengths for the best discrimination between good and defect potatoes is in both the visible and Near Infrared (NIR) range of the spectrum. However, the system lacks spatial resolution as no indication of disease area can be obtained with the method due to single point measurements. Furthermore, according to the authors the method is not suitable for the detection of small disease spots as the probe requires a rather large measuring area compared to the spot size. With the availability of multispectral camera's which operate in the visible part of the spectrum a new area of applications becomes available where both spatial information and spectral resolution can be used. The development and application of multispectral imaging systems has been reported for the quality inspection of poultry [5] and chickens [6], the measurement of ripeness of tomatoes [7], the inspection of cherries [8], the spatial distribution of soluble solids in kiwi fruit and melons [9, 10] and detection of parasites in cod fillets [11]. As for the detection of defects on French fries, two patents[12, 13] have been filed which describe systems that use two spectral bands for the spectral discrimination between peel and potato flesh. However, classification performance is not considered and no attempt has been made to discriminate between different defects and diseases.

One of the goals of the presented research is to investigate if multispectral imaging improves discrimination between potato flesh, potato peel and potato defects on French fries. Therefore, both multispectral images and RGB color images of French fries are classified with different supervised classifiers to determine the best performing classifier. The French fries used in the experiments are produced from four cultivars which are frequently used for French fries production. Both multispectral images and RGB color images are captured prior to class labelling by a product expert. Due to material specific variables as particle size, surface structure and particle distribution scattering of the spectra occurs which results in undesired spectral variations. Many preprocessing techniques are proposed to remove these undesired spectral variations [14, 15]. Therefore, a second objective is to select the best performing classifier for both multispectral and RGB color images, combined with applying different well-known data preprocessing techniques on the spectra prior to classification. Both parametric classifiers and non-parametric classifiers are selected for the classification of the raw and preprocessed spectra.

The paper is organized as follows: Section 6.2 describes the used classification and preprocessing techniques, Section 6.3 discusses the measurement setup for the multispectral images and the required spectral and spatial calibration procedures, followed by a explanation of a general strategy for the extraction of training and test sets. In Section 6.4 the multispectral explorative results are discussed and the classification results of the multispectral images are compared with the classification results of the RGB images. In the last section the conclusions are given.

6.2 Theory

6.2.1 Classification

For the classification of the RGB color and multispectral images three supervised classification techniques gave been selected. The K-Nearest Neighbour classifier (knnc) and Support Vector Machines classifier (svc) have been selected for their good classification performance for high dimensional data sets for Near-infrared data [16] and multispectral remote sensing images [17, 18]. The fisher Linear Discriminant classifier (fisherc)is selected because literature shows that it gives good results for the classification of multispectral images [19, 14, 7, 20]. The parametric fisher classifier estimates the class dependent mean and covariance matrixes from the training set. The optimal parameter k for the knnc and the optimal kernel and the corresponding parameters for the svc must be set beforehand and are estimated from the training data. A detailed description of the classifiers can be found in literature [21, 22] and will not be further discussed in this paper. A Matlab toolbox PrTools[23] contains all the above mentioned classifiers and is used in the experiments.

Accuracy is used to evaluate classifier performance. The accuracy (ac) of a classifier is expressed as a percentage:

$$ac = \frac{\#correctly\ classified\ pixels}{total\ number\ of\ pixels} \times 100\% \tag{6.1}$$

The accuracy gives just a general classifier performance indication for all classes, for an individual class performance the type I error (α) and type II error (β) must be evaluated [24]. A type I error corresponds to the probability of misclassifying a member of a class as a non-member (false negative) and a type II error is the probability to classify a non-member as a member (false positive). Low α values of a class indicate that only a small fraction of that class is misclassified (high yield). A low β value for a class indicates that the class contains a small fraction of non-class members, which means that the class is very pure (high purity). Thus, α is a measure for yield, β is a measure for purity. In case of French fries inspection, low α and β for the good fries are preferred as a high yield and a high purity are required commercially. A low β value for the peel class is also required to prevent that defects are recognized as peel.

6.2.2 Preprocessing

Variations within individual Near Infrared (NIR) reflectance spectra are often due to problems associated with scattering. The scattering depends on the physical nature of the sample and is influenced by path length changes through the sample and the scatter of radiation at the surface of particles. The resulting spectra can have differences in baseline slopes and offsets. Many preprocessing techniques have been proposed to eliminate those additive and multiplicative differences between spectra that are not caused by a variation in chemical concentration. Some of those techniques have been applied successfully in various NIR applications[14, 25, 15]. To investigate if spectral preprocessing improves classification performance of multispectral images recorded in the 400-900 nm region of the electromagnetic spectrum, several preprocessing techniques have been applied on the data before training and testing the classifiers. These preprocessing techniques have shown to give good performance in combinations with classification techniques [14], but not in combination with the classifiers used in this paper. The following preprocessing techniques are considered:

- Standard Normal Variate (snv)
- modified Standard Normal Variate (snv_mod)
- 1nd derivative (1d), Savitsky-Golay, window size 7 (diff1d)
- 2nd derivative (2d), Savitsky-Golay, window size 7 (diff2d)

These techniques are widely known and well described in literature [14, 15] and will therefore be discussed briefly. Snv removes additive and multiplicative effects from the spectral data, resulting in a spectrum with zero mean and a variance equal to one. Snv_mod is similar to snv, except the mean spectral value of the spectra is added to the snv result. The mean value of the preprocessed spectrum is no longer zero but has a positive offset equal to the mean value of the spectrum. The derivatives not only remove additive baselines and sloped baselines but also addresses problems of overlapping peaks. A drawback of differentiation is that it amplifies noise. Therefore, it is necessary to smooth the data beforehand. Here, a combined smoothing and derivative operation is performed according to the method of Savtisky-Golay [24] as described in literature [26]. The above preprocessing techniques are applied to individual spectra and no information about reference spectra from the same class is required. This is an important requirement as a priori class information of measured spectra is not present.

6.3 Material and methods

6.3.1 Measurement procedure

The image acquisition procedure consisted of two steps, first an RGB images was captured, secondly the multispectral image was captured. A blue polystyrene plate of 10× 25 cm. was used as a carrier for the fries. About 15 fries were positioned rowwise on the plate with a minimum distance of 1 cm between the fries. First, the plate was positioned in the lighting chamber and a colour RGB image was captured. Next, the plate was positioned on the stepper table and a multispectral image was recorded. A product expert classified and labelled the visible defects on the fries immediately after the image acquisition.

6.3.2 Potato cultivars

Four different cultivars were manually selected from a French fries production plant in the Netherlands. The selected potato cultivars Agria, Asterix, Bintje and Arcade are particularly used for French fries production in the Netherlands. The cultivars

Agria, Arcade and Bintje have a yellowish colored peel, Asterix has a reddish colored peel. About 50 kg from the four potato cultivars were selected based on visual inspection of external defects on the potatoes. The potatoes contained peel and showed the defects greening, black rot, greening and external damages. The potatoes were cleaned and peeled in a combined potato washer/peeler. After cleaning, the potatoes were cut into French fries and stored in a container filled with water to prevent browning. Immediately after the cutting process, the container with the fries was transported to the measurement setup and the fries were measured with both the color and multispectral camera setup. When all the fries of one cultivar were measured, the following cultivar was washed, peeled, cut and measured.

6.3.3 Instrumental

The potato color images of the experiments are captured by a Sony 3-CCD color camera. A prism in the camera splits the incoming light of the visible spectrum into a Red, Green and Blue part and the light is mapped on the corresponding CCD. A framegrabber in the computer digitizes the 3 images and delivers 3 different 8-bit gray-value images, which result in a multivariate colour image with 3 variables (Red,Green and Blue). To obtain homogeneous lighting on the camera's field of view, a special lighting chamber with high-frequency fluorescent tubes (6500K) was used.

Figure 6.1 depicts the multispectral imaging measurement setup. The multispectral French fries images are recorded with an ImSpector V9 imaging spectrograph (Spectral Imaging Ltd. Oulu, Finland) mounted on a Peltier cooled Qimaging PMI-1400EC (Burnaby, Canada) monochrome camera. The camera contains a Kodak KAF-1400EC class II CCD sensor (Eastman Kodak, Rochester,USA). The ImSpector V9 produces a multispectral image where the 430-900 nm part of the electromagnetic spectrum is recorded in 104 small bands (every 4.5 nm) for every pixel. The incoming light is split by a prism-grating-prism and projected on the 2 dimensional CCD in the camera. The CCD size is 1320 pixels along the spatial axis and 1035 pixels along the spectral axis of the system. Since the number of pixels in the spectral direction is larger than the number of distinguishable wavelength bands according to the specifications the pixels can be binned with a factor 9 ($1035/104 \approx 9$). A 2-dimensional spectral image is obtained by moving the object under the ImSpector during recording. The translation table used to move the fries with respect to the camera is a Lineartechniek Lt1-SP5-C8-600 translation table driven by a SDHWA 120 programable microstepping motor driver (Ever Elettronica, Italy). The stepsize of the translation table was chosen to match the spatial resolution of the spatial axis. The number of steps was chosen to capture the entire plate with French fries. The resulting images have a spatial resolution of 318×560 square pixels and a spectral dimension of 104 bands (about 100 Mb.) The used lighting setup consists of two

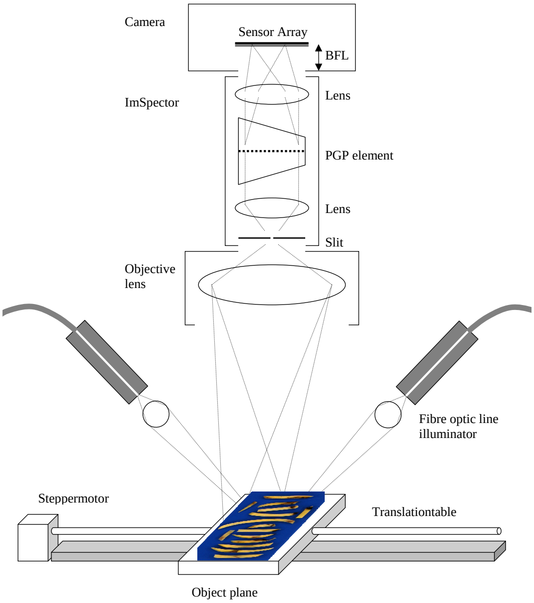

Figure 6.1: *An overview of the multispectral imaging setup*

Dolan-Jenner PL900 illuminators (Andover St. Lawrence, Mass.) with 150 W quartz halogen lamps. The scene was illuminated by two glass fiber optic line arrays (Vision Light Tech) of 0.002 inch × 6 inch aperture. Two Rod lenses were positioned in front of the line arrays. Detailed information about the used multispectral imaging setup and ImSpector calibration is described in literature [27].

6.3.4 Calibration and image preprocessing

To make the measured spectra independent of factors such as the spectrum of the used light source, the quantum efficiency of the camera, different noise sources and temperature a spectral correction is required. The images are corrected according to:

$$I(x)_{spectral} = \frac{I(x)_{raw} - I(x)_{dark}}{I(x)_{whiteref} - I(x)_{dark}} \tag{6.2}$$

where $I(x)_{spectral}$ is the corrected image, $I(x)_{raw}$ is the uncorrected image, $I(x)_{dark}$ is the dark current image and $I(x)_{whiteref}$ is the white reference image. The x-axis is perpendicular to the direction of movement. The white reference image has been taken from a white tile of PTFE-plastic (TOP Sensor Systems WS-2) with a spectral reflectance of over 0.98 from 400 till 1500 nm. The dark current image was obtained by taking an image with a closed lens cap and lights turned off. The correction procedure as described above requires that the used white reference covers the entire field of view of the camera. In that case, little illumination differences in the field of view such as inhomogeneous lighting will automatically be corrected. Subsequently, the background in the images is removed via an image threshold procedure.

6.3.5 Filtering of spectra

The spectra of the spatially and spectrally corrected multispectral images are filtered with a Savtisky-Golay filter [24] with a kernel size of 7 bands to remove remaining noise and spikes. The low radiation from the light source in the lower part of the visible band (between 430 and 450 nm) combined with the low sensitivity of the CCD camera in the lower and upper parts of the spectrum produces a low signal to noise ratio in these parts of the spectrum. Therefore, after the Savitsky-Golay filtering the spectrum is reduced to a range of 450-870 nm.

6.3.6 Training and test set selection of defect classes

During the color and multispectral measurements of the French fries a product expert classified and labelled the visible defects on the fries. Based on the defects selected by the product expert, the following classes are chosen: potato flesh, visible greening, peel, green peel, rot, damaged and internal red/brown discoloring.

A drawback of manual visual inspection is that latent defects which are not visible for the human eye cannot be recognized and labelled as such. If present and detectable with multispectral imaging, these defects can only be found in the multispectral images during an explorative analysis of the multispectral images. For the explorative analysis a new procedure for the modelling and representation of classes in multivariate images is developed to tackle this problem. The procedure is based on the Multivariate Image Analysis (MIA) approach as described thoroughly in literature [28]. The procedure is called Feedback Multivariate Model Selection (FEMOS)[29] and combines unsupervised and supervised classifiers with a model evaluation criterion to extract classes from the multivariate image in an iterative manner. The procedure uses a subset of the multivariate image to estimate a general model and evaluates this model with the complete original multivariate image via a model evaluation criterion. It operates in spectral space and estimated classes can be stored for later use. The saved pixels of different classes are combined to compose a representative training and test set. The positions of the labelled regions in a multispectral image are used to extract pixels from similar regions in the corresponding RGB image.

6.3.7 Data sets

The set of labelled pixels extracted from the multispectral images as described in Paragraph 6.3.6 comprise 7 classes for each cultivar and is referred to as the original set. The minimum required discrimination capacity for French fries inspection is between features potato flesh, peel and various defects. Therefore, a second data set is created from the original set that exist of the classes potato flesh, peel and defects where the latter contains all defects and diseases. This set is further referred to as the merged set.

As the number of pixels per class differ enormously (from 36000 pixels for the potato flesh class to 550 pixels for the internal browning class), a subset is extracted from each class in each data set. The number of pixels per class is limited to 500. When classifying high dimensional data, care must be taken for the selected number of pixels in combination with the type of classifier. Although increasing the number of spectral bands (dimensionality) potentially provides more information about class separability this positive effect is diluted by poor parameter estimation for second order statistics[30]. The lower bound for the required number of pixels is determined by the dimension of the data and the used classification technique. In case of linear decision boundaries, the required number of points in each class is linear related with the dimension of the data, with quadratic classifiers, this relation becomes quadratic [21, 30]. Therefore, only a parametric classifier with lineair decision boundaries (fisherc) is used as there are limited number of pixels available in some disease classes.

6.3.8 Experimental procedure

Each dataset is split in half to create a training set and a test set. The classifiers are trained with the training set and validated with the test test. The confusion matrix is calculated and the corresponding accuracy, α error and β error are calculated. To visualize the results, the accuracy of each classifier for different combinations of preprocessing technique and cultivar is shown in a graph. In a single graph, the results for raw RGB data, raw multispectral data and preprocessed multispectral data are combined. This offers an opportunity to visualize trends and allows an easy visual comparison between classifier accuracy performance. The classification performance of the RGB color images and the raw multispectral images serve as a reference in order to determine if spectral preprocessing indeed reduces the classification error. The (α) and (β) error for the best performing combination of classifier and preprocessing technique are discussed in the text. The discussion focusses on both the potato flesh and peel class as these are classes which are important in terms of yield and purity. Furthermore, deviating class performances are also discussed. The following spectral preprocessing techniques as described in section 6.2.2 are applied to the multispectral images: snv_mod, snv, diff2d and diff1d.

To determine the optimal parameters for both knnc and svc classifier, a leave-one-out (LOO) procedure is performed for the two training data sets for both RGB color and multispectral images. The best parameter k for knnc was found by testing all k values from 1 to 10 for the RGB images and from 1 to 14 for the multispectral images. For both image types, knnc with the parameter $k = 3$ gives the best results and is used in the experiments. A similar LOO procedure was performed for the svc where radial basis functions, polynomial and exponential functions for kernel were evaluated for different values for the separability parameter C [18]. The exponential kernel with $C = 2$ performs best and is used in the experiments.

6.4 Results and discussion

6.4.1 Exploration of spectra

A selection of 50 spectra of fries with the greening defect from the Agria cultivar are visualized in Figure 6.2 before and after applying different preprocessing techniques. The spectra are filtered as described in Paragraph 6.3.5. The raw spectra in Figure 6.2(a) show an offset, a slope and a large within-class variance. To separate meaningful from meaningless information due to the rugged surface and the wavelength dependent scattering the spectra are preprocessed. Figure 6.2(b) shows the same spectra after mean centering. An offset of the spectra is removed although there still remains some divergence between the samples. In Figure 6.2(c) the snv processed spectra shows not only an offset correction but also a divergence reduction compared to the mean centered spectra. In Figure 6.2(d) both the offset and slope of the spectra are removed by the first derivative. Although the graphs shows that offsets and slopes are largely removed after preprocessing, experiments will indicate if classification performance actually increases.

6.4.2 Multispectral image analysis

In Figure 6.3, the mean spectra of several diseases are shown with the corresponding position on the fries. The image is a pseudocolour image reconstructed from the multivariate image stack containing all the spectral information. The spectra in the graph indicate that the discrimination between some of the defects might be a challenging task as there is little spectral distinction between them. The spectra are rather smooth and do not contain particular peaks, besides the chlorophyll absorbtion peek of greening around 670 nm. Potatoes turn green on a cumulative exposure to light

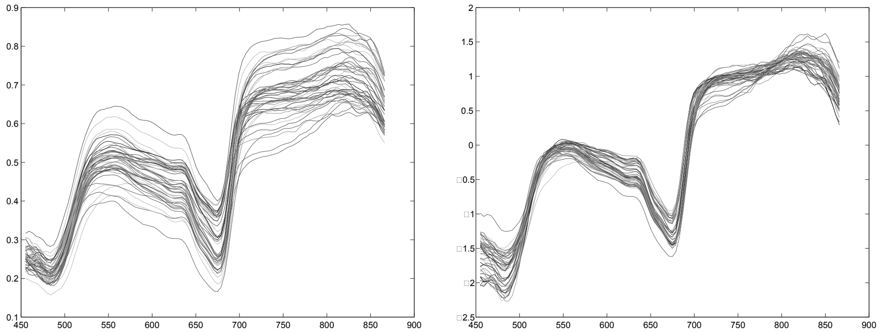

(a) Spectra of the greening defect

(c) snv corrected spectra

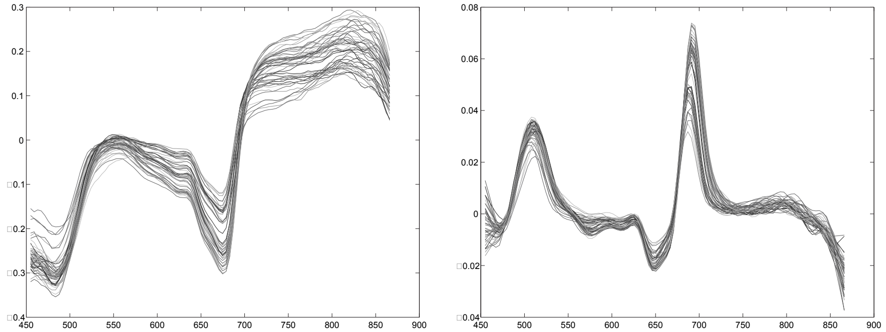

(b) mean centered spectra

(d) 1st derivative spectra

Figure 6.2: *The raw spectra and the corrected spectra of the greening defect*

as a result of the formation of chlorophyll. Such tubers develop a bitter taste, off -flavor and may cause health hazards and, in some specific instances, death because of high solanine content [31, 32]. The concern with green potatoes is not the chlorophyll, which is tasteless and harmless, but the solanine which develops in the the same area in the potato along with the chlorophyll. Therefore, green potatoes must be removed as these components affect the quality of potatoes and potato products, especially in respect to appearance, texture and nutritive value. Heavily greening is visible for the human eye and thus detection with standard RGB color cameras is sufficient. An extensive multivariate analysis of the multivariate images as described in Paragraph 6.3.6, demonstrated that a number of fries showed similar spectra as the fries with greening although the product expert did not label these fries as greening. In fact, these fries were labelled as good fries, as the light greening was not visible

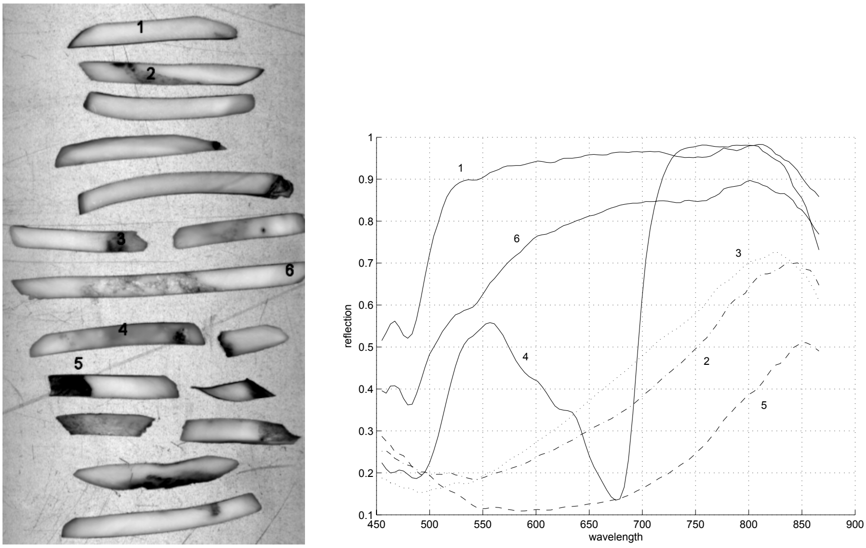

Figure 6.3: *Several typical French fries defects and diseases with their corresponding spectra. 1=potato flesh, 2=peel, 3=damage, 4=greening, 5=external rot, 6= browning*

for the human eye. Figure 6.4(a) shows a pseudo color image of the Arcade cultivar taken with the multispectral measurement setup. The fry in the upper part of the image is marked with number one, the fry in the lower part of the image is marked number two. Fry number one was labelled as good fry, fry number two was labelled as greening. On both fries, a circular marker indicates the location of a spectral point measurement. These spectra and the second derivatives taken from these spectra are shown in the graphs of respectively figure 6.4(b) and figure 6.4(c). Both spectra in the graph with the second derivative show a peak in the 670-680 nm region, a region which is known to be the absorbtion wavelength of chlorophyll-a. It was shown in Figure 6.3 that this peak is absent in the spectra of good potato flesh. Therefore, the fry with marker one is considered to contain some greening, though invisible for the human eye. The surplus value of multispectral imaging compared to traditional RGB color imaging is shown with this example. In multispectral French fries images, latent defects are already visible before they become visible for the human eye. For a true evaluation of the difference in classification performance for both multispectral images and RGB color images the number of classes for both image types must be equal. This is a problem for the nonvisible greening defect which cannot be detected by the product expert and is consequently not available as a labelled class in the RGB

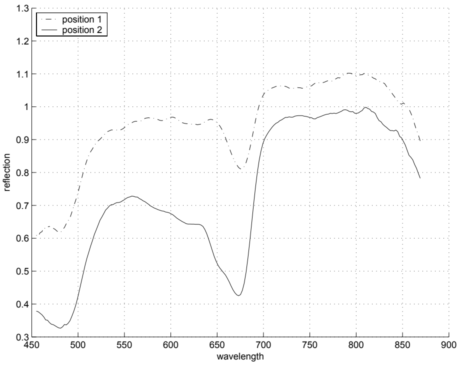

(b) The original spectra

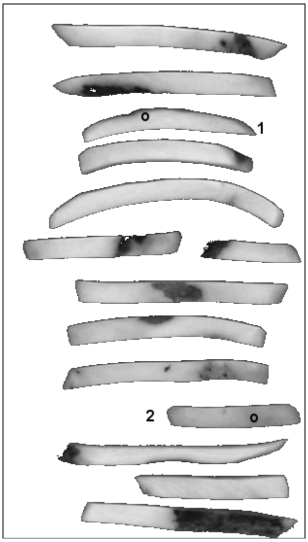

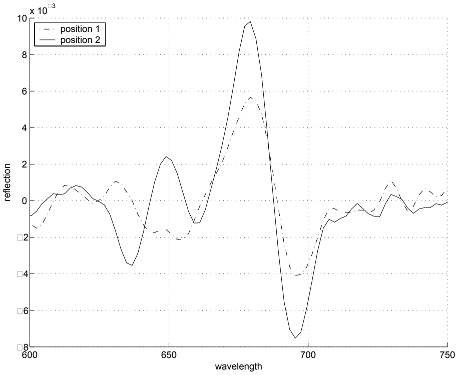

(a) An Arcade pseudo color image

(c) The 2nd derivative of the spectra (zoomed)

Figure 6.4: *Pseudo color image of multispectral image and both original and 2nd derivative spectra for marked position (circle) on fry one (labelled as good fry) and fry two (labelled as greening*

color images. Therefore, the RGB color classification results are actually worse then the presented error classification percentages in the graphs of subsequent Paragraphs.

6.4.3 Experiment 1: classification results of original Set

Figure 6.5 shows the graphs with the classification accuracy for different classifiers with the original set. The labels on the Y-axis correspond with the preprocessing technique as discussed in section 6.3.8. The four horizontal bars represent the cultivars

Asterix, Agria, Arcade and Bintje (from top to bottom).

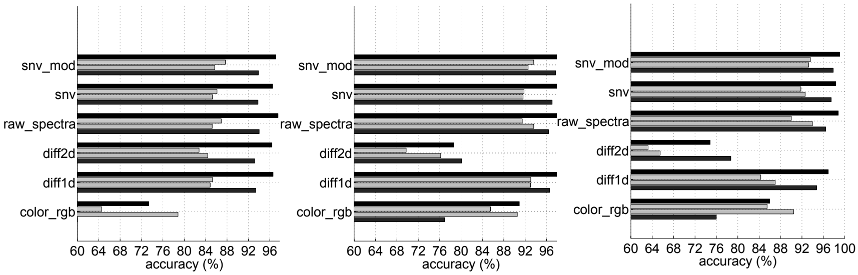

(a) fisherc (b) knnc (c) svc

Figure 6.5: *The classification results of the original set for different classifiers. The bars in the graph represent the cultivars Asterix, Agria, Arcade and Bintje (top to bottom)*

Multispectral classification results

Although both svc and knnc give good results, knnc performs better for different cultivars for different individual preprocessing techniques compared to the svc. However, the best results are obtained with the svc with snv_mod preprocessing, the error percentage varied from 99.1% for the Asterix cultivar and 93.7% for the Arcade cultivar. A closer look at the the Asterix confusion matrix shows that the misclassification is between defect classes only, the classes potato flesh ($\alpha = 0, \beta = 0$) and peel ($\alpha = 0.012, \beta = 0$) are correctly classified. The snv_mod preprocessing halves the α error from $\alpha = 0.028$ to $\alpha = 0.012$ for the peel class compared to the raw spectra. As for the Arcade cultivar, the major misclassification is caused by the peel class ($\alpha = 0.24, \beta = 0.005$) which is classified as damaged ($\alpha = 0.112, \beta = 0.019$) and internal red/browning ($\alpha = 0.116, \beta = 0.02$). The confusion matrices for both Agria and Bintje show that the misclassification is mainly between the classes rot and damaged. Inspection of α and β error for the potato flesh and peel class for each cultivar shows that the snv_mod preprocessing reduces both errors compared with the raw spectra for both Agria and Arcade cultivar, for both Asterix and Bintje cultivar both errors are 0.

RGB classification results

The best classification results are obtained with knnc, the accuracy percentages vary from 90.9% for Asterix till 76.9% for Bintje. The Asterix confusion matrix shows that the classification error is caused by misclassification between rot ($\alpha = 0.24, \beta = 0.014$), green peel ($\alpha = 0.16, \beta = 0.04$) and peel ($\alpha = 0.064, \beta = 0.04$). The low knnc-Bintje accuracy is a result of lack of discrimination between greening ($\alpha = 0.272, \beta = 0.049$) and peel ($\alpha = 0.24, \beta = 0.049$), and between rot ($\alpha = 0.352, \beta = 0.033$), green peel ($\alpha = 0.306, \beta = 0.057$) and damaged ($\alpha = 0.256, \beta = 0.048$). The potato flesh class of all cultivars is correctly classified ($\alpha = 0, \beta = 0$), which is in contrast with the peel class that shows not only low yields for Arcade $\alpha = 0.28$, Bintje $\alpha = 0.24$ and Agria $\alpha = 0.26$, but also low purities as for the majority of the cultivars, the lowest purity is for the peel class.

6.4.4 Experiment 2: classification results of merged set

In this experiment, it was investigated if classification performance could be improved if the classes are combined to the absolute minimum required discrimination between classes good potato, peel and disease. Figure 6.6 shows the graphs with the classification accuracy for different classifiers. The labels on the Y-axis correspond with the preprocessing technique as discussed in section 6.3.8. The four horizontal bars represent the cultivars Asterix, Agria, Arcade and Bintje (from top to bottom).

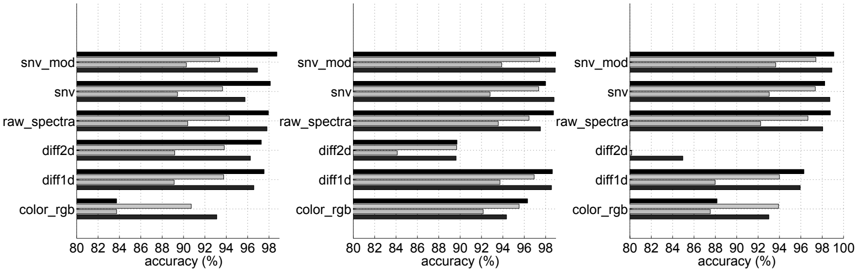

(a) fisherc (b) knnc (c) svc

Figure 6.6: *The multispectral and RGB classification results of the merged set for different classifiers. The bars in the graph represent the cultivars Asterix, Agria, Arcade and Bintje (top to bottom)*

Multispectral classification results

The best results are obtained with a combination of svc with snv_mod preprocessing, the accuracy percentage varied from 99.1% for Asterix till 93,9% for Arcade. The svc-Asterix confusion matrix with snv_mod preprocessing shows that the error is due to defects ($\alpha = 0.012, \beta = 0.002$) which are misclassified as peel($\alpha = 0.004, \beta = 0.006$). Compared to the raw spectra, snv_mod preprocessing reduces the α error from 0.016 to 0.004, and reduced the β error from 0.018 to 0.006 for the peel class. Potato flesh produces a high yield ($\alpha = 0, \beta = 0$) for all cultivars except Arcade ($\alpha = 0.016, \beta = 0.008$). In general, snv_mod preprocessing improves both the yield (low α error) and the purity (low β error) for the potato flesh and peel class.

RGB classification results

The best classification results are obtained with knnc, the error percentages vary from 96,3% for Asterix till 92,2% for Arcade. According to the confusion matrices for all cultivars, all objects of the potato flesh class are correctly classified ($\alpha = 0, \beta = 0$). The main error contribution is caused by defects which are classified as peel, with the Arcade cultivar as worst performing cultivar for peel ($\alpha = 0.04, \beta = 0.11$) and defects ($\alpha = 0.22, \beta = 0.02$) and Asterix as the best performing cultivar with the lowest β error for the peel class ($\alpha = 0.032, \beta = 0.032$).

Multispectral versus RGB

Figure 6.7 summarizes the difference between the best performing classifier (knnc) for the RGB images and the best performing combination of preprocessing and classifier (snv_mod + svc) for multispectral images for the two classification experiments. It is clear from the figure that the multispectral image classification accuracy outperforms the RGB image classification for both experiments. An increase in classification accuracy between the original set and the merged set indicates that the misclas-

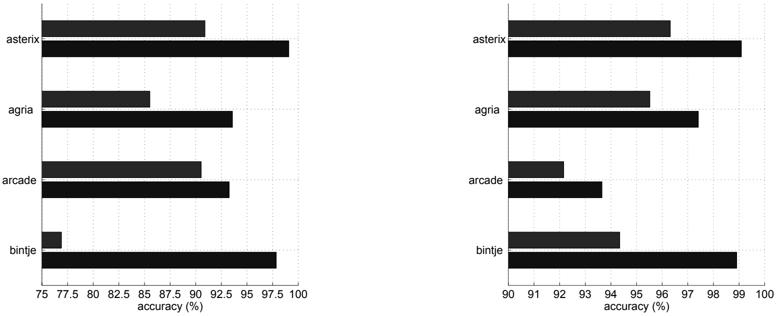

Figure 6.7: *Difference between the RGB results (upper bar) and the MS results (lower bar) for the best performing combination of preprocessing and classifier for the original (left) and merged (right) data sets*

sification in the original set is between different defect classes, as defect classes are combined to a single defect class in the merged set.

Although accuracy gives an indication of classifier performance over all classes, for a detailed class performance for the potato flesh and peel class the α and β error must be compared. In Figure 6.8 the α and β errors of the individual potato cultivars are averaged for both RGB color and multispectral images of the original and merged set. The average α and β error gives an indication of the performance difference between the best classifier for RGB images (knnc) and the best classifier for snv_mod preprocessed multispectral images in terms of yield and purity. The low α and β error for the potato flesh class for both image types and in both the original and merged data set indicate that this class is pure and almost completely classified correctly. This is not the case for the remaining classes, especially in RGB images the important peel class is misclassified and contains a rather large number of non-class members. The

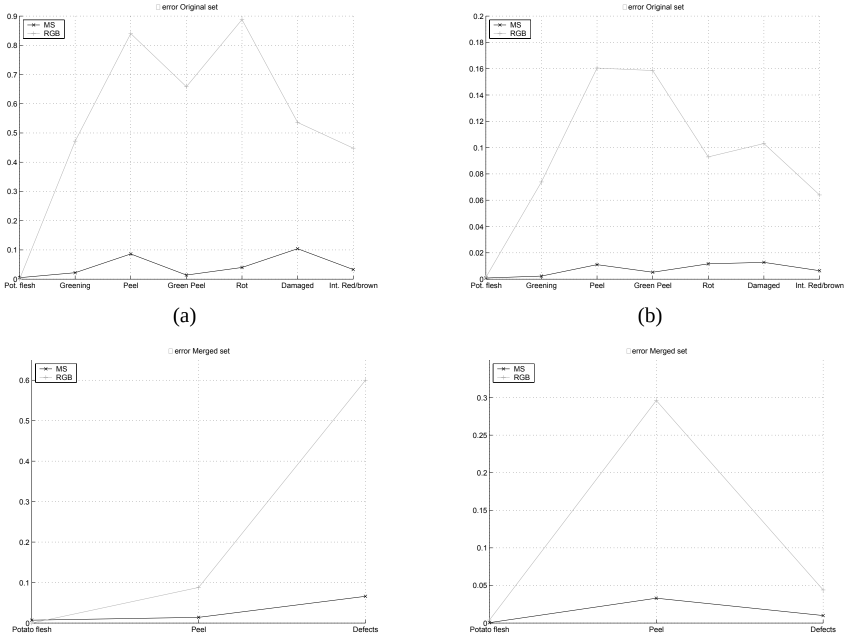

(a) (b) (c) (d)

Figure 6.8: *Overview of averaged α and β error for all cultivars for RGB and MS+snv_mod results. (a) α error of original set; (b) β error of original set; (c) α error of merged set; (d) β error of merged set;*

multispectral results show an error decrease for this class which ranges from 10-14 for the α and β error respectively. The multispectral results for the peel class in the merged set show an error reduction with a factor that ranges from 6-9 for the α and β error respectively. In general, the results show that multispectral imaging outperforms RGB imaging not only for accuracy but also improves both yield and purity for the two most important classes flesh and peel.

6.5 Conclusion

The latent greening defect in French fries detected with the exploration of the multispectral images shows the additional value of multispectral imaging for French fries. A comparison between the multispectral images and the RGB color images confirms this: the defect is not visible in the color images. This shows that a product expert labelling is not sufficient and a thorough explorative multivariate analysis is required to be able to detect and label all defects prior to classification.

Spectral preprocessing techniques like snv and both derivatives which remove mean and offset from the spectra give less good classification results for French fries multispectral images. This indicates that the mean value in the spectra is an additional discriminative feature that further improves classification results. This is confirmed by the good classification results for multispectral images with snv_mod, a variation of snv where the original mean is returned in the spectra. In general, the improvement of snv_mod preprocessing results in a reduction of both α and β error for the majority of the classes. The results show that combination of snv_mod preprocessing and svc gives the best performance for multispectral images while the knnc performs best for raw RGB color images.

The multispectral classification results outperform the RGB color classifications results for both data sets, the surplus of spectral resolution results in an improved classification accuracy for all four potato cultivars. When individual class performance is considered, the results indicate that snv_mod preprocessed and svc classified multispectral images improve both yield and purity for all classes in both data sets. Therefore, future visual inspection systems for raw French fries inspection should be equipped with multispectral camera's, the spectra must be preprocessed with snv_mod preprocessing and classified with a support vector classifier for best performance in terms of classification accuracy, yield and purity.

6.6 Acknowledgements

This work was partially funded by the Dutch Ministry of Economic Affairs under the IOP (Innovation Oriented Research) programme and the Ministry of Agriculture, Nature Management and Fisheries. The authors acknowledge the contribution of G. Polder and G. van der Heijden of Plant Research International in Wageningen with the use of their spectral imaging equipment.

Bibliography

[1] L. Zhou, V. Chalana, and Y. Kim, “PC-based machine vision system for real-time computer-aided potato inspection,” *International Journal of Imaging Systems and Technology*, vol. 9, no. 6, pp. 423–433, 1998.

[2] P. Heinemann, N. Pathare, and C. Morrow, “An automated inspection station for machine-vision grading of potatoes,” *Machine Vision and Applications*, vol. 9, pp. 14–19, 1996.

[3] J. Noordam, G. Otten, A. Timmermans, and B. van Zwol, “High-speed potato grading and quality inspection based on a color vision system,” in *SPIE, Machine vision and its Applications* (K. W. Tobin, ed.), vol. 3966, (San Jose, Californie), pp. 206–220, SPIE, 2000.

[4] R. Porteous, A. Muir, and R. Wastie, “The identification of diseases and defects in potato tubers from measurements of optical spectral reflectance,” *Journal of Agricultural Engineering Research*, vol. 26, pp. 151–160, 1981.

[5] K. C. Lawrence, W. R. Windham, B. Park, and J. Buhr, “Hyperspectral imaging for poultry contaminant detection,” *NIR News*, vol. 12, no. 5, pp. 3–6, 2001.

[6] J. P. Wold and K. Kvaal, “Mapping lipid oxidation in chicken meat by multispectral imaging of autofluorescence,” *Applied Spectroscopy*, vol. 54, no. 6, pp. 900–909, 2000.

[7] G. Polder, G. van der Heijden, and I. Young, “Spectral image analysis for measuring ripeness of tomatoes,” *Transactions of the ASAE*, vol. 45, pp. 1155–1161, 2002.

[8] D. Guyer and X. Yang, “Use of genetic artificial neural networks and spectral imaging for defect detection on cheries,” *Computers and Electronics in Agriculture*, vol. 29, pp. 179–194, 2000.

[9] P. Martinsen and P. Schaare, “Measuring soluble solids distribution in kiwifruit using near-infrared imaging spectroscopy,” *Postharvest Biology and Technology*, vol. 14, no. 3, pp. 271–281, 1998.

[10] J. Sugiyama, “Visualization of sugar content in the flesh of a melon by near-infrared imaging,” *Journal of Agricultural and Food Chemistry*, vol. 47, pp. 2715–2718, 1999.

[11] J. P. Wold, F. Westad, and K. Heia, “Detection of parasites in cod fillets by using SIMCA classification in multispectral images in the visible and NIR region,” *Applied Spectroscopy*, vol. 55, no. 8, pp. 1025–1034, 2001.

[12] D. Campbell, “System and method of inspecting peel-baring potato pieces for defects, patent no. 5884775,” 1999.

[13] D. Campbell, “Detecting defective peel-bearing potatoes in a random mixture of defective and acceptable peel-bearing potatoes, patent no. 6252189189b1,” 2001.

[14] P. de Groot, G. Postma, W. Melsen, and L. M. Buydens, “Selecting a representative training set for the classification of demolition waste using remote NIR sensing,” *Analytica Chimica Acta*, vol. 392, pp. 67–75, 1999.

[15] A. Candolfi, R. de Maesschalck, D. Jouan-Rimbaud, P. Hailey, and D. Massart, “The influence of data pre-processing in the pattern recognition of excipients near-infrared spectra,” *Journal of Pharmaceutical and Biomedical Analysis*, vol. 21, pp. 115–132, 1999.

[16] Y. Roggo, L. Duponchel, and J. Huvenne, “Comparison of supervised pattern recognition methods with McNemar’s statistical test: Application to qualitative analysis of sugar beet by near-infrared spectroscopy,” *Analytica Chimica Acta*, vol. 477, pp. 187–200, 2003.

[17] M. Pal and P. Mather, “Assessment of the effectiveness of support vector machines for hyperspectral data,” *Future Generation Computer Systems*, vol. in press, 2003.

[18] Gualtieri, “Support vector machines for hyperspectral remote sensing classification,” in *SPIE, Advances in Computer Assisted Recognition*, vol. 3584, (Washington, D.C.), pp. 1–12, SPIE, 1998.

[19] W. van den Broek, *Chemometrics in spectroscopic near infrared imaging for plastic material recognition*. PhD thesis, Catholic University of Nijmegen, 1997.

[20] J. Witjes, *Explorative analysis of chemometrics in magnetic resonance (spectroscopic) imaging of human brain tumors*. PhD thesis, Catholic University of Nijmegen, 2001.

[21] K. Fukunaga, *Introduction to Statistical Pattern Recognition, 2nd edition*. San Diego: Academic Press, 1990.

[22] W. Vapnik, *The Nature of Statistical Learning Theory*. Springer Verlag, New York, 1995.

[23] R. P. W. Duin, "Prtools_3, a matlab toolbox for pattern recognition." Website Delft University of Technology, 2000. `http://www.ph.tn.tudelft/duin/prtools`.

[24] B. vandeGinste, D. Massart, L. Buydens, S. de Jong, P. Lewi, and J. Smeyers-Verbeke, *Handbook of Chemometrics and Qualitmetrics: Part B*. Data handling in science and technology-volume 20B, Amsterdam: Elsevier, 1998.

[25] R. Barnes, M. Dhanoa, and S. Lister, "Standard normal variate transformation and de-trending of near-infrared diffuse reflectance spectra," *Applied Spectroscopy*, vol. 43, pp. 772–777, 1989.

[26] D. W. Hopkins, "Derivatives in spectroscopy," *Near Infrared Analysis*, vol. 2, no. 1, pp. 1–13, 2001.

[27] G. Polder, G. W. A. M. van der Heijden, L. C. P. Keizer, and I. T. Young, "Calibration and characterization of imaging spectrographs," *Journal of near Infrared Spectroscopy*, vol. 11, pp. 193–210, 2003.

[28] P. Geladi and H. Grahn, *Multivariate Image Analysis*. John Wiley & Sons Ltd., 1996.

[29] J. Noordam and L. van den Broek, W.H.A.M.and Buydens, "A new procedure for the modelling and representation of classes in multivariate images," *Chemometrics and Intelligent Laboratory Systems*, vol. submitted, pp. 759–761, 2004.

[30] C. H. Chen, *Information Processing for Remote Sensing for Multispectral and Hyperspectral Image Data*. World Scientific Publishing Co., 1999.

[31] L. Dao and M. Friedman, "Chlorophyll, chlorogenic acid, glycoalkaloid and protease inhibitor content of fresh and green potatoes," *Journal of Agricultural and Food Chemistry*, vol. 42, no. 3, pp. 633–639, 1994.

[32] P. Slanina, "Solanine (glycoalkloids) in potatoes: toxicological evaluation," *Food and Chemical Toxicology*, vol. 28, pp. 759–761, 1990.

Chapter 7

Conclusions and future prospects of multispectral imaging in food inspection

7.1 General

This thesis describes different novel chemometric techniques applied to multispectral images for quality inspection on agricultural products. The presented techniques and algorithms are originated from specific problems, in this case the detection of defects and diseases from multispectral images acquired from postharvest products. The algorithms presented in this thesis focus on the combined use of spatial and spectral information during image classification and also on the unsupervised classification and extraction of training and test sets from multispectral images. The chemometric techniques are applied on multispectral images acquired from agricultural food products. These images do not only have a huge number of spectral bands which makes training set selection a challenging task, they also contain classes with small defects or abnormalities where objects of these classes are easily missed.

7.2 Conclusions

Chapter 2 and Chapter 3 describe an unsupervised segmentation technique based on Fuzzy C-Means (FCM) which combines both spectral and spatial information to improve discrimination between objects of similar spectra. With respect to the combined approach of spatially and spectrally guided clustering one can conclude that there is a surplus value compared to the traditional form of FCM clustering. The first algorithm, called geometrically guided conditional FCM (ggc-FCM) uses a window of variable size to store a priori spatial information about spurious or small objects. An outlier threshold value determines which objects are removed in the defuzzification procedure, where at the same time edges are preserved. Although the ggc-FCM results are improved compared with FCM, in applications such as agricultural product inspection where each object must be assigned to a true product class, the use of a reject class is impractical and needs further optimization.

Therefore, in Chapter 3 the Spatially Guided FCM (sg-FCM) is presented that overcomes the reject class. sg-FCM segments multivariate images by incorporating both spatial and spectral information. The performance of sg-FCM is compared with both FCM and the combination of FCM and a majority filter (FCM-MAJORITY) in experiments with multivariate images where spectral information is not sufficient to discriminate between objects. The sg-FCM segmented images show more homogeneous regions and less spurious pixels compared to FCM and FCM-MAJORITY results.

Generally, defects or abnormalities on agricultural products which are inspected for appearance based quality represent small areas compared to the whole product area. FCM is often used as an unsupervised segmentation technique for the segmentation of these images, although known to be sensitive for unequal cluster sizes. Therefore, in Chapter 4 a cluster size insensitive FCM (csi-FCM) is described which is insensitive to unequal number of objects in clusters. Besides the required number of clusters no additional parameter settings are required. The performance of the csi-FCM algorithm is compared with two algorithms known to be insensitive for different number of points in clusters and the results show that the csi-FCM performs equally or better when high dimensional data is used.

In general, to grade a product based on a particular quality, classification of the image is required to be able to determine defect percentage. For the classification of multispectral images several supervised and unsupervised techniques are available. Unsupervised techniques are able to segment the image in regions based on a user selected number of classes. However, in particular applications the huge amount of data in multispectral images requires computational demands which are not feasible in most applications and in such applications supervised classification techniques can be used instead. For supervised classification, a representative training and test set is required which can be troublesome to obtain as there are multiple image bands to explore. A new procedure has been developed which is able to explore and segment a multivariate image. The feedback multivariate model selection (FEMOS) procedure is presented in Chapter 5 and is a general class modelling approach which can be applied either for the unsupervised segmentation of multivariate images or for training and test set estimation from multivariate images. The procedure combines both unsupervised and supervised techniques for the segmentation of the multivariate images where the segmentation process is controlled according the visual feedback principle of the Multivariate Image Analysis (MIA) procedure. The single parameter is a threshold value for the stop criterion and an exact value for the stop criterion is not required as the segmentation outcome is mainly user or application dependent. Experiments with different types of multispectral images showed segmented images with more details compared to traditional multivariate image analysis.

In Chapter 6, a food application is presented where both RGB color and multispectral images of French fries with latent defects and diseases are classified. Different supervised classifiers combined with different preprocessing techniques are evaluated for the best classification performance. The results show that the multispectral classification results outperform the RGB color images by a factor varying from 8-11, depending of the used cultivar. The best classification results for multispectral images are obtained with a support vector classifier with an exponential kernel and a modified version of standard variate normal preprocessing. The spectral preprocessing also improves both yield and purity for all classes. The best classifier for French fries RGB color images is 3-Nearest Neighbor without any spectral preprocessing. It was also shown that the use of multispectral imaging allows detection and classification of defects which are not visible in traditional RGB images.

7.3 Future expectations

7.3.1 Spectral image acquisition

The recent boost of spectroscopic imaging equipment like the Imspectors as used for the acquisition of the multispectral images in this thesis has resulted in many applications in agriculture. However, the majority of the applications take place in the visible party of the spectrum. This is more or less in contrast with the huge amount of literature about Near InfraRed (NIR) spectroscopy applications in agriculture which indicate that the NIR region is an interesting area for quality inspection of agricultural products. The major reason for this is that there are no suitable robust cameras available which can both operate in the NIR region of the electromagnetic spectrum and have a sensitivity comparable to existing NIR spectrometers. Although there are NIR camera systems which are used in several applications [1], both the robustness and the sensitivity of those camera systems is still not sufficient for practical applications. Furthermore, currently available Imspectors for the NIR region have a spectral range from 900-1790 nm and a spectral resolution of 13 nm. This is a rather broad spectral resolution compared with existing NIR systems which operate in the 900-2500 nm range with a resolution around 1 nm. The relative insensitivity of available multispectral cameras in the NIR region combined with the broad spectral resolution of current Imspector technology has limited successful multispectral imaging applications for this part of the electromagnetic spectrum. It is expected that future imaging applications in the NIR region with corresponding algorithms will be presented in literature when new camera technology becomes available on the market for these regions of the electromagnetic spectrum. Another decelerating effect for the development of applications in the NIR regions might be the water absorbtion bands. The majority of fruit and agricultural products contain a huge amount of water which results in spectra where the water absorbtion bands overrule the absorbtion band of other neighboring compounds (E.g. 70% of a potato consists of water) and thus a accurate measurement of those compounds can be difficult.

Improvement of camera hardware and optics will translate current laboratory research into realtime applications for the online sorting and grading of food and vegetables. Currently, there is a huge gap between the common aperture camera capable of acquiring a 3 band multispectral image simultaneously and the imaging spectrograph (Imspector) technology. Once this gap has been reduced by the introduction of new hardware, laboratory applications suitable for realtime inspection which require more than 3 image bands become candidate for conversion to realtime applications. At the same time, associated algorithms and techniques might need adaptation to be suitable for realtime performance.

7.3.2 Chemometrics

When spectral imaging hardware as described above improves in the future and applications like spatial NIR spectroscopy (NIR imaging) become possible, topics from both the image processing domain and the spectroscopy domain need to be combined for successful utilization. With respect to the development of new chemometric techniques and algorithms for image exploration or classification in the field of post-harvest product inspection, new territories can be explored where besides spatial and spectral information also particular low-level domain knowledge is utilized. For example, in the case of French fries inspection, using particular information about cultivar specific properties (e.g. disease sensitivity) might improve yield, purity and classification accuracy. In this thesis a new unsupervised classifier is described which utilizes both spatial and spectral information during segmentation. A similar modification for supervised classifiers is an obvious topic for future research. As mentioned in Chapter 1, various manuscripts about the combined use of spatial and spectral information for image segmentation have been reported in literature before. However, information about the best performing technique on specific applications is not known and this an interesting future research topic. A more challenging research topic for combined use of spatial and spectral information is the development of a technique which is less application dependent and can be applied more generally. Also, with the ongoing expansion of the number of bands in multispectral images, applications like FEMOS as described in Chapter 5 are required for effective image exploration and data set extraction. As for the FEMOS procedure, automatic parameter adjustment or spatial filter selection are topics that need further development.

7.3.3 External factors

Besides this, future applications and research topics will not only be determined by technological standards, but also by new trends, demands and standards in human society, as recently summarized in literature [2]:
”(Fruit) quality should not be considered as an absolute unchanging variable. Rather, it is a concept that changes dynamically across time as consumers’ expectations change. As new products are released and new postharvest technologies developed, there will be a corresponding impact on the lifecycle of existing products”

Bibliography

[1] A. Schut, *Imaging Spectroscopy for Characterization Grass Swards*. PhD thesis, Wageningen University, 2003.

[2] F. Harker, F. Gunson, and S. Jeaher, “The case for fruit quality: an interpretive review of consumer attitudes and preferences for apples,” *Postharvest Biology And Technology*, vol. 28, pp. 333–347, 2003.

Summary

This thesis describes different novel chemometric techniques applied to multispectral images for quality inspection on agricultural food products. These images do not only have a huge number of spectral bands which makes training set selection a challenging task, they also contain classes with small defects or abnormalities where objects of these classes are easily missed. For the segmentation and classification of multispectral images the unsupervised Fuzzy C-Means (FCM) clustering algorithm is often used for its transparency and good performance in high dimensional spaces. With the availability of high spectral resolution multispectral camera's new application areas have become available in which both spatial information and spectral information can be used. A drawback of many unsupervised techniques, including FCM, is that the spatial information is not used during the classification of such multispectral images. Therefore in Chapter 2, a modification of FCM is presented which combines both spatially and spectrally information into the clustering process to improve image segmentation. The presented geometrically guided conditional FCM (ggc-FCM) requires a threshold to determine whether object pixels are outliers. The use of a threshold limits it use in sorting and inspection applications and therefore in Chapter 3 a generalization of this technique is presented. The spatially guided FCM (sg-FCM) not only uses the spatially neighborhood information, even a priori spatial shape information can be used during clustering to guide the image segmentation. The algorithm is compared with standard FCM and the combination of standard FCM followed by a majority filter. Both techniques are applied on synthetic and real multispectral images and have shown improved performance compared to traditional FCM and the majority filter.

Although FCM is often used for the unsupervised segmentation of multispectral im-

ages it has several known drawbacks which can effect the clustering outcome when applied to multispectral images which contain defects or diseases. Usually, the defect or disease area is small compared to the overall area of the product under inspection. Unfortunately, FCM is known to be sensitive for this which results in underestimated defect classes as smaller defect classes are drawn to the larger clusters. A modification of FCM is presented in Chapter 4 which overcomes this sensitivity. The presented cluster insensitive FCM (csi-FCM) is compared with two cluster techniques which are known to be unsensitive for unequal number of points in the clusters. The csi-FCM algorithm performs similar or even outperforms the other techniques for the used data sets and real multispectral images.

Unsupervised segmentation of multispectral images is possible as long as the images have limited spatial resolution or limited number of spectral of bands. When the number of spectral bands increases, the huge amount of data in the multispectral images requires computational demands which are not feasible in most applications. A widely used approach is to apply an unsupervised classifier to a small sample of the image data for the estimation of the classes and then classify the entire multivariate image using a supervised classifier trained with the estimated model. However, it has been shown that this strategy leads to under or overestimated classes in the segmented image, especially for multispectral images of food products with small defects or abnormalities where objects of these classes are easily missed.

Therefore, in Chapter 5, a Feedback Multivariate Model Selection (FEMOS) is presented which automated the segmentation proces by combining supervised and unsupervised techniques. The segmentation procedure is an iterative procedure and continues until the current model used by the unsupervised classifiers equals the model as used by the supervised classifier. The difference evaluation between both models is determined by a feedback principle which is based on the human visual comparison. The only parameter is a threshold for the stop criterion which determines the amount of detail of the model and thus the amount of detail in the segmented image. Experiments show that the FEMOS procedure is capable in correctly segmenting different type of multivariate images, even if the number of spectral bands is high.

In Chapter 6, an application is presented where both multispectral images and RGB color images of French fries with different defects and diseases are evaluated. The explorative analysis of the multispectral images prior to classification shows that defects are visible in the multispectral images while invisible in the RGB color images and thus for the human eye. Both multispectral images and RGB color images are classified with different classifiers. The effect of applying different spectral preprocessing techniques on the classification results is also investigated. The results show that the multispectral classification results outperform the RGB color images not only in terms of accuracy but also in terms of yield and purity. The best classification results for French fries multispectral images are obtained with a support vector classifier and a modified version of standard variate normal preprocessing. The best classifier for French fries RGB color images is (k=3)-Nearest Neighbor without any spectral preprocessing. Finally, Chapter 7 describes the conclusions and some future aspects of multivariate imaging for agricultural product inspection.

Samenvatting

Dit proefschrift beschrijft verschillende nieuwe chemometrische technieken welke zijn toegepast op multispectrale beelden voor kwaliteitsinspectie van agroproducten. Deze beelden hebben niet alleen een enorm aantal spectrale banden, wat de selectie van een goede training set bemoeilijkt, maar bevatten ook zeer kleine defect klassen die makkelijk over het hoofd gezien worden. Voor het segmenteren en classificeren van deze multispectrale beelden wordt vaak gebruik gemaakt unsupervised technieken, waarvan Fuzzy C-Means (FCM) clustering één van de meest gebruikte technieken is vanwege o.a. de goede performance in hoog dimensionale ruimten. Met het op de markt komen van hoge resolutie multispectrale camera's worden nieuwe toepassingen mogelijk waarbij zowel de ruimtelijke als de spectrale informatie gebruikt kan worden. Een nadeel van vele unsupervised technieken, inclusief FCM, is dat er voor de uiteindelijke segmentatie van de multispectrale beelden geen gebruik wordt gemaakt van de ruimtelijke informatie.

In hoofdstuk 2 is een aangepaste FCM techniek beschreven die zowel de spectrale informatie als de ruimtelijke informatie gebruikt om tot een verbeterde segmentatie te komen. De techniek, genaamd geometrically guided conditional FCM (ggc-FCM) gebruikt een drempelwaarde om te bepalen welke objecten als outlier kunnen worden bestempeld. Het gebruik van een dergelijke drempelwaarde beperkt echter het gebruik van deze techniek in realtime sorteer- en inspectieapplicaties en daarom is in hoofdstuk 3 een meer generieke aanpak van deze methode beschreven. De ruimtelijk gestuurde FCM (sg-FCM) gebruikt niet alleen ruimtelijke informatie om de segmentatie te sturen, ook a priori vorminformatie kan worden gebruikt. De prestaties van de techniek zijn vergeleken met standaard FCM en standaard FCM in combinatie met een majority filter. Zowel kunstmatige beelden als multispectrale beelden van agro-

producten zijn gebruikt in de experimenten waaruit blijkt dat sg-FCM beter presteert.
Hoewel FCM vaak wordt gebruikt als unsupervised techniek voor het segmenteren van multispectrale beelden heeft de techniek toch een aantal tekortkomingen die de segmentatie nadelig beïnvloeden, zeker als de techniek gebruikt wordt voor het segmenteren van beelden die ziekten en gebreken bevatten. In het algemeen is het oppervlak van het te detecteren defect of ziekte klein ten opzichte van het totale te inspecteren oppervlak. Helaas is FCM gevoelig voor dit soort situaties waar het aantal objecten in de te segmenteren klassen veel ten opzichte van elkaar verschillen. Het effect van deze klassegroottegevoeligheid is dat het oppervlak van de kleine gebreken wordt onderschat doordat de kleine klassen worden aangetrokken door de grote klassen. Dit probleem is opgelost in hoofdstuk 4 waar een aangepaste FCM techniek is beschreven. De nieuwe techniek, cluster size insensitive FCM (csi-FCM) genaamd, wordt naast de traditionele FCM ook vergeleken met twee clustertechnieken die ook ongevoelig zijn voor het kleine klassen probleem. De resultaten laten zien dat csi-FCM minimaal gelijke maar vaker betere prestaties levert dan de twee bekende technieken.

De unsupervised segmentatie van multispectrale beelden is mogelijk zolang de beelden een beperkte ruimtelijke resolutie hebben of een beperkt aantal spectrale banden. Als de ruimtelijke of spectrale resolutie toeneemt neemt het geheugengebruik dermate toe dat dit niet meer werkbaar is in het merendeel van de applicaties. Een veel gebruikte techniek om het geheugenprobleem te omzeilen is om een unsupervised classifier toe te passen op slechts een subset van de gehele dataset. Daarna wordt het gehele beeld geclassificeerd met een supervised classifier die getraind is met het model van de unsupervised classifier. Er is is echter aangetoond dat deze strategie leidt tot een over- of onderschatting van het aantal klassen in het gesegmenteerde beeld, hetgeen een probleem is voor multispectrale beelden met kleine defect klassen die hierdoor eenvoudig gemist kunnen worden. Daarom is in hoofdstuk 5 een nieuwe techniek, genaamd Feedback Multivariate Model Selection (FEMOS), gepresenteerd die het segmentatie probleem automatiseert, waarbij een combinatie van unsupervised en supervised technieken is gebruikt. De techniek bestaat uit een iteratieve procedure waarin een initieel model wordt aangepast aan de hand van het verschil tussen het originele beeld en het gesegmenteerde beeld, min of meer op de manier zoals wij als mensen ook beelden vergelijken. Uit de experimenten blijkt dat de FEMOS procedure uitstekend in staat is om verschillende multivariate beelden te segmenteren, ook van beelden met zeer veel spectrale banden.

In hoofdstuk 6 wordt een toepassing beschreven waarin zowel multispectrale beelden als kleurenbeelden worden gevalueerd voor het detecteren van ziekten en gebreken op ongebakken franse friet. De exploratieve analyse voorafgaand aan de classificatie laat zien dat bepaalde defecten zichtbaar zijn in multispectrale beelden terwijl deze gebreken niet of nauwelijks zichtbaar zijn in de kleurenbeelden en dus ook niet voor het

menselijk oog. Zowel de multispectrale beelden als de kleurenbeelden zijn geclassificeerd met verschillende typen classificatoren. Hierbij zijn verschillende soorten spectrale voorbewerking gebruikt om het effect op classificatie te achterhalen. De experimenten laten zien dat met multispectrale beelden betere classificatie resultaten te behalen valt dan met RGB beelden.
Tenslotte worden in hoofdstuk 7 de conclusies en enkele toekomstige aspecten over multispectrale beeldverwerking voor agrarische productinspectie beschreven.

Curriculum Vitae

Jacco Noordam werd geboren op 23 april 1970 te Bleiswijk. In 1986 behaalde hij het MAVO diploma aan de Winschoter Scholen Gemeenschap te Winschoten. Van 1986 tot 1989 bezocht hij de Middelbare Technische School te Stadskanaal alwaar hij het diploma elektronica behaalde. Na een actieve studententijd in de mooiste studentenstad van het land behaalde hij in 1993 het diploma elektrotechniek aan de Rijkshogeschool Groningen. De universitaire opleiding elektrotechniek werd in 1996 afgerond aan de Universiteit Twente. De afstudeeropdracht werd uitgevoerd op de vakgroep Meettechniek en Instrumentatie onder leiding van professor Paul Regtien. In 1996 trad hij in dienst van het huidige Agrotechnoloy and Food Innovations B.V. op de toenmalige afdeling Computerbeeldanalyse. In oktober 1999 is het promotieonderzoek van start gegaan.